

THE KPNO/DEEPRANGE DISTANT CLUSTER SURVEY: I. THE CATALOG & THE SPACE DENSITY OF INTERMEDIATE REDSHIFT CLUSTERS

MARC POSTMAN¹

Space Telescope Science Institute², Baltimore, MD 21218

TOD R. LAUER

National Optical Astronomy Observatories³, Tucson, AZ 85726

WILLIAM OEGERLE¹

Laboratory for Astronomy and Solar Physics, Code 681, NASA/GSFC, Greenbelt, MD 20771

MEGAN DONAHUE¹

Space Telescope Science Institute², Baltimore, MD 21218

Accepted for publication in The Astrophysical Journal

ABSTRACT

We have conducted an automated search for galaxy clusters within a contiguous 16 square degree *I*-band survey in the north Galactic hemisphere. A matched filter detection algorithm identifies 444 cluster candidates in the range $0.2 \lesssim z \lesssim 1.2$. The full catalog is presented along with the results from a follow-up spectroscopic survey. The estimated redshift distribution of the cluster candidates is consistent with a constant comoving density over the range $0.2 \leq z_{est} \leq 0.8$. A decline in the cluster space density by more than a factor of 3 over this redshift range is rejected at $> 99.9\%$ confidence level. We find that the space density of $\Lambda_{CL} \geq 40$ clusters in our survey lies in the range $(1.6 - 1.8) \times 10^{-5} h_{75}^3 \text{ Mpc}^{-3}$, ~ 1.5 times higher than the local distribution of comparably rich Abell RC ≥ 0 clusters. The Λ_{CL} distribution is consistent with a power-law. The discrepancy between the space density of Abell clusters and the clusters in this survey declines quickly as Λ_{CL} increases, suggesting that the difference at lower richness is due to significant incompleteness in the Abell catalog. A percolation analysis reveals that 10 - 20% of the spectroscopically confirmed distant clusters are linked into superclusters at overdensities between $10 < \delta\rho/\rho < 50$, similar to what is seen in the local cluster distribution. This suggests that there has been little evolution of the cluster-cluster correlation length for $z \lesssim 0.5$.

Subject headings: large-scale structure, clusters of galaxies, cluster catalogs, superclusters

1. INTRODUCTION

The evolution of clustering is an inevitable consequence of any gravitationally driven model of structure formation. The scale dependence and amplitude of this evolution place significant constraints on the nature of dark matter and key cosmological parameters. Clusters of galaxies provide an efficient way to trace matter on large-scales and significant work has been done to both measure the current epoch cluster-cluster correlation length (*e.g.*, Bahcall & Soneira 1983; Postman et al. 1992; Nichol et al. 1992; Croft et al. 1997; Borgani et al. 1999; Collins et al. 2000) and to determine the constraints these measurements place on structure formation models (*e.g.*, Eke et al. 1996; Mo et al. 1996; Colberg et al. 2000; Moscardini et al. 2001). In light of the extensive observational constraints available on the clustering properties of clusters at $z < 0.1$, it is highly desirable to obtain similar measurements at higher redshifts ($z \lesssim 1$) to constrain the evolution of clustering on large-scales and at high masses. Indeed, the evolution of clustering of the high-mass end of the matter distribution is typically the most sensitive to variations in cosmological parameters (Peebles, Daly, & Juszkievicz 1989). To

achieve accurate constraints on the evolution of clustering on large-scales requires galaxy and cluster surveys that are both deep and wide. The depth must be sufficient to sample sources significantly fainter than the characteristic luminosity at redshifts where significant evolution can be detected. The area must be large enough to reliably sample structures on scales much greater than the expected correlation lengths.

The advent of large format CCD detectors, CCD mosaic cameras, and multi-object spectrographs has made mapping the large-scale distribution of clusters and galaxies at intermediate redshifts quite feasible. We completed the first moderately deep imaging survey that also subtended a substantial contiguous area ($\sim 16 \text{ deg}^2$) to establish a database capable of accurately measuring the clustering of galaxies and clusters up to scales of $\sim 130 h_{75}^{-1} \text{ Mpc}$ over the redshift range $0.2 \lesssim z \lesssim 1$, using the first of the large format detectors at the Kitt Peak National Observatory (Postman et al. 1998; Szapudi et al. 2001). There are now at least 5 additional optical/NIR surveys with total areas in excess of 10 square degrees that have depths sufficient to detect a substantial number of clusters up to redshifts

¹ Visiting Astronomer Kitt Peak National Observatory, NOAO.

² The Space Telescope Science Institute is operated by the Association of Universities for Research in Astronomy (AURA), Inc., under National Aeronautics and Space Administration (NASA) Contract NAS 5-26555.

³ The National Optical Astronomy Observatories are operated by AURA, Inc., under cooperative agreement with the National Science Foundation.

near unity: the ESO Imaging Survey ($\sim 15 \text{ deg}^2$; Olsen et al. 1999), the NOAO Deep Wide-Field Survey ($\sim 18 \text{ deg}^2$; Jannuzi et al. 2000), the BTC Survey ($\sim 40 \text{ deg}^2$; Monier et al. 2001), the Red Sequence Cluster Survey ($\sim 100 \text{ deg}^2$; Gladders & Yee 2000), and the Las Campanas Distant Cluster Survey ($\sim 130 \text{ deg}^2$; Gonzalez et al. 2001). X-ray cluster surveys (*e.g.*, Henry et al. 1992; Scharf et al. 1997; Rosati et al. 1998; Ebeling et al. 2000; Romer et al. 2000) have also discovered a moderate number of intermediate redshift ($0.5 < z < 1$) cluster over areas in excess of 100 square degrees. Combined with the application of a variety of objective cluster detection algorithms, which enable the inevitable selection biases to be properly quantified, these surveys are now yielding important and accurate constraints on cosmological parameters (*e.g.*, σ_8, Ω_m) as well as on the abundance, clustering, and properties of galaxy clusters over the last half of the current age of the universe.

In this paper, we present the results of our automated cluster search using the Deeprange survey along with measurements of the space density of clusters as a function of redshift and richness. The scientific requirements that were used to design the survey and a summary of the imaging observations and data reduction are presented in §2. The construction and calibration of the galaxy catalog used as the input for the cluster detection algorithm are described in §3. The algorithm and resulting cluster catalog are presented in §4 along with a detailed description of the derivation of the selection function, richness calibration, and false positive rate estimates. We have also performed a follow-up spectroscopic survey of the cluster candidates, which is described along with the spectroscopic data reduction methods in §5. The main results of this paper are presented in §6 and are followed by a summary of our key conclusions in §7. Throughout this paper we define $h_{75} = H_0 / (75 \text{ km s}^{-1} \text{ Mpc}^{-1})$ and adopt $\Omega_m = 0.2$, $\Omega_\Lambda = 0$.

2. SURVEY DESIGN

Our survey field is a contiguous $4^\circ \times 4^\circ$ area located at high Galactic latitude. This geometry is motivated by a number of important considerations. First, to explore large-scale clustering of clusters at $z \sim 1$, the survey must subtend a contiguous comoving scale that is larger than $50h_{75}^{-1} \text{ Mpc}$ – the locally observed zero-crossing scale in the cluster-cluster two-point correlation function (Klypin et al. 1994). Indeed, the linear comoving scale of the survey must at least be comparable with $130h_{75}^{-1} \text{ Mpc}$ – the size of the largest structures in the local galaxy distribution (*e.g.*, Vogeley et al. 1992; Lin et al. 1996; Colless et al. 2001; Zehavi et al. 2002). At $z = 1$, $130h_{75}^{-1} \text{ Mpc}$ (comoving) corresponds to an angular scale of $\sim 2.7^\circ$. Second, to measure low-order clustering statistics at intermediate redshifts with accuracies comparable to those at low redshift our survey needs to subtend a volume that is comparable with the typical low redshift cluster survey. A $|b| \geq 30^\circ$ cluster survey to $z = 0.07$ (*e.g.*, Bahcall & Soneira 1983) subtends approximately $4 \times 10^7 h_{75}^{-3} \text{ Mpc}^3$ – to cover a similar volume out to $z = 1$ would require a solid angle of approximately 20 deg^2 . We also need to have approximately 300 to 500 clusters in the survey area ($\sim 25\%$ of which would lie within $0.75 \leq z \leq 1.15$) to assure mod-

erately accurate measurements of the clustering at higher redshifts. When we began to plan this survey, estimates of the surface density of clusters from small area surveys (Gunn et al. 1986; Postman et al. 1996) were in the range 15-20 clusters deg^{-2} out to $z = 1$, and thus a survey area of at least 16 deg^2 was required. Lastly, although one can construct a survey that samples these scales by combining data from many non-contiguous fields, finite sampling and cosmic variance effects can severely degrade the accuracy of clustering statistics derived from such a patchwork survey (*cf.* Postman et al. 1998).

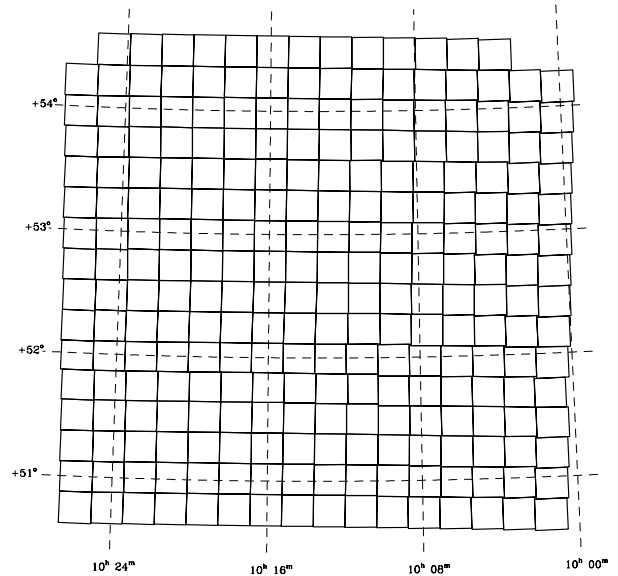


FIG. 1.— The positions of the 253 survey pointings on the sky. Grid 001 is located at the southeastern corner. The survey originally was designed with 256 pointings but 1 pointing was excluded due to the presence of a $V = 7$ mag star (HD 90249) and 2 others were never observed due to weather limitations. Each 16 arcminute grid overlaps its adjacent grids by 1 arcminute enabling accurate photometric and astrometric calibration across the entire survey.

The survey is centered at 10h 13m 27.95s +52d 36m 43.5s (J2000) by virtue of its high Galactic latitude ($+51^\circ$), low HI column density ($2.2 \times 10^{20} \text{ cm}^{-2}$), high declination (enabling extended visibility from KPNO), low IRAS 100μ cirrus emission, and the absence of many bright stars or nearby rich clusters. The E(B-V) estimates from Schlegel, Finkbeiner, & Davis (1998) (computed using the NED extinction calculator) for our survey region yield a mean value of 0.011 mag, a maximum value of 0.018 mag, and a minimum value of 0.005 mag. The mean E(B-V) value of 0.011 mag corresponds to an I -band extinction of 0.02 mag (assuming an $R_V = 3.1$ extinction curve).

2.1. Observations

The imaging phase of the survey was conducted in the I -band using the prime focus CCD camera on the KPNO Mayall 4m telescope. Working in the I -band assures good completeness in the detection of clusters out to $z \sim 0.8$ (see §4.2). The camera has a $16'$ field of view (0.47 arcseconds pixel^{-1} for the T2KB CCD); 256 exposures were,

therefore, required to survey the entire field. Each pointing overlapped its adjacent pointing by 1 arcminute – the overlap is required to guarantee accurate photometric and astrometric calibration of the galaxy catalog (see §3.2 and §3.3). Figure 1 shows the configuration of the survey pointings on the sky.

The observations were conducted over a 2 year period between Jan. 1994 and March 1996. Each exposure was 900 seconds in duration⁴. This allows us to reach a 5σ detection limit (for point sources) of $I=23.85$, sufficient to detect cluster galaxies 2 magnitudes fainter than the typical first-ranked elliptical at $z = 1$ (*e.g.*, Aragon-Salamanca, Baugh, & Kauffman 1998; Postman, Oke, & Lubin 2001). Going to this depth was essential – a shallower survey would only be sufficient for detecting the very richest $z \sim 1$ clusters and would limit our conclusions about evolution of structure. (At $I = 23.5$, we are able to detect $z \sim 1$ Abell richness class 1 systems). Since we also wish to conduct follow-up spectroscopic surveys based on these images, it was desirable to have the data reach the spectroscopic limit of 8 - 10m class telescopes with a reasonable signal-to-noise ratio. The median seeing achieved in the images is 1.3 arcseconds FWHM (85% of the images have seeing of 1.5'' or better) and the median airmass is 1.2. Although the survey was designed with 256 pointings, only 253 images were ultimately acquired – 1 pointing was excluded due to the presence of a $V = 7$ mag star (HD 90249) and 2 others were never observed due to weather limitations.

Fringing was minimized by using the prime focus camera scan table. The scan table suppresses flat-field and fringing artifacts by physically moving the detector in sync with and parallel to an electronic shift of charge. After some experimentation, it was determined that a 60-pixel scan was the optimal choice (the fringe amplitude decays more slowly with scan size when the scan size exceeds 60 pixels but decays quite rapidly with scan size for scans less than 60 pixels). With this set up, we were able to flatten the images to 1 percent or better. The scan process reduces the usable field of view in the scan direction by 28 arcseconds. The reduced images from this survey are publicly available from the NOAO science archive (<http://archive.noao.edu/nsa/>).

2.2. Imaging Data Reduction

To prepare the image data for use in galaxy and cluster detection, all significant instrumental signatures are removed using well-tested data reduction procedures. Flat-fielding and de-fringing of the image data represent the most significant steps in this process. We begin the reduction process with basic de-biasing and removal of pixel-to-pixel sensitivity variations using an averaged dome flat image. We then create a master median sky image using all the images from a given observing run. An illumination correction image (intended to remove large-scale sensitivity variations) is derived from this median image by fitting a two-dimensional, second-order surface and then normalizing the mean pixel value in the fit to unity. A fringe correction image is derived by dividing the master median by

the illumination correction image. The illumination and fringe correction processes are then performed in the usual manner. The resultant images exhibit extremely uniform sky levels: typical sky variations are less than 0.2% on scales between 50'' and 240''. Furthermore, small (1 pixel) to medium (30 pixels) scale sky variations are consistent with photon statistics indicating that the fringe removal has worked extremely well.

3. THE GALAXY CATALOG

We use a modified version of the Faint Object Classification and Analysis System (FOCAS; Jarvis & Tyson 1981; Valdes 1982) to detect and classify objects in the images. The modifications include an algorithm that allows the use of a variable PSF in an image for object classification and an algorithm that cleans spurious detections surrounding bright stars and galaxies. We use a $3 - \sigma$ detection threshold⁵ and a 12 pixel (2.65 arcsec²) minimum object area constraint. These parameters work well for 95% complete detection of galaxies with isophotal magnitudes that are 0.5 mag brighter than the detection threshold (*e.g.*, a 95% completeness limit of $I = 23.5$ when $\mu_{I,det} = 24$).

We run FOCAS on each individual $16' \times 16'$ image and construct a corresponding instrumental object catalog. These individual catalogs are then merged to construct our master galaxy catalog once the photometric and astrometric calibration of the entire survey is completed. We manually defined ~ 4000 rectangular regions in the vicinity of bright stars or galaxies ($I \lesssim 14$) where object detection is compromised due to excessive pixel saturation, high intensity PSF wings, and/or significant scattered light. Any detections that lie within these regions are excluded from the analyses. The total survey area is 14.7 deg² after accounting for all the exclusion regions.

3.1. Star – Galaxy Classification

The FOCAS object classifier attempts a 2D fit of a linear combination of a stellar PSF and a broadened PSF⁶ for each detected object. The classification of an object depends on what fraction of the fit is represented by the broadened PSF. Typically, if a PSF broadened by more than a factor of 1.3 comprises at least 25% of the amplitude of final fit the object is classified as a galaxy. The stellar PSF is derived by selecting ~ 25 star-like sources in each image.

The images in this survey were obtained prior to the installation of the enhanced prime focus corrector (installed in late 1996). Hence, there are noticeable PSF variations from the image center to the edge. The standard FOCAS resolution classifier uses a position invariant PSF. We modified this software to allow a position dependent PSF model to be employed. This modification was critical in obtaining uniform object classification across the field of view. We derive an empirical position dependent PSF model based on measurements of the FWHM as a function of distance from the optical center. We find that the expression

$$B(r) = a_0 + a_2 r^2 + a_4 r^4 \quad (1)$$

⁴ CR splits were not performed because the cosmic ray hit rate is low – no significant increase in spurious detections or contamination of object photometry was found. The overheads associated with CR splits are substantial.

⁵ In calibrated units, the detection threshold is typically $\mu_{I,det} = 24.2$ mag arcsec⁻² but, of course, this depends on the mean sky level.

⁶ The broadened PSF is simply a wider version of the stellar PSF. See equation 10 in Postman et al. (1996) for details.

is an excellent representation. In this equation, $B(r)$ is the FOCAS broadening factor and r is the radial distance from the optical center. We fit equation 1 to the lower envelope of the FOCAS broadening factor as a function of r . The maximum broadening factor allowed for an object classified as a star is then taken to be $\min[B(r) + 0.3, 2]$. The upper limit of 2 is set by an assessment of the maximum broadening induced

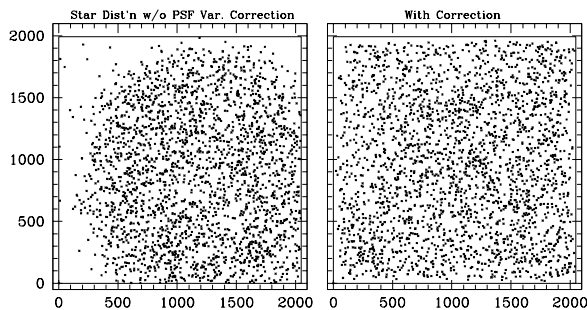


FIG. 2.— The distribution of objects classified as stars before (left) and after (right) the application of the position-dependent PSF classifier. The data are based on a stacking of objects in 69 of the 253 images. The plot shows a random sampling of 5000 of the $\sim 60,000$ stellar objects with $19 \leq I < 23$. The optical center of the imager is located near x,y position (1200,920).

by the PSF distortion near the detector edges. The 0.3 offset is the default used in FOCAS (*e.g.*, in an image with a constant PSF, the default FOCAS classification rule defines stars as objects with $B = 1.0 \pm 0.3$). The location of best focus is not always at $r = 0$ and it can vary from run to run. Therefore, the coefficients are derived independently for each image and the a_2 coefficient can be positive or negative (the a_0 and a_4 coefficients are always positive). In fact, the a_2 coefficient is negative for 98% of the images because the region of good focus is fairly wide and significant PSF degradation occurs only near the edges of the CCD field of view. The optical center is derived by plotting the positions of all objects classified as stars *prior* to the use of the position dependent PSF. There is a well defined circular boundary beyond which the stellar density falls off significantly (and the galaxy surface density increases correspondingly). The center of this region is the optical center and is located at pixel position (1200, 920) in our data. Figure 2 shows a random sampling of the distribution on the CCD of $\sim 60,000$ objects classified as stars (with $19 \leq I < 23$) before and after application of the position dependent PSF classifier. Only minor inhomogeneities in the stellar distribution remain after accounting for the PSF variations. There is also no

signature of the CCD image size in the galaxy two-point correlation function (Postman et al. 1998) providing further validation that the above procedure for correcting the PSF variations is successful.

The FOCAS classifier works well down to about $I = 21.5$ in these data (based on running the same code on simulations). Fainter than this, a statistical approach is needed to assess the probability that an object is a galaxy. Specifically, we find that for $I > 21.5$ there is a systematic tendency for the classifier to identify galaxies as stars. We have quantified this effect by extrapolating the bright star counts ($I \leq 20$) to fainter limits and then compute the number of stars that should be in each mag bin. From this we generate the probability (as a function of magnitude) that a given faint star is really a galaxy. That function is:

$$P(s \rightarrow g) = 0.663 - 5.33 \times 10^{-3} I^2 + 1.00 \times 10^{-5} I^4 \quad (2)$$

where I is the isophotal mag and $P(s \rightarrow g)$ is the probability that a star of magnitude I is really a galaxy. We clamp this function to lie in the range $[0,1]$ as it is a polynomial best fit and does not give valid results outside the range of the fit ($18.25 \leq I \leq 24.5$). The classifier rarely misclassifies a faint star as a galaxy, however. We note that for $I > 21.5$ galaxies outnumber stars by at least a factor of 5 (the galaxy/star ratio is ~ 10 by $I = 23.5$, based on the statistically corrected star and galaxy counts). Hence, star contamination would not exceed $\sim 10 - 15\%$ even if one simply classified every object fainter than $I = 21.5$ as a galaxy. We, however, do use the above probability function to assemble an object catalog with statistically reliable galaxy counts down to $I = 24$. Our galaxy counts as a function of I magnitude are published in Postman et al. (1998). In particular, we refer the reader to figure 2 of that paper, which shows a comparison of our galaxy counts to those from other surveys. The good agreement between our counts and those from other surveys demonstrates the accuracy of our statistical corrections to our faint object classifications.

3.2. Photometric Calibration of the Survey

Accurate reduction of the survey images to a common photometric zeropoint is essential to ensure both uniform detection of galaxy clusters over the area of the survey, as well as for characterizing the galaxy-galaxy correlation function on large angular scales. The basic calibration strategy is to use the overlap of any survey image with its north/south and east/west neighbors in the 16×16 grid of individual CCD fields to enforce local consistency of the photometric scale. This method is actually essential, as the entire survey was observed in a mix of non-photometric/photometric sky conditions, thus some fields can only be calibrated by reference to their neighbors. Global uniformity over the survey is provided by sequences of fields observed in photometric conditions, as well as a set of independent calibration observations, kindly provided by R. Y. Shuping, using a large-field CCD camera at the KPNO 0.9m telescope. The zeropoint, itself, is established by Landolt (1983) standards observed at both the KPNO 4m and 0.9m telescopes.

Measuring the photometric scale of any image with respect to its neighbors begins with identifying common objects in the catalogues of the overlap regions. This is done

for each pair of images that have significant angular overlap. The second step is to estimate the photometric offset between the two images based on the photometric offsets between all objects in common, under an assumed initial estimate of the photometric zeropoint. In practice, to treat both images equally, the offset is measured as the constant that best minimizes the differences of the *ad hoc* magnitudes for each object, weighted by its average luminosity within the two images. One can visualize this graphically as trying to fit a flat-line to a simple plot of magnitude versus magnitude for the common objects rotated 45° , to avoid treating magnitudes in the two images as a pair of independent and dependent variables. The statistical accuracy of the photometric offset for any image pair is determined by the density of objects in the overlap region, and their distribution in luminosity; its median value over all pairs in the survey is 0.019 mag.

The set of photometric differences between all neighboring images in the survey grid defines a set of equations that can be solved to estimate the photometric correction for any individual image to make it consistent with the survey overall; Koranyi et al. (1998) present an independent development of this approach. There are 253 usable images in the survey, thus we require 253 photometric corrections, Δ_i . The photometric offsets, m_{ij} , between adjacent images are defined in the sense that the magnitudes of objects in grid j are subtracted from grid i . If we solve for Δ_i by a standard least-squares procedure, then we must minimize the overall error:

$$E = \sum_{i=1}^{253} \sum_{j=1}^{253} \epsilon_{ij} (\Delta_i - m_{ij} - \Delta_j)^2, \quad (3)$$

where $\epsilon_{ij} = 1$ when grids i and j are adjacent, and is zero otherwise. If we minimize E with respect to Δ_i , then we get:

$$\frac{\partial E}{\partial \Delta_i} = 0 = \Delta_i \sum_{j=1}^{253} \epsilon_{ij} - \sum_{j=1}^{253} \epsilon_{ij} m_{ij} - \sum_{j=1}^{253} \epsilon_{ij} \Delta_j. \quad (4)$$

This generates a system of linear equations that can be solved for Δ_i . The problem is over-determined as each survey row has a maximum of 15 photometric differences for $16 \times 15 = 240$ east-west comparisons and likewise 15 sets of 16 north-south inter-row comparisons, for a maximum total of 480 m_{ij} (in fact, because there were only 253 frames available, there are only 474 comparisons). Monte Carlo simulations show that the error in the photometric offsets are 0.017 mag, slightly smaller than the error in the individual pair-wise differences.

One serious problem is that the photometric differences between image pairs do not constrain the overall average zeropoint of the survey. The solution is simply to require one of the images to have a reference zeropoint based on standard-star calibrations, the final offset corrections are then defined to this zeropoint. A more serious problem is that calibration based on differences leads to the best local agreement between any image and its neighbors in the survey, but is prone to substantial drift of the zeropoint over large angular scales. If the individual images have a slight zeropoint drift over their extent, as might result from small errors in the flat-field illumination pattern, then this error may actually be compounded by this calibration process. For example, if there were a 2% north to south gradient

in the photometric scale of any image, then the total drift across the declination extent of the survey would exceed 30% (if all images had the same error). The solution is to use external calibration frames plus those survey images taken in photometric conditions with good standard star solutions to guard against any photometric drift. In practice, the initial zeropoint determined from differences alone appeared to drift by 0.22 mag in declination and 0.08 in RA over the extent of the survey, which was readily corrected with simple linear terms. The larger drift in declination probably reflects the fact that the survey was extended in declination over a number of runs, while we were able to scan a few complete east-west rows in a single night. We note that on photometric nights the pattern of measured photometric differences clearly reflected the airmass variation as the survey field transited the sky.

3.3. Astrometric Calibration

We calibrate the astrometry using objects detected in the Digitized Palomar Observatory Sky Survey (DSS). For each CCD frame, we typically cross identify 32 DSS objects (minimum used was 10, maximum used was 60). The objects matched are chosen to exclude saturated stars ($I \lesssim 17$) and objects fainter than $I \sim 19$. A six-term, second order astrometric solution is then derived using the CCD x-y positions and the DSS celestial coordinates. The mean rms of the fits is $0.56''$ and is dominated by the uncertainty of the centroids of faint objects in the DSS images.

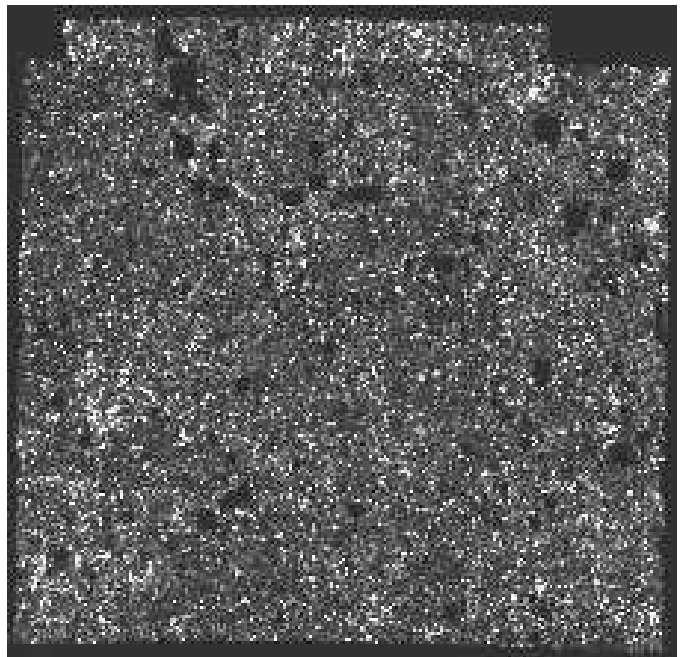


FIG. 3.— The angular distribution of the $\sim 710,000$ galaxies in our survey with $I \leq 23.5$. Each galaxy is represented as a point with intensity proportional to $\text{dex}(-0.4m)$ where m is the isophotal I -band magnitude. Blank rectangular areas are the regions excluded due to the presence of bright stars.

Systematic errors associated with the DSS astrometric calibration itself can be as large as $2''$ but relative astrometry at the $0.3''$ level can be achieved, as evidenced by the success of our spectroscopic follow-up (see §5). We also derive

the T2KB CCD pixel scale as part of the astrometric calibration process and find a mean value of 0.4702 ± 0.0005 arcsec pixel⁻¹, in excellent agreement with the KPNO published value.

As a final check on our astrometric calibration, we cross-correlate our catalog with the FIRST VLA survey catalog (Becker, White, & Helfand 1995). We look for any image-wide astrometric offsets as well as any systematic offsets that may be a function of CCD position. We detect image-wide systematic offsets between our initial DSS astrometry and that from the FIRST catalog that are typically $0.5 - 1''$ in amplitude. These are corrected in our final catalog. Any CCD position dependent residuals are typically $0.3''$ or less. Once astrometric calibration is complete, we assemble a master catalog. In cases where an object falls in an overlap region between adjacent images, the object parameters used in the master catalog are chosen according to where the object lies with respect to the line bisecting the overlap region.

Figure 3 shows the distribution of the $\sim 710,000$ galaxies with $I \leq 23.5$ on the sky. In this figure, each galaxy is represented as a point with intensity proportional to $10^{-0.4m}$ where m is the isophotal I -band magnitude. The galaxy distribution in this figure incorporates the photometric and astrometric calibrations described above as well as the statistical correction for object misclassification described in §3.1. Blank rectangular areas are the regions excluded due to the presence of bright stars.

4. CLUSTER DETECTION

We use the matched filter algorithm developed by Postman et al. (1996) to detect and characterize cluster candidates in our survey. The algorithm employs flux and radial filters to optimize the contrast of a distant cluster projected on the sky. For details of the matched filter algorithm, and its variants, readers are referred to Postman et al. (1996); Schuecker & Boehringer (1998); Kepner et al. (1999); and Kim et al. (2001). In addition to detecting clusters, this algorithm provides a richness estimate, Λ_{CL} , and an estimated redshift for each candidate cluster. Λ_{CL} is the effective number of L^* galaxies in the cluster and within the cutoff radius of the radial filter. We have modified the computation of Λ_{CL} as proposed by Schuecker & Boehringer (1998) to minimize redshift dependent bias.

Cluster detection is run on an image that is a convolution of the matched filter, tuned to a specific redshift, with the galaxy catalog. Regions excluded from object detection (see §3) are also excluded from cluster detection. As in Postman et al. (1996), the matched filter is tuned to 11 different redshifts between 0.2 and 1.2 in 0.1 intervals. The estimated redshift is determined by choosing the redshift that maximizes the matched filter signal for a given detection. Any intrinsic cluster parameters (*e.g.*, Λ_{CL} , effective radius, etc.) are then determined for this redshift. The peak of the flux filter in magnitude-space depends on the assumed cluster galaxy luminosity function. Table 1 details the parameters used in our cluster detection process. We apply evolutionary and k -corrections to the assumed characteristic magnitude, m^* , that are appropriate for a passively evolving elliptical galaxy. Specifically, we assume $M^*(z) = M^*(z = 0) - z$, which is consistent with the observations of distant cluster ellipticals in Post-

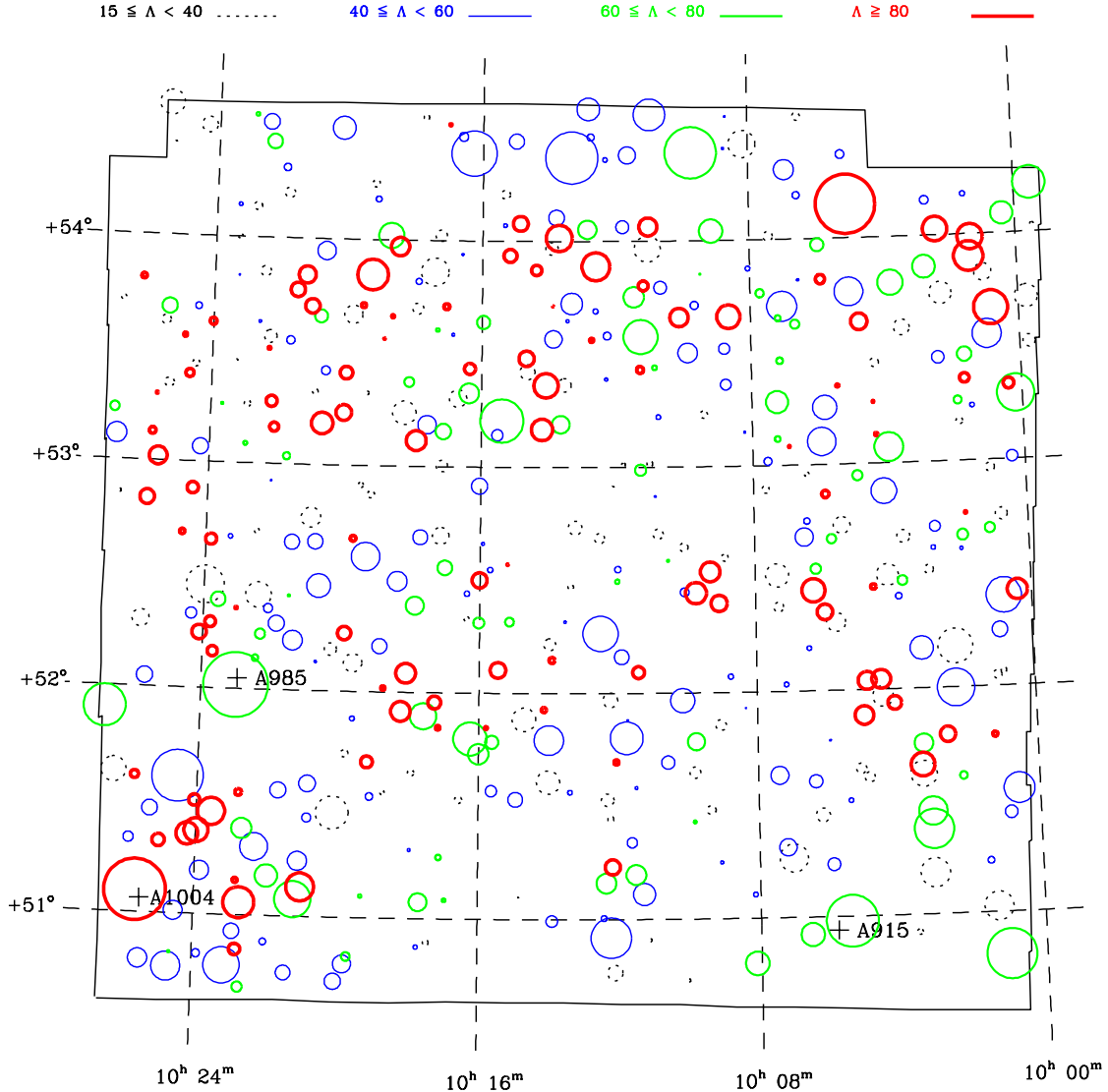
man, Oke, & Lubin (2001) and Fumiaki et al. (2001). The $z = 0$ M^* value in Table 1 is derived from R -band observations of low redshift clusters and transformed to the I -band using transformations in Frei & Gunn (1994).

Once cluster detection is complete, we minimize the problem of “deblended” clusters (*i.e.*, clusters detected multiple times due to substructure) by identifying cluster candidates whose effective radii overlap and whose estimated redshifts lie within $\Delta z = 0.2$. For each overlapping pair, we exclude from the final catalog the detection with the lower matched filter signal. Typically, this procedure reduces the size of the final cluster sample by $\sim 5 - 10\%$.

4.1. The Cluster Catalog

Table 2 lists the 444 cluster candidates in the Deeprange survey with a detection significance of 2σ or greater. As this a single passband survey, clearly many of the 2σ detections will be spurious. Visual inspection suggests that some higher z candidates ($z \gtrsim 0.8$) with detection levels in the $2 - 3\sigma$ range are likely to be real. We have thus opted for completeness over “cleanliness” in publishing this catalog. However, we fully characterize the false positive rate as a function of detection level, Λ_{CL} , effective radius, and redshift in §4.4. Users should carefully review that section before deciding what minimum detection significance, effective area, and cluster richness they wish to use. A sample of cluster candidates with a minimal number of false positives can easily be constructed by appropriately filtering on these parameters. Figure 4 shows the distribution of the cluster candidates on the sky. The radius of each circle is directly proportional to the cluster effective radius. The thickness and style of the circle line is determined by the Λ_{CL} estimate of the cluster.

A numeric cluster ID is given in column 1 of Table 2. The mean J2000 right ascension (h m s) and declination (d m s) of each cluster candidate are given in columns 2 through 7. The redshift estimate is given in column 8 and the Λ_{CL} value is given in column 9. Columns 10 through 13 contain four Abell-like richness parameters. The first, $N_{A,0.25}$, is the number of galaxies within a $333h_{75}^{-1}$ kpc radius that lie within m_3 and $m_3 + 2$, where m_3 is the statistically selected 3rd brightest cluster galaxy in this same radius. A statistical background subtraction, derived from galaxy counts in survey regions with no detected cluster candidates, is applied to all the Abell-like richness estimates. The m_3 value is given in column 16 of the table. The next Abell-like richness estimate is $N_{e,0.25}$ and is computed over the magnitude range m_{Eff} to $m_{Eff} + 2$, where m_{Eff} is the apparent magnitude at which the cluster is maximally enhanced over the background field. The m_{Eff} is derived by the matched filter algorithm and is given in column 17. The final two Abell-like richness estimates are $N_{A,0.5}$ and $N_{e,0.5}$, which are similar to those above except that the computations are done out to a radius of $666h_{75}^{-1}$ kpc (m_3 , however, is the value derived for the central $333h_{75}^{-1}$ kpc region). The significance of each detection (in σ units) is listed in column 14 and the effective radius (in arcseconds) is in column 15. The effective radius is $\sqrt{A_{MF}/\pi}$, where A_{MF} is the area of the detected signal in the match filtered image. Lastly, column 18 contains a visually assigned quality flag for all candidates with $\Lambda_{CL} \geq 50$. This flag is assigned by M.P. and is



ch

FIG. 4.— The distribution of cluster candidates on the sky. Circles denote the cluster position and their size is directly proportional to the cluster’s effective radius. Circle line thickness is related to the Λ_{CL} value. Dashed circles have $\Lambda_{CL} < 40$, thin-lined circles have $40 \leq \Lambda_{CL} < 60$, medium-lined circles have $60 \leq \Lambda_{CL} < 80$, and thick-lined circles have $\Lambda_{CL} \geq 80$. The survey boundaries are shown for reference. The locations of the 3 Abell clusters that lie within our survey are denoted by crosses along with their Abell ID number.

his attempt to assess the reality of each detection. A value of 3 indicates the cluster candidate is almost certainly real – a substantial galaxy enhancement is seen and the galaxies exhibit a pronounced central concentration similar to spectroscopically confirmed clusters at similar redshifts. A value of 2 indicates that the cluster candidate is likely to be real but may also be a compact group. A value of 1 indicates that the detection does not appear to have a strong central concentration of galaxies and may very well be spurious, a poor group, or deblended substructure from a nearby rich cluster. Use of the visual quality flag is meant for non-statistical analyses only.

4.2. The Selection Function

Meaningful astrophysical constraints can only be extracted from this cluster catalog when the selection function and false positive rate are well measured and a good calibration of the richness parameter, Λ_{CL} , is available. Implanting simulated clusters into the actual galaxy catalog is the most reliable method for determining the selection function and richness calibration. We have simulated over 17,000 clusters to obtain the required precision in our selection function and richness calibration. Specifically, we generate clusters spanning the ranges $10 \leq \Lambda_{CL} \leq 1000$, $0.2 \leq z \leq 1.2$. At each redshift and richness, we also create clusters dominated by an elliptical galaxy population and clusters dominated by an Sbc galaxy population. By this we mean that the evolutionary and k-corrections applied

are appropriate either for a passively evolving elliptical or Sbc dominated galaxy population. Clusters at $z \sim 1$ can exhibit spiral fractions that are 3 – 5 times larger than that seen in nearby clusters (*e.g.*, van Dokkum et al. 2001; Lubin et al. 1998; Lubin, Oke, Postman 2002). Finally, we also create clusters with surface density profile slopes of -1.0 , -1.4 , and -2.0 . The observed range in cluster profile slopes is typically $-1.6 \leq \gamma \leq -1$ (*e.g.*, Postman et al. 1988; Tyson & Fisher 1995; Lubin & Postman 1996; Squires et al. 1996). We have done the same for clusters with richness corresponding to Abell richness classes 0 through 4. These simulated cluster galaxies are inserted into the actual galaxy catalog in locations not occupied by real detected clusters. The cluster detection software is then run (using the identical detection parameters as in the real catalog) and we record the resulting Λ_{CL} , detection significance, and estimated redshift as well as the false negative rate. The selection function can then be computed as a function of all of these key parameters.

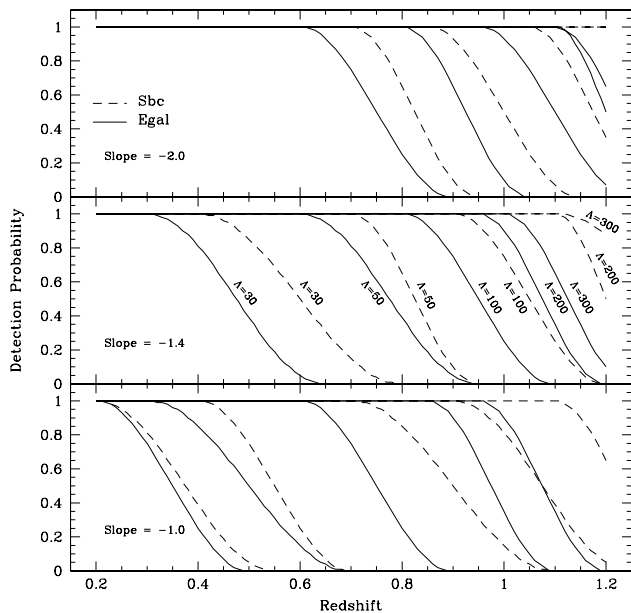


FIG. 5.— The cluster detection probability as a function of redshift, Λ_{CL} , cluster surface density profile slope, and galaxy spectral type. Results are explicitly shown for our $\Lambda_{CL} = 30, 50, 100, 200$, and 300 simulations. The solid curves are for the simulations using an elliptical dominated galaxy population. The dashed curves are for an Sbc dominated galaxy population. The Λ_{CL} values are explicitly labeled in the middle (slope = -1.4) panel. The order of the curves in the other panels is similar – for lower Λ_{CL} clusters, detection probabilities fall off at lower redshifts.

Figure 5 shows the cluster detection probability as a function of Λ_{CL} , profile slope, galaxy population, and redshift for all detections with significance $\geq 2\sigma$. The detection efficiency decreases with increasing redshift, decreasing richness, and decreasing star formation rate. Furthermore, clusters that are more centrally concentrated are detectable to higher redshifts than their more diffuse counterparts. The detection probability as a function of redshift for a given richness, galaxy population, and profile slope typically declines from 1 to 0 over a range $\Delta z \sim 0.2$. We use the selection functions computed above in all computations of cluster space density and in the estimation of

the Λ_{CL} distribution function.

4.3. Richness Calibration

There are essentially two methods to calibrate the richness parameter Λ_{CL} that enable us to compare our derived space densities with those from the Abell cluster catalog. The first method takes advantage of the extensive simulations performed to compute the selection function. These simulations provide two key results: the accuracy with which we recover the Λ_{CL} value of a given cluster and the relationship between Λ_{CL} and the Abell richness count. The relationship between Λ_{CL} and the Abell richness count can also be obtained empirically by processing known Abell clusters through our algorithm. For this empirical calibration to be most reliable, the imaging data of the Abell clusters should be identical to that in this survey. This would be time-intensive to perform for a large sample of Abell clusters. Fortunately, there are 3 Abell clusters in the survey boundaries (A915, A985, A1004) and these provide at least a rough reality check on the more precise calibrations provided by the simulations.

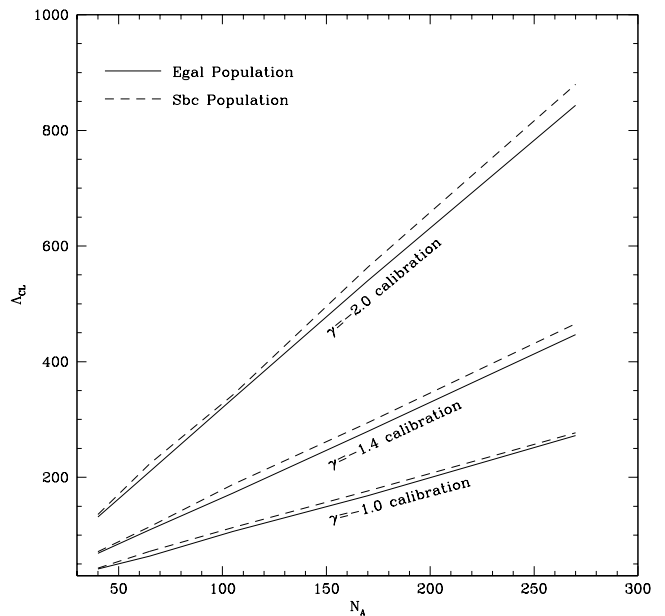


FIG. 6.— The relationship between Λ_{CL} and the Abell richness count, N_A , as estimated from simulated cluster data run through the matched filter algorithm. The simulations span the Abell richness class range $0 \leq RC \leq 4$ and are constructed using one of three different surface density profile slopes: $-1, -1.4, \text{ or } -2$.

We use the same simulation techniques used to compute the cluster selection function to create, insert, and measure the characteristics of clusters with known Abell richness classes. As in the selection function computations, we generate clusters with surface density profile slopes of $-1, -1.4, \text{ and } -2$ and with either Sbc or Elliptical dominated galaxy populations. The calibration is only weakly dependent on the galaxy type but is strongly dependent on the cluster profile slope. The slope dependence is largely a consequence of the use of a radial filter that weights centrally located cluster galaxies more than those at larger radii – a system with a steeper profile has relatively more

galaxies located near the cluster center than an equally massive cluster with a flatter profile. Figure 6 shows the derived Λ_{CL} values as a function of the Abell richness count, N_A , for simulated clusters with the 3 different profile slope values. The relationship between Λ_{CL} and N_A is linear for a given surface density profile. Taking the average between the Egal and Sbc calibrations, we find that a reasonable representation of the calibration between Λ_{CL} and N_A is

$$\Lambda_{CL} \approx f(\gamma)N_A \text{ where } f(\gamma) = 0.46 + 0.26\gamma + 0.81\gamma^2 \quad (5)$$

and where γ is the slope of the cluster surface density profile. Figure 7 shows a zoomed view of these relations with the actual data from the 3 Abell clusters superposed. The Abell cluster results lie in between the $\gamma = -1$ and $\gamma = -1.4$ calibration. The best-fit line (with a zero-valued intercept) to the cluster data in Figure 7 is

$$\Lambda_{CL} = 1.24N_A \quad (6)$$

corresponding to an average profile slope of $\gamma \sim -1.16$ (equation 5). This average is consistent with the actual slopes we measure for these 3 clusters: -1.23 ± 0.04 (A915), -1.00 ± 0.01 (A985), and -1.19 ± 0.02 (A1004). We thus adopt equation 6 as our nominal relationship between Λ_{CL} and N_A . The Abell clusters also provide a calibration of the Abell-like richness parameter, $N_{A,0.5}$, provided in Table 2. We find the relationship is $N_{A,0.5} \approx 0.44N_A$.

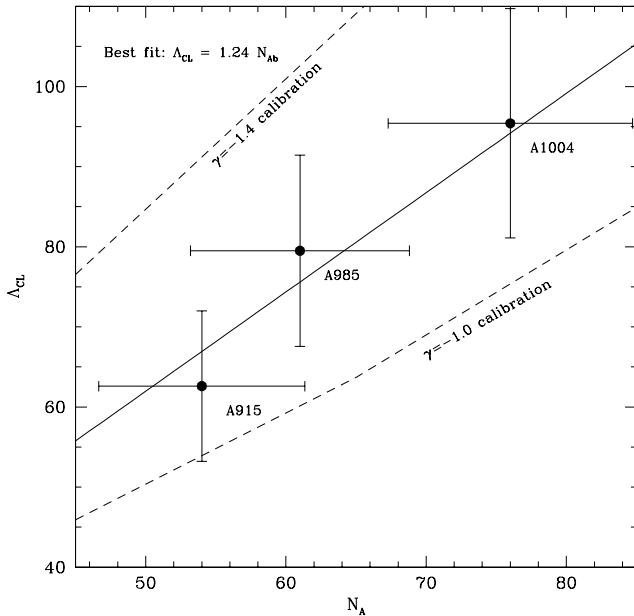


FIG. 7.— The empirical relationship between Λ_{CL} and N_A for Abell clusters A915, A985, and A1004. These 3 clusters lie wholly within the survey boundaries. The dashed lines show the same relations depicted in Figure 6. The solid line is the best-fit line with a zero-valued intercept. Errors in Λ_{CL} are $\pm 15\%$, as derived from our simulations. Errors in N_A are just $\sqrt{N_A}$.

Out to $z_{est} = 0.9$, we find that the typical error in Λ_{CL} is $\pm 15\%$. This is measured by comparing the known Λ_{CL} value from each simulated cluster at a given richness and redshift with the value computed by the matched filter algorithm. The Λ_{CL} uncertainties are insensitive to redshift in the range $0.2 \leq z_{est} \leq 0.9$. Beyond $z_{est} = 0.9$, the corrections used to compensate for the truncation of the

flux filter by the survey flux limit become quite sizeable and the errors in Λ_{CL} can reach 40% (see section 4.1 in Postman et al. (1996) for details). Our Λ_{CL} values are thus most reliable for those candidates with $z_{est} \lesssim 0.9$.

4.4. False Positive Rates

There are two basic sources for false positive detections in this survey: random fluctuations of field galaxies and chance alignments of poor groups of galaxies. The false positive rate for random fluctuations in the galaxy distribution can be assessed by creating simulations that contain no clusters but that have an angular two point correlation function similar to the galaxies in the real universe. We generate such simulations using a Rayleigh-Levy galaxy pair separation distribution: $P(> \theta) = (\theta/\theta_o)^{-d}$ if $\theta \geq \theta_o$ and $P(> \theta) = 1$ if $\theta < \theta_o$. To construct the clustered galaxy distribution, we randomly select a starting position within the survey boundaries and then generate galaxy positions about this center using the above separation distribution. We allow up to 7 galaxies to be so distributed about a given center. The results below are not very sensitive to this choice so long as the number is more than 2 and less than 15. A new center is then randomly chosen and the process repeated until the number of galaxies matches the observed number. The values of θ_o , d are chosen to match the observed $\omega(\theta)$ derived from this survey as best as possible (Postman et al. 1998). We then run the matched filter algorithm on these clusterless fields using the identical detection parameters as in the real survey. Figure 8 shows the resulting

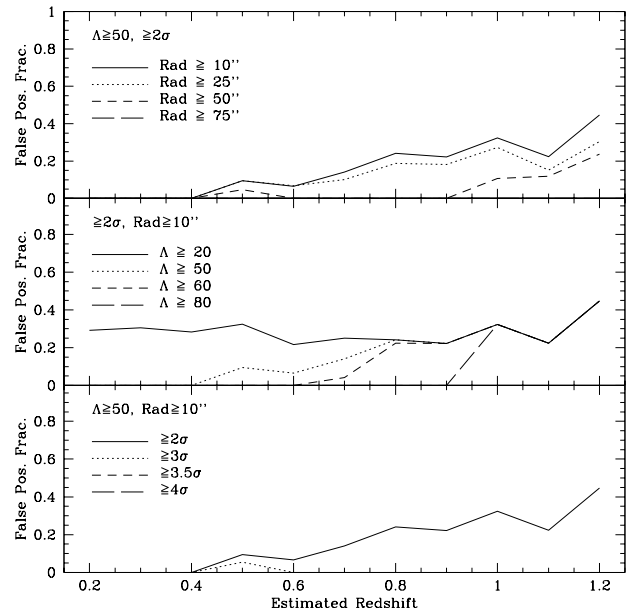


FIG. 8.— The fraction of detections that could be spurious as a function of redshift, richness, detection significance, and effective radius. These results are obtained by running the matched filter algorithm on simulated fields with a non-zero two point correlation function but with no clusters. The false positive fraction value is computed by dividing the surface density of detections in these simulations by the observed surface density of cluster candidates in the actual survey.

false positive fractions as functions of estimated redshift,

Λ_{CL} , detection significance, and effective radius. The false positive fraction is the number of detections in the clustered simulation (per square degree) divided by the observed number of cluster candidates (per square degree) found in the actual survey. These simulations predict that a sample of cluster candidates with $\Lambda_{CL} \geq 20$, $\sigma \geq 2$, and effective radii $\geq 10''$ will suffer a false positive rate between 10% to 40% depending on the redshift. The vast majority of these spurious detections lie at the low end of the Λ_{CL} distribution and tend to also be small in size. Table 3 shows how the number of clusters in the survey varies with the minimum Λ_{CL} , σ , and effective radius. Users who wish to work with a catalog that contains a minimum number of spurious detections should use candidates with $\Lambda_{CL} \geq 60$, $\sigma > 3$, and effective radii $\geq 60''$. Such a sample should have few spurious detections due to large positive fluctuations in the field galaxy distribution. Note, however, that such selection criteria will significantly reduce the number of high redshift candidates in the sample.

Approximately 70 to 80% of the cluster candidates with $z_{est} \lesssim 0.7$ are most likely physically real galaxy associations. The false positive rate for candidates with $z_{est} > 0.7$ will be assumed to be $\sim 30 - 40\%$ for the purposes of computing true cluster space density estimates. We note that the use of simulations with non-zero angular two point correlation functions is essential in accurately estimating false positive rates. Simulations with purely random galaxy distributions yield false positive rates that are an order of magnitude smaller than that observed in the clustered simulations and in the actual data.

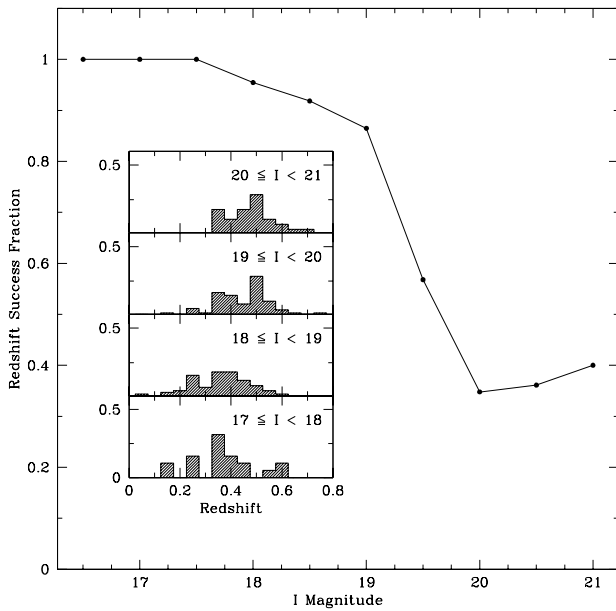


FIG. 9.— The fraction of galaxies for which redshifts were successfully measured as a function of the isophotal I -band magnitude. Inserts show the redshift histograms in four magnitude bins.

5. SPECTROSCOPIC FOLLOW-UP

Assessing the occurrence of spurious detections due to the chance radial alignment of physically unrelated groups

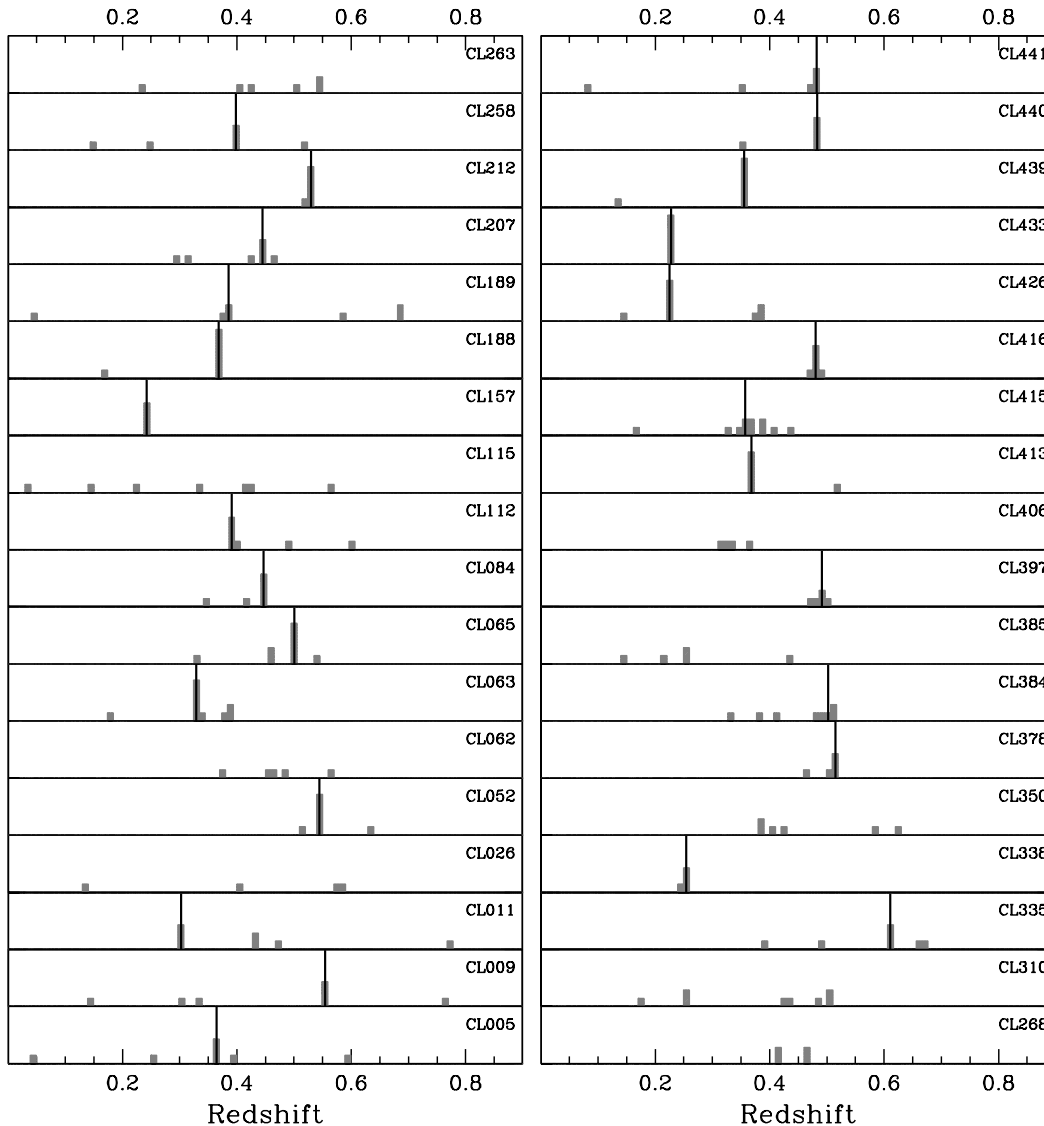
⁷ Highest priority was given to galaxies that fell within ± 0.5 mag of the effective cluster magnitude derived by the matched filter algorithm.

of galaxies (or edge-on sheets of galaxies) is best addressed by spectroscopic follow-up of a well selected subset. Indeed, a spectroscopic survey enables one to measure the overall spurious detection rate due to both random fluctuations and chance alignments. Such a follow-up survey was begun in December 1998 and we find that up to $z = 0.6$ the false positive rate is $\sim 25\%$. This rate includes all spurious detections regardless of their nature. It is in excellent agreement with that predicted by the simulations above. The scientific motivation for this spectroscopic survey is to measure the 3D cluster-cluster correlation function at $z \sim 0.5$. To achieve this goal, we set out to obtain spectra for galaxies in the 141 clusters with $0.3 \leq z_{est} \leq 0.7$ and $\Lambda_{CL} \geq 50$. As of March 2001, we have observed 36 clusters.

We have had a total of 6 spectroscopic observing runs on the KPNO 4m telescope. The first 4 runs (Dec 1998, Feb 1999, Jan 2000, Mar 2000) used the Cryocam spectrograph. The Cryocam suffered a mechanical failure in March 2000 and our subsequent observations (Jan 2001, Mar 2001) were performed with the less efficient RC spectrograph. Both spectrographs were used with the BL-181 grating to provide low resolution ($7 - 10\text{\AA}$) spectra over the range $4200 - 9500\text{\AA}$. We visually selected likely cluster members⁷ within 2.5 arcminutes from the cluster center (the Cryocam field of view is 5 arcminutes) using our I -band images. KPNO provided software that was then used to create slit mask templates. We produced one mask per cluster and the masks typically contained between 8 to 12 slits (a slit width of 2 arcseconds was used).

We always obtained at least 2 exposures per cluster and, more typically, 3 to 4 exposures. Depending on the estimated cluster redshift and the observing conditions, the combined exposure times range from 3600 seconds (for a $z_{est} = 0.3$ cluster observed with Cryocam in clear weather with good seeing) to 9500 seconds (for a $z_{est} = 0.5$ cluster observed with RCSpec in less than ideal conditions). The accuracy of our astrometry proved sufficient to assure successful centering of galaxy targets in their slits but we note that the use of check and setup stars was critical in achieving this good alignment. The KPNO-4m+Cryocam/RCSpec are well suited to obtaining redshifts for systems with $z_{est} < 0.6$ but the availability of an imaging spectrograph at NOAO would significantly increase the efficiency of obtaining such observations. The relatively modest productivity of our spectroscopic program (36 clusters over 2.3 years) is largely due to weather related problems. None the less, we did succeed in completing the observations for all clusters with $0.3 \leq z_{est} < 0.5$. Acquiring redshifts efficiently for the more distant component of our sample (81 clusters with $z_{est} \geq 0.6$) will require a 6 - 8m class telescope.

The spectroscopic data were extracted and calibrated using standard IRAF longslit packages. We did observe small sub-pixel shifts in the sky line positions between subsequent Cryocam exposures of the same target. This required that the multiple exposures be co-added *after* extraction and wavelength calibration. The RC Spectrograph data were more stable and thus could be co-added prior to spectral extraction and calibration.



ch

FIG. 10.— The redshift distributions for the 36 clusters candidates observed in our spectroscopic follow-up survey. Of the 36, 9 are probably spurious or superpositions of poor groups. The vertical lines indicate the adopted mean cluster redshift, when a reliable mean can be determined.

5.1. Galaxy and Cluster Redshift Determination

Galaxy redshifts were derived using the IRAF package *xsao*. We used 8 independent high S/N templates of elliptical galaxies to perform the cross-correlations. Regions around prominent night sky lines (Hg, NaD, OI) and strong atmospheric OH absorption bands were excluded from the fitting procedure. A galaxy redshift was computed by averaging the results for those templates that lie within 250 km s^{-1} of the mode. For a high S/N spectrum, all 8 templates are in agreement. If fewer than 4 templates are found to agree, the spectrum is deemed unusable for redshift determination. Of the 352 spectra that were obtained, we were able to derive reliable redshifts for 230. The remaining spectra had insufficient S/N. Figure 9 shows the redshift measurement success rate as a function

of *I*-band magnitude along with redshift histograms as a function of magnitude. All spectra were visually inspected as well to assure the resultant redshift was sensible. Approximately 10% of all the spectra exhibited emission features and redshifts for these galaxies were determined using the IRAF package *roidlines*. Table 4 gives the positions, *I*-band magnitudes, redshifts and redshift errors for all the observed objects.

Cluster redshifts are derived by looking for “clumps” in redshift that are not wider than 3000 km s^{-1} in the rest frame. If at least 3 galaxies can be identified in such a clump, we average their redshifts to compute a mean value for the cluster. The results are listed in Table 5 and displayed in Figure 10. Of the 36 clusters observed, two (CL415 and CL426) appear to be superpositions of

two systems. In both cases, however, one of the spikes in redshift contains 5 concordant redshifts indicating the presence of a real cluster. For 6 of the 36 clusters (CL026, CL062, CL115, CL263, CL268, CL385), no reliable redshift could be derived because no clump of 3 or more concordant redshifts was identified or because the S/N of the spectra for most of the objects was too low. Finally, for 3 of the clusters (CL310, CL350, CL406) a “clump” of 3 redshifts exists but is just larger than $\sim 3000 \text{ km s}^{-1}$ in width. If we assume all 9 of these cluster candidates are spurious, then our matched filter algorithm is finding real physical systems $\sim 75\%$ of the time (at least out to $z \sim 0.6$), in accord with other studies (Holden et al. 1997) and with simulations done in this paper and by Postman et al. (1996).

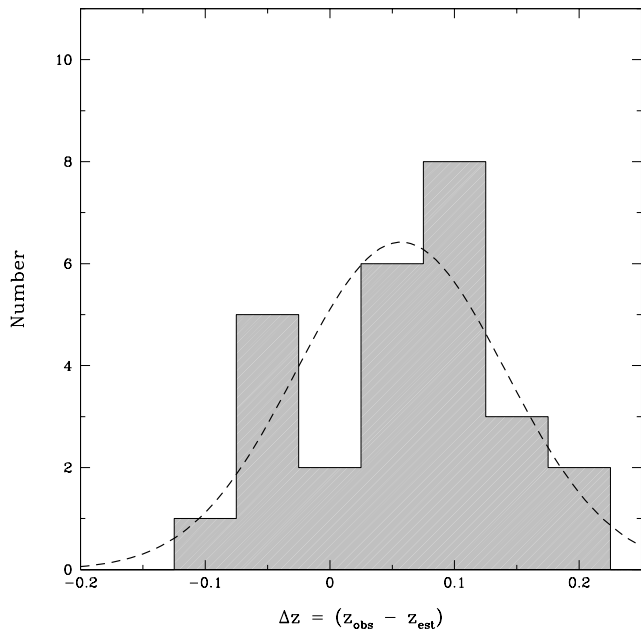


FIG. 11.— The distribution of differences between the observed spectroscopically derived cluster redshift and the redshift estimate derived from the matched filter algorithm. The data are derived from the 27 clusters with 3 or more concordant redshifts within $\pm 1500 \text{ km s}^{-1}$. The best fit Gaussian representation of the distribution ($\overline{\Delta z} = +0.057$, $\sigma_z = 0.084$) is also shown.

5.2. Comparison with Estimated Redshifts

The accuracy of the matched filter redshift estimates depends largely on the accuracy of our cluster luminosity function model. Figure 11 shows the redshift difference histogram ($\Delta z = z_{\text{obs}} - z_{\text{est}}$) for the 27 clusters for which reliable mean redshifts could be measured. The mean offset ($\overline{\Delta z}$) is 0.057 with an rms scatter (σ_z) of 0.084. These statistics are largely independent of the redshift estimate over the range $0.3 \leq z_{\text{est}} \leq 0.5$. The relatively good agreement between the observed and estimated redshifts indicates that our cluster LF model is reasonable and further suggests that the characteristic cluster galaxy magnitude is a reasonably reliable ($\pm 20\%$) distance indicator. The slight positive offset of the Δz distribution can possibly be attributed to a small underestimate in the assumed characteristic luminosity, L^* . However, the offset is smaller than the 0.1 interval used to estimate redshifts. Spectroscopic follow-up of clusters in the Palomar Distant Cluster

survey (Holden et al. 2000) suggests that the scatter observed above increases a bit at higher redshifts ($z \lesssim 0.8$): for 7 PDCS clusters with $0.5 \leq z_{\text{est}} \leq 0.8$ $\sigma_z = 0.16$. This is consistent with the growth in the expected systematic errors with redshift (see §6.2) but is still small enough that reliable space density estimates can be established.

6. RESULTS

The abundance of galaxy clusters as a function of redshift and mass is a critical constraint on cosmological models and models for cluster formation and evolution. With an accurate construction of the selection functions, Λ_{CL} calibration, and false positive rates complete, we can now use our observations to constrain the observed space density of optically selected clusters up to $z \sim 1$.

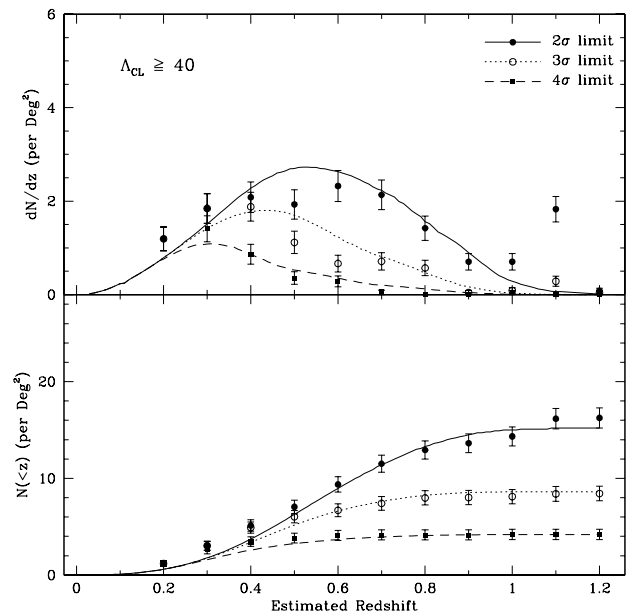


FIG. 12.— The differential and cumulative surface densities of clusters as functions of estimated redshift and detection significance for systems with $\Lambda_{CL} \geq 40$. The surface densities have been corrected for false positive detections. The curves show the predicted relations for a constant comoving space density of clusters multiplied by the relevant selection functions. The best-fit constant comoving density (for $\Omega_m = 0.2$, $\Lambda = 0$) that matches the surface density observations is $(1.57 \pm 0.15) \times 10^{-5} h_{75}^3 \text{ Mpc}^{-3}$, ~ 1.3 times the local space density of $\text{RC} \geq 0$ Abell clusters.

6.1. The Surface Density of Clusters vs Redshift

The differential and cumulative surface density of $\Lambda_{CL} \geq 40$ cluster candidates as functions of redshift and detection threshold are shown in Figure 12. The measured counts have been corrected for the expected false positive rates. The continuous curves in this figure are the predictions for a constant comoving space density of clusters multiplied by the appropriate selection functions. We also assume that the relative abundances of clusters of different richness classes remain independent of redshift. We adopt De Propris et al. (2002) estimates of the space density of Abell clusters: $(1.17 \pm 0.12) \times 10^{-5} h_{75}^3 \text{ Mpc}^{-3}$ for $\text{RC} \geq 0$ and $(3.80 \pm 0.72) \times 10^{-6} h_{75}^3 \text{ Mpc}^{-3}$ for $\text{RC} \geq 1$. For $\text{RC} \geq 2$, we assembled a compilation of redshifts, including data from the MX Survey (Slingsend et al. 1998)

and the 2dF Survey (De Propris et al. 2002), and derived our own space density estimate of $9.16 \times 10^{-7} h_{75}^3 \text{ Mpc}^{-3}$ based on a sample of 60 Abell clusters with observed redshifts $z \leq 0.1$ and $|b| \geq 40^\circ$. The good agreement between the observed cluster surface densities and those predicted by our convolution of the selection functions with a constant comoving space density supports the hypothesis that there is little evolution in the comoving space density of clusters over the range $0 < z < 0.8$. The constant comoving space density that best fits the surface density data is $(1.57 \pm 0.15) \times 10^{-5} h_{75}^3 \text{ Mpc}^{-3}$, about 1.3 times the mean space density of local $\text{RC} \geq 0$ Abell clusters. From equation 6, we find that $\Lambda_{CL} > 40$ is approximately equivalent to $N_A > 30$, which is the Abell $\text{RC} = 0$ threshold. The Deeprange cluster surface densities are consistent with those found in other optical surveys using the matched filter (*e.g.*, PDCS (Postman et al. 1996) and EIS (Olsen et al. 1999)). The EIS and PDCS both find cluster surface densities in the range $5 - 10 \text{ deg}^{-2}$ for $z_{est} \leq 0.7$ and $\Lambda_{CL} \geq 40$. The ratio of the space density of distant clusters to that for the Abell catalog is, however, significantly less than that reported by Postman et al. (1996) for the Palomar Distant Cluster Survey. We believe the difference between the current results and those from the PDCS is a result of the more accurate Λ_{CL} - Abell richness calibration used here, improved measurements of the local cluster space density (Postman et al. 1996 used rather out-of-date estimates of the Abell cluster densities based on results in Bahcall 1979), and the significantly larger contiguous survey area, which enables a more reliable measurement of the mean density level. As we will demonstrate below, the somewhat larger space density of poor clusters in our survey relative to the Abell catalog is attributed to incompleteness at the low richness end of the Abell catalog.

The good agreement between the observed and predicted cumulative cluster surface density also implies that we can reliably divide out the signature of the selection function to obtain a constraint on the true cumulative cluster surface density. The results of this computation are provided in Table 6. Table 6 also lists the effective survey area as a function of redshift. The survey area is a weak function of redshift because about 3% of the CCD images have a limiting magnitude above that needed to detect clusters out to $z_{est} = 1.0$ and about 20% have insufficient depth to detect clusters in the range $1 < z_{est} \leq 1.2$.

6.2. The Space Density of Clusters

We use the estimated redshifts in the full catalog to derive the space density of clusters as a function of redshift. At each redshift, the space density is

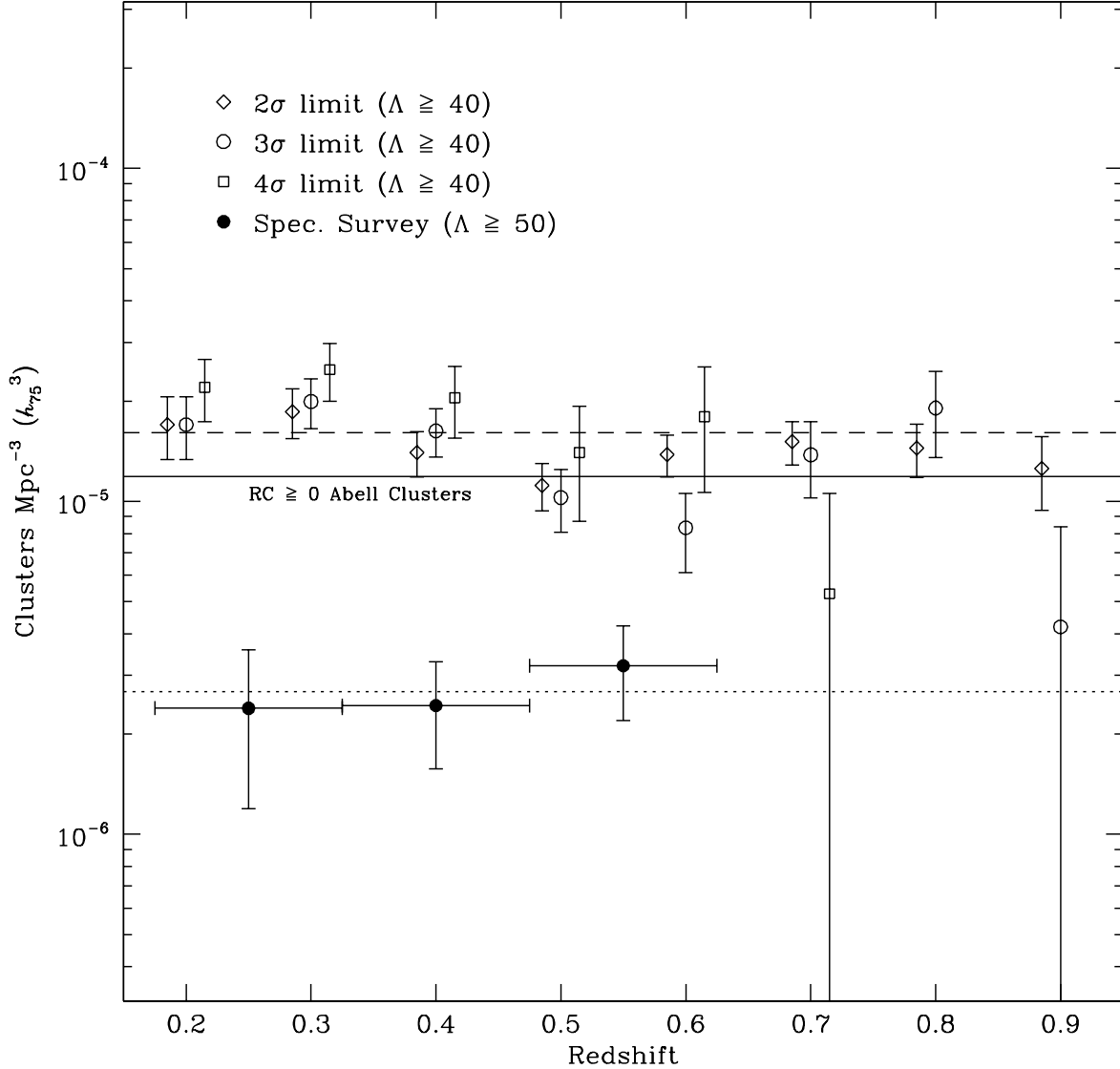
$$\rho(z) = \left(\sum_{k=1}^{N_{CL}(z)} 1/P_k(z) - N_{spur}(z) \right) / \int_{z-\Delta z/2}^{z+\Delta z/2} \Omega(z) dV \quad (7)$$

where $P(z)$ is the probability of detecting a cluster with a given Λ_{CL} and detection threshold at redshift z , $N_{CL}(z)$ is the number of clusters found with estimated redshift between $z - \Delta z/2$ and $z + \Delta z/2$, $N_{spur}(z)$ is the mean number of false positive detections expected in this same redshift interval, $\Omega(z)$ is the effective area subtended by the survey at redshift z , and dV is the unit comoving volume element. The width of the redshift bins, Δz , is 0.1.

Figure 13 shows the space density of $\Lambda_{CL} \geq 40$ clusters as a function of redshift and detection significance. The minimal dependence of the cluster space density on detection significance is a tribute to the accuracy of the selection functions - weighting the cluster counts by the inverse of the detection probability effectively removes the artificial decline in space density introduced by the decreasing significance of the cluster detections with increasing redshift. The mean space density of $\Lambda_{CL} \geq 40$ clusters, in the range $0.2 \leq z_{est} < 1$, is $(1.61 \pm 0.24) \times 10^{-5} h_{75}^3 \text{ Mpc}^{-3}$, in excellent agreement with the best-fit space density obtained in §6.1. The mean V/V_{max} value (Schmidt 1968) for the $\Lambda_{CL} \geq 40, \sigma \geq 3.0$ cluster sample is 0.54, suggesting that the spatial distribution of clusters in this sample is close to uniform and, thus, the space densities derived from it are representative of the full redshift range. The observed comoving cluster space density is consistent with little or no evolution over the redshift range $0.2 < z < 0.8$. Attempting to fit an exponentially decaying space density to the data allows us to place an upper limit to any density evolution. A drop in space density of greater than a factor of 3 over the above redshift range is ruled out at greater than the 99.9% confidence level for the sample of clusters with $\Lambda_{CL} \geq 40, \sigma \geq 3$.

Figure 13 also shows the space density of $\Lambda_{CL} \geq 50$ clusters that have 4 or more concordant spectroscopic redshifts. The mean space density for these 22 clusters is $(2.68 \pm 1.05) \times 10^{-6} h_{75}^3 \text{ Mpc}^{-3}$. If we include those clusters with at least 3 concordant redshifts, then the mean space density becomes $(3.38 \pm 1.17) \times 10^{-6} h_{75}^3 \text{ Mpc}^{-3}$. These densities differ by a factor of ~ 3 from the result obtained using the full $\Lambda_{CL} \geq 50$ sample with estimated redshifts: $(8.80 \pm 0.13) \times 10^{-6} h_{75}^3 \text{ Mpc}^{-3}$. About 80% of the difference is due to the significant volume underestimation that results from deriving the space density for a sample spanning a very narrow range of estimated redshifts. If we recompute the space density of the spectroscopically observed clusters using their estimated redshifts instead, we derive density that is 2.4 times higher than the space density derived using the spectroscopic redshifts. This systematic error is a direct consequence of the moderate uncertainties in the redshift estimates and was discussed originally in Postman et al. (1996). The 27 clusters with existing redshifts in the spectroscopic followup survey all have estimated redshifts of either 0.3 or 0.4, yet their spectroscopic redshifts span the range $0.225 \leq z \leq 0.611$. The remaining difference ($\sim 20\%$) is probably due to small uncertainties in our false positive rate corrections and incompleteness in our spectroscopic survey (the S/N ratios of the spectra in 3 of the 36 cluster candidates in the spectroscopic survey were too low to derive redshifts).

In general, the effect of uncertainties in the estimated redshift and uncertainties in Λ_{CL} conspire to inflate the derived abundance of clusters by some amount that is dependent on the amplitude of these uncertainties. This is largely due to an asymmetry in the number of clusters that are scattered into a given estimated redshift bin versus the number scattered out. However, the above factor of ~ 2.4 volume underestimate is not applicable across the full estimated redshift range $0.2 \leq z_{est} \leq 1.2$. Monte Carlo simulations we have performed indicate that the mean space density derived from a sample that covers an estimated



ch

FIG. 13.— The space density of clusters as a function of redshift. The open diamonds, circles, and squares show the space density as a function of estimated redshift for all cluster candidates with $\Lambda_{CL} \geq 40$ and with detection thresholds of 2, 3, and 4 σ , respectively. These data have been divided by the appropriate selection functions and corrected for the expected false positive rates. The data points for the 2 and 4 sigma results are intentionally offset (by ± 0.015 in z) for clarity. The solid circles show the space density averaged into 3 redshift bins for the 22 $\Lambda_{CL} \geq 50$ clusters with 4 or more concordant spectroscopic redshifts. The long-dashed line is the mean space density for the $\Lambda_{CL} \geq 40$ subsample, the short-dashed line is the mean space density for the spectroscopic sample. The solid line is the mean space density of $RC \geq 0$ Abell clusters.

redshift range of at least 5 times the rms scatter in the $(z_{obs} - z_{est})$ values should be no more than $\sim 15\%$ larger than the true space density. We have corrected all our space density estimates downward accordingly to account for this effect. The spectroscopic sample only spans an estimated redshift range that is comparable to this rms scatter (see §5.2) and, thus, the significant volume underestimate resulting from use of the estimated redshifts is fully expected. The corrected mean space density derived from the full survey ($0.2 \leq z_{est} \leq 1.2$) should, therefore, be relatively free from systematic error unless the rms scatter in the estimated redshifts is significantly larger than 0.2

– and this is not supported by existing spectroscopic data (see §5.2).

6.3. The Lambda Function and Cluster Mass Estimation

The dependence of the space density of clusters on Λ_{CL} is equally as important as its redshift dependence. In the absence of an accurate mass estimate for each cluster, the Λ_{CL} function can provide a proxy for the mass function if the mass-to-light ratio on cluster scales is relatively invariant or if the Λ_{CL} value is based on a rest-wavelength that traces the integrated stellar mass in the cluster galaxies. In the case of the Deeprange survey, the latter is certainly

not the case for redshifts higher than $z \sim 0.4$. Nonetheless, the relative abundance of clusters as a function of Λ_{CL} can be used to provide a crude constraint on the typical mass of the ensemble of clusters in the survey, as discussed at the end of this section.

We use the same procedures for computing the differential Λ_{CL} function as in Donahue et al. (2001) for the ROSAT Optical X-Ray Survey (ROXS). In our case, we calculate the Λ_{CL} function for the subset of 217 cluster candidates with detection significance $> 3\sigma$ and $\Lambda_{CL} \geq 20$. The data and best-fit are shown in the lower panel of Figure 14. The data points shown are the binned values in 14 equal sized $\Delta\Lambda_{CL} = 10$ intervals such that $dN/d\Lambda_{CL} = \sum_i 1/V_{max,i}$ where V_{max} is the maximum volume at which a cluster could have been detected in our survey. The V_{max} for a given cluster is computed by integrating the cosmological comoving volume element dV multiplied by the appropriate detection probability function. For this purpose, the Λ_{CL} -dependent selection functions (see Figure 5) were interpolated to span the range of Λ_{CL} values in the above subsample.

In order to characterize the general shape and normalization of the Λ_{CL} function, the unbinned Λ_{CL} and estimated redshift data were fit to a simple power law of the form $dN/d\Lambda_{CL} = N_0(\Lambda_{CL}/40)^{-\alpha}$, where the normalization N_0 and the slope α were the sole parameters of the fit. We compute a likelihood function $S(\alpha, N_0)$ (Marshall et al. 1983) defined by

$$S(\alpha, N_0) = 2 \int N_0(\Lambda_{CL}/40)^{-\alpha} f(\Lambda_{CL}, z) d\Lambda_{CL} dV - 2 \log \mathcal{N} \quad (8)$$

where \mathcal{N} is a sum of all k cluster candidates (appropriately weighted to account for the expected false positive rate) such that $\mathcal{N} = \sum_k N_0(\Lambda_{CL,k}/40)^{-\alpha}$ and $f(\Lambda_{CL}, z)$ is the normalized selection function (Figure 5) assuming elliptical-like passive evolution and a cluster profile slope of $\gamma = -1.4$. The best-fit function for the 217 clusters with detection significance of at least 3σ and $\Lambda_{CL} \geq 20$ is

$$dN/d\Lambda_{CL} = (1.55 \pm 0.40) \times 10^{-6} (\Lambda_{CL}/40)^{-4.40 \pm 0.30} \quad (9)$$

The units of dN are $h_{75}^3 \text{ Mpc}^{-3}$, Λ_{CL} is dimensionless. The uncertainties in the normalization and slope are statistical only and do not include systematic uncertainties associated with false positive rates, volume/redshift estimates, and Λ_{CL} . We further caution that the best-fit is not intended for extrapolation beyond the redshift or Λ_{CL} ranges spanned by the data in Figure 14.

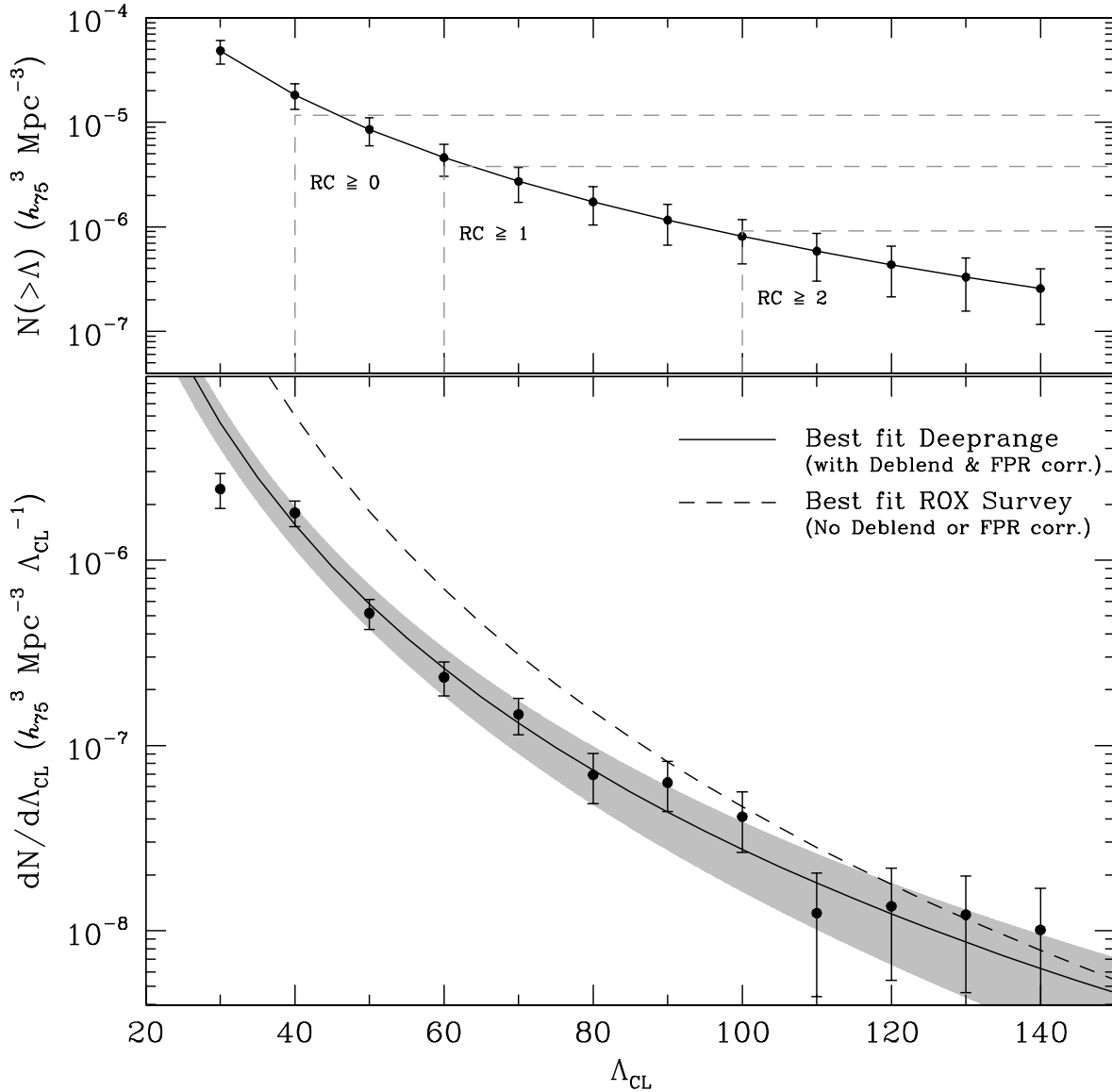
Formally, the ROXS data (Donahue et al. 2001) resulted in a steeper Λ_{CL} function ($\alpha = 4.8 - 5.8, 1\sigma$) with higher normalization at $\Lambda_{CL} = 40$ (by factor of ~ 2). The difference is largely for cluster candidates in the $\Lambda_{CL} < 60$ range and is most likely due to differences in the processing of the ROXS data – Donahue et al. (2001) do not correct their counts for false positive detections nor do they “deblend” their cluster detections, which results in a higher number of low- Λ_{CL} systems in their catalog. Our Λ_{CL} function fit is not inconsistent with the ROXS data, however. The slopes of the two Lambda functions differ by a formal uncertainty of 2σ . Since most of the systematic uncertainties in the data induce dispersion, the discrepancy between the two Λ_{CL} function fits is, in fact, less significant than 2σ .

The cumulative cluster space densities, $N(\geq \Lambda_{CL})$, derived by integrating equation 9 agree with those derived in §6.1 and §6.2 to within $\pm 25\%$, well within the statistical uncertainties of the fit. For $\Lambda_{CL} \geq 40$, the integration yields a space density of $(1.83 \pm 0.50) \times 10^{-5} h_{75}^3 \text{ Mpc}^{-3}$, about 1.6 times the density of Abell RC ≥ 0 clusters. Table 7 lists the integrated space densities as a function of Λ_{CL} and these data are plotted in the upper panel of Figure 14. Our $\Lambda_{CL} \geq 40$ space density is also consistent with that seen in recent x-ray selected surveys for local clusters. For example, integrating the Ebeling et al. (1997) bolometric x-ray luminosity function one obtains a space density of $1.57 \times 10^{-5} h_{75}^3 \text{ Mpc}^{-3}$ for clusters with $L_x \geq 2.25 \times 10^{43} h_{75}^{-2} \text{ erg s}^{-1}$, the typical x-ray luminosity for a $\Lambda_{CL} = 50$ cluster (Donahue et al. 2001). Our calibration of the $\Lambda_{CL} - N_A$ relation predicts that $\Lambda_{CL} \geq 40$ corresponds to RC ≥ 0 and the uncertainties in our false positive rate correction are no larger than 20%. Therefore, the most probable explanation for the lower space density of Abell clusters is likely to be attributed to incompleteness in low richness end of the Abell catalog. The space density of $\Lambda_{CL} \geq 60$ clusters in our survey agrees with the local space density RC ≥ 1 Abell clusters to within 20%. The cumulative Abell cluster space densities for richness class RC ≥ 0 , RC ≥ 1 , and RC ≥ 2 are displayed in the upper panel of Figure 14 as dashed lines.

We can use the Λ_{CL} function to obtain approximate estimates of the typical cluster mass as a function Λ_{CL} . The relation between Λ_{CL} and mass is expected to be noisy (Donahue et al. 2001, 2002). As such, one cannot reliably take a Λ_{CL} value for an individual cluster and expect to derive an accurate mass. One can, however, attempt to provide an estimate of the typical mass for a large ensemble of clusters in at least two independent ways. In the first method, we compute the average Λ_{CL} value for a subset of clusters, derive the corresponding average intrinsic luminosity (recall that Λ_{CL} corresponds to the effective number of L^* galaxies within the cutoff radius used in the matched filter), correct this luminosity for the finite radius used, and multiply the corrected luminosity by an assumed M/L ratio to obtain a mean mass estimate corresponding to the mean Λ_{CL} . The second method involves deriving a predicted mass function using Press-Schechter formalism for a given cosmological model and finding the correspondence between the densities in the model with the observed cluster space densities (*e.g.*, Table 7).

We use the first method to derive mass estimates for clusters with $\Lambda_{CL} \geq 40, 60$, and 100, respectively, which correspond approximately to the Abell richness class limits $\geq 0, \geq 1$, and ≥ 2 . The mean Λ_{CL} values for these three samples are 57, 85, and 141. We convert these mean Λ_{CL} values to absolute luminosities using our adopted M_I^* value of $-21.90 (2.1 \times 10^{10} h_{75}^{-2} L_{\odot})$ and multiply by a factor of 1.05 to correct for the finite radius⁸ of the matched filter. The finite radius correction factor is, however, considerably smaller than the uncertainties in the M/L ratio. If $\Omega_m = 0.2$, then the typical M/L ratio on cluster scales in the I -band should be ~ 200 , based on the luminosity function parameters presented in Blanton et al. (2001). If the M/L is independent of mass, then we find

⁸ For a de-projected density profile with a core radius of 133 kpc, the ratio between the integrated mass at infinite radius and that at the matched filter cutoff radius is 1.02 and 1.07 for profile slopes of -2.4 and -2.0, respectively.



ch

FIG. 14.— **Lower panel:** The differential space density of clusters as a function of Λ_{CL} for the subset of cluster candidates detected with at least a 3σ significance. The cluster counts are weighted by the appropriate selection function and corrected for the expected false positive rate. The grey shaded region shows the 1σ confidence limits on the best-fit power-law relation. The best-fit from the ROXS data are shown for comparison. The difference between our result and the ROXS data is understood and discussed in §6.3. **Upper Panel:** The integrated space density of clusters derived from the best-fit power-law to the Deeprange data in the lower panel. The dashed lines correspond to the observed Abell cluster space densities as a function of richness.

that the typical cluster masses for $\Lambda_{CL} \geq 40$, 60, and 100 are $2.5 \times 10^{14} M_{\odot}$, $3.7 \times 10^{14} M_{\odot}$, and $6.2 \times 10^{14} M_{\odot}$, respectively. If the M/L increases with cluster mass as $M/L \propto M^{\sim 0.5}$ (Hradecky et al. 2000; Donahue et al. 2001) then the mass estimates above would be correspondingly higher by $\sim 60 - 160\%$.

In the second method, a Press-Schechter mass-function is derived from the approximation developed by Pen (1998) for a flat-universe with $\Omega_m = 0.3$, $\Omega_b h^2 = 0.0205$ (O’Meara et al. 2001), $h = 0.75$, and $\sigma_8 = 1.0$, which is consistent results from cluster abundance constraints (e.g., Moscardini et al. 2001). In this model, $N(> M) = 10^{-6} h_{75}^3 \text{ Mpc}^{-3}$ when $M \approx 3 \times 10^{14} M_{\odot}$. This would correspond to the

observed cluster density when $\Lambda_{CL} \gtrsim 90$. This mass scale is in good agreement with that derived in the first approach. While quite approximate, both approaches suggest that the average mass of a $\Lambda_{CL} \geq 40$ cluster is in the few $\times 10^{14} M_{\odot}$ range, albeit the scatter about this mean value is expected to be substantial.

6.4. Superclusters at Intermediate Redshifts

We have identified at least 2 potential superclusters from our spectroscopic survey data. The clusters CL416, CL440, and CL441 are linked when a percolation length of $10 h_{75}^{-1} \text{ Mpc}$ ($\frac{\delta\rho}{\rho} \approx 100$) is used. The mean redshift of this supercluster is 0.482. The clusters CL426 and CL433

are also linked with this percolation length and lie at a mean redshift of 0.226. At a slightly larger percolation of $13h_{75}^{-1}$ Mpc ($\frac{\delta\rho}{\rho} \approx 50$), the clusters CL415 and CL439 are linked. The mean redshift of this system is 0.357. No additional supercluster candidates are found for $10 < \frac{\delta\rho}{\rho} < 50$. This supercluster frequency is comparable to that in the distribution of local $RC \geq 0$ Abell clusters for similar overdensities – $\sim 10 - 20\%$ of Abell clusters are linked into groups of 3 or more when $10 < \frac{\delta\rho}{\rho} < 20$ (Postman et al. 1992; Lauer & Postman 1994). The frequency of superclusters at a given overdensity is correlated with the cluster-cluster correlation length. As our spectroscopic survey is largely complete for $\Lambda_{CL} \geq 50$ clusters with $0.3 \leq z_{est} < 0.5$, the general agreement between our supercluster frequency and that in the Abell catalog suggests that the correlation length for the $\Lambda_{CL} \geq 50$ systems at $z \sim 0.4 \pm 0.1$ is similar to the local value for $RC \geq 0$ clusters. If the cluster distribution at intermediate redshifts were completely random, the probability of detecting a supercluster with at least 3 members and with $\frac{\delta\rho}{\rho} > 10$ would be less than 0.005. Clearly, this is a crude qualitative constraint on the evolution of clustering but it is consistent with the findings of Gonzalez et al. (2002), who find only modest evolution in the cluster-cluster correlation length by $z \sim 0.45$ from the Las Campanas Distant Cluster Survey.

7. CONCLUSIONS

We have completed an automated search for distant clusters in a contiguous 16 square degree patch of sky using moderately deep I -band images as our source data. The complete cluster catalog and redshifts for those clusters with spectroscopic data are provided. The key results derived in this paper are summarized below. The images from the Deeprange survey are publicly available from the NOAO science archive (<http://archive.noao.edu/nsa/>).

(i) Various approaches to estimating the space density of clusters in our deep survey yield values in the range $(1.57 - 1.83) \times 10^{-5} h_{75}^3 \text{ Mpc}^{-3}$ for systems with $\Lambda_{CL} \geq 40$. The uncertainties in these estimates range from 10% to 27%, depending on the technique used. This space density range is about a factor of 1.3 – 1.6 times larger than that for comparably rich clusters ($RC \geq 0$) in the Abell catalog. The offset between our results and those for the Abell catalog is due predominantly to differences at the low richness end of the cluster distribution. The ratio of Deeprange-to-Abell cluster space density drops to 1.2 for $\Lambda_{CL} \geq 60$ ($RC \geq 1$) and is consistent with unity for $\Lambda_{CL} \geq 100$ ($RC > 2$). The discrepancy between the Abell catalog and our current survey is substantially less than that reported for the Palomar Distant Cluster Survey (Postman et al. 1996). We believe this is mostly do to the use of better values for the local space density of clusters and a more reliable calibration of the $\Lambda_{CL} - N_A$ relation in the current work. The cluster abundances found here are also consistent with the density of X-ray selected clusters in wide area surveys (*e.g.*, Ebeling et al. 1997). Bramel et al. (2000) apply matched filter cluster detection to the Edinburgh/Durham Cluster Catalog II (EDCCII) and find a significantly higher local space density of clusters than is found in the Abell catalog: $2.4_{-1.0}^{+2.7} \times 10^{-5} h_{75}^3 \text{ Mpc}^{-3}$ for

$\Lambda_{CL} \geq 40$ systems. However, their richness calibration associates $\Lambda_{CL} \geq 40$ with Abell $RC \geq 1$, in part due to their use of the now superseded cluster space densities given in Bahcall (1979). Our revised calibration would associate such systems with poorer $RC \geq 0$ clusters. If we revise their calibration to match ours then we find good agreement between their local space density and that seen at $z > 0.2$.

(ii) The comoving space density of clusters with $\Lambda_{CL} \geq 40$ is relatively constant out to $z = 0.8$. While the data do allow a gradual decline in cluster abundance with increasing redshift, a drop in density by a factor greater than 3 over the range $0.2 < z < 0.8$ is ruled out at $>99.9\%$ confidence level. Postman et al. (1996) and Ebeling et al. (1998) have previously reported results suggesting non-evolving cluster space densities out to $z = 0.6$ and $z = 0.3$, respectively. The mean V/V_{max} value for the $\Lambda_{CL} \geq 40$ sample is 0.54, in excellent agreement with the expected value for a uniform, non-evolving distribution. Coupled with the good agreement between our results and those from local x-ray surveys (*e.g.*, Ebeling et al. 1997) and a revised estimate of the density found in the EDCCII catalog (Bramel et al. 2000), a scenario where the space density of clusters has evolved very little, if at all, over the past half a Hubble time appears to be likely. This result favors CDM models with low values of Ω_m . A thorough consistency check between these data and model predictions will be the scope of a future paper. We note, however, that such a comparison is complicated by the fact that what we are measuring here is the number density of clusters as a function of optical luminosity and redshift whereas what models most often predict is the evolution of the cluster mass function. A proper analysis, therefore, either requires an accurate estimate of the mass distribution of these clusters or a prediction of the evolution of the space density of clusters in a rest-frame optical passband. Furthermore, Voit (2000) demonstrates that the evolution of the mass function of clusters and the evolution of their ICM temperature (which correlates with x-ray luminosity) differ even for a given cosmological model. Specifically, the temperature function evolution tends to be weaker than the mass function evolution. If similar trends are carried into the optical bandpass, albeit driven by different astrophysical processes, the weak (or non-existent) variation of cluster space density with redshift observed here may not imply a similarly weak evolution in the cluster mass function. What is certain, however, is that in an $\Omega_m = 1$ universe the temperature function evolves dramatically – the normalization increases by at least 3 orders of magnitude between $z = 1$ and $z = 0$. Even with a noisy correlation between optical and x-ray luminosity, such substantial evolution is clearly ruled out by the Deeprange survey.

(iii) An empirical calibration of the matched filter cluster luminosity, Λ_{CL} , and the Abell richness parameter yields $\Lambda_{CL} = 1.24N_A$. This calibration agrees well with the relationship predicted from extensive simulations.

(iv) The false positive rate using the matched filter detection method on these data is, on average, between 20 – 30%. This assessment is based on a spectroscopic follow-up survey of ~ 40 cluster candidates in the range $0.2 < z < 0.6$ and on simulations explicitly designed to estimate the spurious detection rate. The false positive rate

is a function of effective cluster size, detection significance, and cluster richness. Cluster samples that are largely free of spurious detections can be constructed by appropriately filtering on these parameters.

(v) The Λ_{CL} function is consistent with a power law of the form $dN/d\Lambda_{CL} = (1.55 \pm 0.40) \times 10^{-6}(\Lambda_{CL}/40)^{-4.40 \pm 0.30}$, where dN is in units of $h_{75}^3 \text{Mpc}^{-3}$. Two separate methods to provide an approximate calibration of the mass of the clusters in this survey find that the average mass of a $\Lambda_{CL} \geq 40$ cluster is in the few $\times 10^{14} M_{\odot}$ range. However, the mass- Λ_{CL} relation is too noisy to provide accurate estimates of individual cluster masses.

(vi) Between 10 – 20% of the spectroscopically confirmed

clusters are linked into superclusters at high overdensities ($\frac{\delta\rho}{\rho} > 10$). This percentage is comparable with the value derived from local cluster surveys and suggests that the cluster – cluster correlation function does not evolve dramatically between $z \sim 0.5$ and the current epoch.

We thank the NOAO and U.S. Gemini TACs for their support of this survey. We thank Rick White for his assistance in enhancing the astrometric accuracy of our coordinates via cross-correlation with the FIRST survey. We thank the anonymous referee for helpful comments, which improved the clarity of the paper. We also thank Lori Lubin for valuable comments on the initial draft of this paper.

REFERENCES

- Abell, G. O., 1958, ApJS, 3, 211.
 Aragon-Salamanca, A., Baugh, C. M., Kauffmann, G. 1998, MNRAS, 297, 427.
 Bahcall, N. 1979, ApJ, 232, 689.
 Bahcall, N. A., Soneira, R. M. 1983, ApJ, 270, 20.
 Becker, R. H., White, R. L., Helfand, D. J. 1995, ApJ, 450, 559.
 Blanton, M. et al. 2001, AJ, 121, 2358.
 Borgani, S., Plionis, M., Kolokotronis, V. 1999, MNRAS, 305, 866.
 Bramel, D. A., Nichol, R. C., Pope, A. C., 2000, ApJ, 533, 601.
 Colberg, J. M., White, S. D. M., Yoshida, N., MacFarland, T. J., Jenkins, A., Frenk, C. S., Pearce, F. R., Evrard, A. E., Couchman, H. M. P., Efstathiou, G., Peacock, J. A., Thomas, P. A., The Virgo Consortium 2000, MNRAS, 319, 209.
 Colless, M. et al., 2001, MNRAS, 328, 1039.
 Collins, C. A., Guzzo, L., Böhringer, H., Schuecker, P., Chincarini, G., Cruddace, R., De Grandi, S., MacGillivray, H. T., Neumann, D. M., Schindler, S., Shaver, P., Voges, W. 2000, MNRAS, 319, 939.
 Croft, R. A. C., Dalton, G. B., Efstathiou, G., Sutherland, W. J., Maddox, S. J. 1997, MNRAS, 291, 305.
 De Propriis, R. et al. 2002, MNRAS, 329, 87.
 Donahue, M., Mack, J., Scharf, C., Lee, P., Postman, M., Rosati, P., Dickinson, M., Voit, G. M., Stocke, J. T., 2001, ApJ, 552, L93.
 Donahue, M., Scharf, C., Mack, J., Lee, P., Postman, M., Rosati, P., Dickinson, M., Voit, G. M., Stocke, J., 2002, ApJ, in press.
 Ebeling, H., Edge, A. C., Fabian, A. C., Allen, S. W., Crawford, C. S., Böhringer, H. 1997, ApJ, 479, L101.
 Ebeling, H., Edge, A. C., Böhringer, H., Allen, S. W., Crawford, C. S., Fabian, A. C., Voges, W., Huchra, J. P., 1998, MNRAS, 301, 881.
 Ebeling, H., Edge, A. C., Allen, W., Crawford, C. S., Fabian, A. C., Huchra, J. P., 2000, MNRAS, 318, 333.
 Eke, V. R., Cole, S., Frenk, C. S., Navarro, J. F. 1996, MNRAS, 281, 703.
 Frei, Z., & Gunn, J. E. 1994, AJ, 108, 1476.
 Fumiaki, N. et al. 2001, PASJ, 53, 1139.
 Gladders, M. D., & Yee, H. K. C., 2000, astro-ph/0011073
 Gonzalez, A. H., Zaritsky, D., Dalcanton, J. J., Nelson, A. 2001, ApJS, 137, 117.
 Gonzalez, A. H., Zaritsky, D., Wechsler, R. H., 2002, ApJ, 571, in press.
 Gunn, J., Hoessel, J., Oke, J. B. 1986, ApJ, 306, 30
 Henry, J. P., Gioia, I. M., Maccacaro, T., Morris, S. L., Stocke, J. T., Wolter, A. 1992, ApJ, 386, 408.
 Holden, B. P., Romer, A. K., Nichol, R. C., Ulmer, M. P. 1997, AJ, 114, 170.
 Holden, B., Adami, C., Nichol, R. C., Castander, F., Lubin, L., Romer, A. K., Mazure, A., Postman, M., Ulmer, M. P., 2000, AJ, 120, 23.
 Hradecky, V., Jones, C., Donnelly, R. H., Djorgovski, S. G., Gal, R. R., Odewahn, S. C. 2000, ApJ, 543, 521.
 Jannuzi, B. T., Dey, A., Tiede, G. P., Brown, M. J. I., NDWFS Team, 2000, BAAS, 197, 77.09.
 Jarvis, J. F., & Tyson, J. A. 1981, AJ, 86, 476.
 Kepner, J., Fan, X., Bahcall, N., Gunn, J., Lupton, R., Xu, G. 1999, ApJ, 517, 78.
 Kim, R. et al. 2001, AJ, 123, 20.
 Klypin, A., Rhee, G., 1994, ApJ, 428, 399.
 Koranyi, D. M., Kleyana, J. & Grogin, N. A. 1998, PASP, 110, 1464
 Landolt, A. U. 1983, AJ, 88, 439
 Lauer, T. R. & Postman, M. 1994, ApJ, 425, 418.
 Lin, H., Kirshner, R. P., Sheckman, S. A., Landy, S. D., Oemler, A., Tucker, D. L., Schechter, P. L., 1996, ApJ, 471, 617.
 Lubin, L. M. & Postman, M., 1996, AJ, 111, 1795.
 Lubin, L. M., Postman, M., Oke, J. B., Gunn, J. E., Hoessel, J. G., Schneider, D. P. 1998, AJ, 116, 584.
 Lubin, L., Oke, J. B., Postman, M. 2002, ApJ, submitted.
 Marshall, H. L., Avni, Y., Tananbaum, H., Zamorani, G., 1983, ApJ, 269, 35.
 Mo, H. J., Jing, Y. P., White, S. D. M. 1996, MNRAS, 282, 1096.
 Monier, E., Osmer, P., Kenefick, J., Hall, P., Smith, M., Green, R., 2001, BAAS, 199, 138.10.
 Moscardini, L., Matarrese, S., Mo, H. J., 2001, MNRAS, 327, 422.
 Nichol, R. C., Collins, C. A., Guzzo, L., Lumsden, S. L. 1992, 255, 21.
 O'Meara, J. M., Tytler, D., Kirkman, D., Suzuki, N., Prochaska, J. X., Lubin, D., Wolfe, A. M. 2001, ApJ, 552, 718.
 Olsen, L. F., Scodreggio, M., da Costa, L., et al. 1999, A&A, 345, 681. (see also pg 363).
 Peebles, P. J. E., Daly, R. A., Juszkievicz, R. 1989, ApJ, 347, 563.
 Pen, U. 1998, ApJ, 498, 60.
 Postman, M., Geller, M. J., Huchra, J. P. 1988, AJ, 95, 267.
 Postman, M., Huchra, J. P., Geller, M. J., 1992, ApJ, 384, 404.
 Postman, M., Lubin, L. M., Gunn, J. E., Oke, J. B., Hoessel, J. G., Schneider, D. P., Christensen, J., 1996, AJ, 111, 615.
 Postman, M., Lauer, T. R., Szapudi, I., Oegerle, W., 1998, ApJ, 506, 33.
 Postman, M., Lubin, L., Oke, J. B. 2001, AJ, 122, 1125.
 Romer, A. K., Nichol, R. C., Holden, B. P., Ulmer, M. P., Pildis, R. A., Merrelli, A. J., Adami, C., Burke, D. J., Collins, C. A., Metevier, A. J., Kron, R. G., Commons, K. 2000, ApJS, 126, 209.
 Rosati, P., della Ceca, R., Norman, C., Giacconi, R. 1998, ApJ, 492, L21.
 Scharf, C. A., Jones, L. R., Ebeling, H., Perlman, E., Malkan, M., Wegner, G. 1997, ApJ, 477, 79.
 Schlegel, D. J., Finkbeiner, D. P., Davis, M. 1998, ApJ, 500, 525.
 Schmidt, M. 1968, ApJ, 151, 393.
 Schuecker, P., Böhringer, H. 1998, A&A, 339, 315.
 Slingland, K., Batuski, D., Miller, C., Haase, S., Michaud, K., Hill, J. M. 1998, ApJS, 115, 1.
 Squires, G., Kaiser, N., Babul, A., Fahlman, G., Woods, D., Neumann, D. M., Böhringer, H. 1996, ApJ, 461, 572.
 Szapudi, I., Postman, M., Lauer, T. R., Oegerle, W., 2001, ApJ, 548, 114.
 Tyson, J.A. & Fischer, P. 1995, ApJ, 446, L55.
 Valdes, F. 1982, Proc. SPIE, 331, 465.
 van Dokkum, P., Franx, M., Kelson, D., Illingworth, G., Fabricant, D. in *Deep Fields*, Proceedings of the ESO/ECF/STScI Workshop held at Garching, Germany, 9-12 October 2000. Stefano Cristiani, Alvio Renzini, Robert E. Williams (eds.) Springer, 2001, p. 194.
 Vogeley, M. S., Park, C., Geller, M. J., Huchra, J. P., 1992, ApJ, 391, L5.
 Voit, G. M. 2000, ApJ, 543, 113.
 Wu J.-H. P., 2001, MNRAS, 327, 629.
 Zehavi, I. et al., 2002, ApJ, 571, 172.

TABLE 1
CLUSTER DETECTION PARAMETERS

Parameter	Value
Hubble constant	$75 \text{ km s}^{-1} \text{ Mpc}^{-1}$
Ω_m	0.2 ($\Lambda = 0$)
Core Radius	133 kpc
Cutoff Radius	1.33 Mpc
LF slope	-1.10
LF M^* ($z = 0$)	-21.90
Detection Threshold	2σ
Min. Filter Redshift	0.20
Max. Filter Redshift	1.20

TABLE 2
DEEPRANGE CLUSTER CATALOG

ID	R.A. (J2000) Dec.		z_{est}	Λ_{CL}	$N_{A,0.25}$	$N_{e,0.25}$	$N_{A,0.5}$	$N_{e,0.5}$	σ	Rad ($''$)	m_3	m_{eff}	QA
001	10 08 40.77	+54 32 49.7	0.60	43.0	10.0	7.7	22.0	25.6	2.1	14	20.8	21.3	...
002	10 06 30.68	+54 32 29.1	0.20	23.6	8.4	7.4	6.5	-0.3	3.0	61	17.8	18.4	...
003	10 17 44.67	+54 32 37.5	0.30	28.6	10.7	13.2	-7.3	-10.2	2.6	45	19.0	19.5	...
004	10 22 52.82	+54 32 29.4	0.80	65.5	19.6	14.3	27.5	19.0	2.3	30	21.0	22.1	2
005	10 10 58.60	+54 33 30.9	0.30	53.0	11.3	15.3	22.0	59.1	4.8	252	18.0	19.3	1
006	10 12 49.53	+54 35 03.8	0.30	40.3	11.5	4.3	2.0	-8.9	3.7	180	18.8	19.2	...
007	10 17 00.50	+54 30 46.2	1.10	91.5	12.2	8.4	16.3	5.4	2.1	18	22.0	23.0	1
008	10 25 29.15	+54 34 55.6	0.20	36.7	4.4	5.4	-2.3	-6.5	4.6	195	17.3	17.8	...
009	10 20 14.27	+54 29 28.7	0.40	58.5	10.5	18.5	29.1	54.1	4.2	182	19.0	20.2	1
010	10 25 20.12	+54 24 22.9	0.40	28.3	3.7	24.4	0.9	18.5	2.0	15	17.8	20.1	...
011	10 22 26.71	+54 30 37.5	0.40	57.2	13.1	13.4	18.3	14.5	4.1	125	19.5	20.0	3
012	10 24 19.47	+54 29 20.8	0.30	33.1	7.7	9.3	17.9	23.1	3.0	125	18.3	19.4	...
013	10 12 45.27	+54 27 36.4	0.50	49.8	2.6	22.8	3.3	2.2	2.9	56	18.0	20.8	...
014	10 14 59.61	+54 26 28.5	0.30	43.8	11.5	20.3	16.0	28.1	4.0	119	18.8	19.3	...
015	10 22 19.72	+54 25 28.1	0.60	64.1	7.7	29.7	21.0	37.7	3.1	117	19.3	21.3	2
016	10 09 43.90	+54 23 19.7	0.20	60.1	27.4	32.7	48.5	61.6	7.5	410	17.8	18.3	3
017	10 16 36.14	+54 27 36.8	0.60	56.7	9.1	6.7	14.4	13.6	2.8	72	19.8	21.1	1
018	10 08 10.67	+54 25 27.0	0.20	36.8	1.4	-3.3	6.5	3.6	4.6	217	17.8	18.1	...
019	10 13 19.52	+54 22 08.2	0.20	43.5	5.1	10.3	15.3	22.1	5.5	415	17.5	18.0	...
020	10 08 45.00	+54 24 23.3	0.80	58.2	9.1	7.8	13.6	17.1	2.1	18	20.5	22.1	1
021	10 16 16.54	+54 23 13.1	0.20	46.9	14.3	12.6	22.1	18.6	5.9	360	18.0	18.3	...
022	10 11 39.28	+54 22 48.0	0.30	43.5	23.8	28.2	19.3	24.8	3.9	136	18.5	19.4	...
023	10 12 19.24	+54 21 38.3	0.70	55.0	17.7	3.1	22.8	-1.7	2.3	36	21.0	21.7	1
024	10 05 12.26	+54 22 10.8	0.60	58.0	11.1	16.7	23.4	34.7	2.8	69	19.8	21.2	2
025	10 21 55.82	+54 18 40.3	0.50	45.0	14.7	10.8	23.8	7.2	2.7	59	20.0	20.7	...
026	10 06 55.05	+54 18 26.3	0.40	52.3	9.1	11.4	33.3	27.5	3.8	159	19.5	20.1	2
027	10 19 13.80	+54 14 56.1	0.40	34.8	4.4	4.5	4.5	6.1	2.5	58	20.0	20.2	...
028	10 06 33.86	+54 11 35.4	0.50	50.4	13.0	1.1	12.9	-11.6	3.0	56	19.5	20.4	2
029	10 15 19.09	+54 12 22.5	0.40	37.8	6.3	20.4	6.1	17.5	2.7	71	18.5	20.0	...
030	09 59 31.50	+54 12 59.6	0.20	78.8	21.4	22.6	39.5	44.6	9.9	260	17.8	18.2	3
031	10 21 50.01	+54 11 58.0	0.20	26.0	4.4	9.6	2.5	6.6	3.3	81	17.8	18.2	...
032	10 19 08.94	+54 10 47.9	0.60	52.8	16.0	9.7	20.0	-3.3	2.6	47	20.8	21.2	2
033	10 01 32.39	+54 10 37.2	0.60	47.3	16.0	12.7	21.0	2.7	2.3	41	20.8	21.3	...
034	10 22 46.99	+54 08 14.2	0.30	26.7	4.7	-1.8	13.9	5.8	2.4	63	18.3	19.5	...
035	10 05 04.85	+54 08 57.8	0.20	84.8	35.4	48.4	65.5	95.7	10.6	473	17.8	18.4	2
036	10 23 18.63	+54 08 31.7	0.60	47.6	16.0	10.7	20.0	5.7	2.3	30	20.8	21.2	...
037	10 02 42.10	+54 09 19.4	0.50	43.9	14.1	15.8	38.4	12.1	2.6	69	19.8	20.8	...
038	10 00 23.00	+54 05 07.6	0.50	74.2	18.0	17.8	30.9	45.2	4.4	179	19.5	20.7	2
039	10 13 47.30	+54 06 14.8	0.40	47.5	10.5	17.5	28.1	38.1	3.4	124	19.0	20.2	...
040	10 15 19.62	+54 04 10.1	0.70	56.7	9.1	6.3	9.2	6.2	2.3	30	21.5	21.8	1
041	10 17 14.48	+54 01 19.7	0.30	29.0	2.3	-2.7	6.1	2.1	2.6	91	18.0	19.2	...
042	10 11 48.43	+54 03 46.5	0.60	59.8	21.6	16.9	55.5	77.6	2.9	103	20.5	21.4	2
043	10 14 51.94	+54 04 40.1	1.10	163.7	23.8	17.4	23.3	14.1	3.8	118	22.8	23.0	1
044	10 12 51.56	+54 03 05.4	0.70	74.0	21.8	16.0	37.1	35.2	3.1	147	20.5	21.8	2
045	10 09 09.03	+54 02 31.3	0.50	76.4	17.7	17.8	47.8	54.2	4.5	186	20.0	20.8	3
046	10 11 02.43	+54 03 47.0	0.60	88.0	29.1	39.7	47.5	87.7	4.3	143	20.0	21.3	3
047	10 13 42.32	+54 00 49.1	0.70	93.6	24.5	18.6	41.2	34.1	3.9	208	20.8	21.7	3
048	10 07 26.26	+54 00 51.3	0.40	34.6	4.5	4.5	9.1	9.1	2.5	76	20.3	20.3	...
049	09 59 29.40	+54 01 54.3	0.50	35.5	7.1	9.7	27.4	36.8	2.1	27	20.5	20.9	...
050	10 05 57.82	+53 58 18.8	0.70	64.8	10.5	14.3	22.8	10.1	2.7	104	20.3	21.7	1
051	10 23 16.86	+53 59 58.0	0.30	28.3	6.3	6.3	-2.9	-2.9	2.6	36	19.3	19.3	...
052	10 18 44.67	+54 01 11.6	0.40	78.6	17.6	20.4	35.3	55.5	5.7	200	18.8	20.1	3
053	10 18 28.53	+53 58 17.0	0.80	85.3	7.3	9.1	31.0	6.3	3.0	146	19.5	22.0	1
054	10 02 24.70	+54 01 34.3	0.70	85.5	35.0	30.3	48.2	45.2	3.5	195	21.5	21.8	2
055	10 01 21.90	+53 59 12.1	0.60	102.1	22.1	36.7	52.5	99.7	5.0	202	20.0	21.3	3
056	10 11 03.64	+53 57 54.3	0.30	39.0	9.2	9.2	28.8	28.8	3.5	208	19.5	19.5	...
057	10 13 55.55	+53 58 03.4	0.20	24.8	2.4	4.7	8.5	17.6	3.1	99	17.8	18.2	...
058	10 17 25.36	+53 51 41.5	0.20	39.4	0.4	-0.7	2.5	6.1	4.9	221	17.8	18.0	...
059	10 16 35.73	+53 56 26.2	0.70	51.5	7.7	1.2	27.8	8.8	2.1	17	21.0	21.6	1
060	10 15 10.25	+53 56 08.6	0.80	98.5	34.5	28.5	61.9	36.3	3.5	104	21.3	22.2	2
061	10 01 25.95	+53 54 04.6	1.10	148.5	11.0	9.4	36.0	13.1	3.5	236	21.0	23.0	1
062	10 20 40.85	+53 56 48.3	0.40	56.1	17.1	8.4	28.3	13.5	4.1	146	19.5	20.1	2
063	10 12 36.38	+53 53 18.0	0.40	109.3	28.5	47.4	59.1	85.5	7.9	222	19.0	20.0	3
064	10 14 22.85	+53 52 18.7	1.10	109.0	9.7	9.4	-4.9	-1.3	2.5	82	23.3	23.0	1
065	10 19 17.10	+53 50 43.6	0.40	87.5	26.0	22.4	47.1	51.5	6.3	244	19.3	20.1	3
066	10 08 03.58	+53 52 25.1	0.70	58.4	17.8	12.5	21.1	-4.2	2.4	38	20.5	21.7	1
067	10 02 47.14	+53 51 43.2	0.50	76.8	28.1	40.8	36.4	49.2	4.5	181	19.8	20.8	3
068	10 09 29.29	+53 51 08.8	1.00	75.7	20.1	13.4	12.9	1.4	2.0	9	21.8	22.7	1
069	10 22 29.32	+53 51 01.3	0.30	34.9	9.7	19.2	17.9	54.8	3.2	82	18.3	19.5	...
070	10 06 33.81	+53 49 06.1	0.60	42.2	24.7	18.7	24.7	10.6	2.1	18	21.0	21.3	...
071	10 21 14.67	+53 50 21.5	0.60	88.5	31.7	44.7	52.7	61.7	4.3	136	20.3	21.3	3
072	10 23 16.46	+53 49 46.6	0.70	49.1	17.2	14.9	11.9	-4.7	2.0	10	21.3	21.7	...
073	10 17 54.12	+53 49 06.8	0.60	56.5	19.6	11.7	16.5	6.7	2.8	49	20.5	21.2	3
074	10 10 41.14	+53 47 38.3	0.60	58.3	8.2	14.7	10.8	17.6	2.9	101	18.3	21.2	1
075	10 26 07.59	+53 48 36.3	1.10	108.1	14.1	14.1	1.1	1.1	2.5	43	23.0	23.0	1
076	10 05 53.65	+53 49 10.0	1.00	98.6	25.5	10.6	12.8	0.4	2.6	74	22.0	22.7	2
077	10 21 30.81	+53 46 18.1	1.10	118.9	8.8	7.7	14.3	4.2	2.8	114	20.5	23.0	1
078	10 11 11.61	+53 48 09.6	1.00	111.0	1.5	8.1	18.1	9.6	3.0	78	20.0	22.7	2
079	10 03 48.28	+53 47 46.6	0.50	73.1	16.1	17.8	55.4	74.2	4.3	201	20.5	20.9	3
080	10 01 01.82	+53 49 44.2	0.20	27.6	12.0	8.6	47.1	22.6	3.5	138	19.5	18.4	...

TABLE 2—Continued

ID	R.A. (J2000) Dec.		z_{est}	Λ_{CL}	$N_{A,0.25}$	$N_{e,0.25}$	$N_{A,0.5}$	$N_{e,0.5}$	σ	Rad (")	m_3	m_{eff}	QA
081	10 11 28.64	+53 45 08.9	0.70	75.0	12.6	4.1	21.2	5.2	3.1	163	19.3	21.6	1
082	10 07 42.66	+53 45 46.2	0.70	64.0	18.7	13.6	43.8	25.8	2.7	66	21.0	21.7	1
083	10 19 32.32	+53 42 32.0	1.10	106.5	14.4	5.6	9.2	-2.4	2.5	39	22.8	23.0	2
084	10 05 03.10	+53 45 43.7	0.30	52.6	14.5	15.2	31.0	48.8	4.8	229	18.8	19.4	2
085	10 02 19.30	+53 44 37.2	0.20	35.3	3.1	2.4	1.3	0.5	4.4	177	17.5	17.8	...
086	10 13 53.62	+53 42 49.5	1.10	87.3	7.9	2.0	-2.2	-6.8	2.0	9	22.3	23.0	2
087	10 26 42.43	+53 42 44.5	0.30	24.7	10.3	12.2	-4.9	-0.2	2.2	41	19.3	19.4	...
088	10 12 37.33	+53 41 28.2	0.60	58.8	12.6	4.7	17.5	-9.4	2.9	41	20.5	21.2	2
089	10 13 19.83	+53 43 25.5	0.30	49.7	6.8	3.3	6.3	10.1	4.5	171	18.5	19.2	...
090	10 17 54.76	+53 41 54.3	0.30	28.4	-3.7	-7.8	12.1	4.8	2.6	87	19.3	19.5	...
091	09 59 45.42	+53 42 56.1	0.20	30.3	9.3	15.4	23.1	42.7	3.8	182	18.0	18.4	...
092	10 17 03.85	+53 42 30.9	1.10	112.7	14.0	6.8	8.0	-3.5	2.6	48	21.0	23.0	1
093	10 09 40.37	+53 42 50.4	0.50	45.5	8.7	11.8	21.8	24.1	2.7	64	20.0	20.7	...
094	10 00 49.52	+53 40 16.6	0.70	119.2	24.5	26.0	69.2	63.2	4.9	270	20.8	21.6	2
095	10 21 03.84	+53 42 03.0	0.90	87.7	10.4	8.2	10.9	4.1	2.7	116	22.0	22.4	2
096	10 18 39.97	+53 39 46.5	1.00	83.8	17.1	7.5	16.8	1.5	2.2	21	22.3	22.7	1
097	10 08 39.45	+53 39 43.3	0.60	86.2	16.7	12.7	46.7	80.7	4.2	187	20.3	21.2	3
098	10 24 27.67	+53 41 13.6	0.50	54.6	12.1	21.8	6.4	21.1	3.2	53	19.8	20.8	3
099	10 04 46.42	+53 37 42.3	0.90	89.6	9.6	2.9	19.4	3.2	2.8	132	19.8	22.4	1
100	10 19 50.13	+53 40 05.3	0.20	33.6	11.3	8.6	17.1	9.6	4.2	145	18.0	18.3	...
101	10 20 47.83	+53 39 27.5	0.60	73.8	17.7	17.7	47.7	55.7	3.6	103	20.3	21.2	2
102	10 10 07.91	+53 39 40.3	0.70	80.9	14.6	21.1	13.5	46.6	3.3	146	20.0	21.8	3
103	10 24 00.76	+53 37 14.2	1.00	88.0	4.9	3.5	4.6	0.2	2.4	55	19.5	22.7	1
104	10 07 03.47	+53 42 12.9	0.20	41.8	10.4	5.7	17.5	21.6	5.2	239	17.8	18.3	...
105	10 07 11.28	+53 39 04.4	0.90	76.9	14.5	14.5	10.6	10.6	2.4	48	22.5	22.5	1
106	10 25 19.47	+53 40 57.3	0.50	62.3	28.1	27.8	35.4	34.2	3.7	122	20.5	20.8	3
107	10 13 27.45	+53 38 52.0	0.70	52.0	5.6	4.0	16.5	6.5	2.2	24	19.5	21.7	1
108	10 15 57.58	+53 38 27.2	0.50	66.9	26.7	23.8	31.8	61.2	3.9	105	20.0	20.8	3
109	10 22 37.30	+53 37 37.8	0.70	56.1	12.5	12.5	2.3	2.3	2.3	21	21.8	21.8	1
110	10 06 41.06	+53 37 23.4	0.80	73.2	18.6	-2.9	27.4	0.3	2.6	73	20.3	22.0	2
111	10 12 16.72	+53 34 53.7	0.40	46.6	9.5	14.4	15.1	20.5	3.4	62	19.0	20.1	...
112	10 11 16.86	+53 34 35.1	0.30	79.2	19.7	32.3	30.9	52.1	7.2	272	18.3	19.3	3
113	10 25 24.83	+53 37 16.5	0.30	31.4	4.5	5.3	6.0	15.1	2.8	75	18.8	19.3	...
114	10 03 30.51	+53 35 51.1	0.30	32.5	9.7	4.2	45.8	28.8	2.9	126	20.0	19.6	...
115	10 00 58.58	+53 33 22.3	0.30	52.0	12.3	17.3	22.0	41.1	4.7	232	18.0	19.3	2
116	10 17 19.32	+53 36 18.0	0.90	70.6	12.2	1.0	26.8	-2.0	2.2	28	20.8	22.4	2
117	10 16 51.63	+53 35 06.7	0.70	54.7	8.1	4.3	-3.8	-8.8	2.3	22	21.5	21.8	1
118	10 13 52.57	+53 34 03.6	0.30	45.3	13.7	12.3	20.9	22.1	4.1	138	18.3	19.2	...
119	10 08 47.97	+53 31 14.6	0.60	54.8	23.6	28.7	31.5	40.7	2.7	88	20.5	21.4	3
120	10 12 44.23	+53 33 46.7	1.10	97.2	18.8	11.2	32.6	19.5	2.3	32	22.5	23.0	1
121	10 18 54.38	+53 33 49.3	1.10	88.6	21.0	12.8	-5.5	-1.1	2.1	9	22.0	23.0	1
122	09 59 43.60	+53 31 02.9	0.40	38.9	16.5	13.5	16.1	0.1	2.8	97	19.8	20.2	...
123	10 24 49.87	+53 33 24.0	1.10	95.0	13.1	11.2	15.3	10.3	2.2	32	22.5	23.0	1
124	10 22 17.69	+53 33 45.1	0.20	32.2	3.1	3.3	0.3	5.1	4.0	100	17.5	18.0	...
125	10 21 41.58	+53 32 52.1	0.50	43.5	15.7	5.8	23.9	12.1	2.6	66	20.3	20.8	...
126	10 09 53.19	+53 30 15.2	0.40	41.4	10.5	10.5	47.1	47.1	3.0	155	20.3	20.3	...
127	10 22 19.31	+53 30 34.7	1.10	93.1	12.2	7.3	13.0	-1.1	2.2	21	22.0	23.0	1
128	10 07 09.33	+53 27 46.0	0.70	60.9	20.7	21.2	12.8	-7.4	2.5	53	21.0	21.7	3
129	10 04 21.34	+53 26 44.7	0.30	33.4	10.5	3.2	17.0	-4.2	3.0	70	18.8	19.4	...
130	10 01 40.41	+53 28 08.5	0.70	74.3	15.8	3.8	47.1	18.6	3.1	115	20.5	21.7	3
131	10 02 27.46	+53 27 33.3	0.40	49.1	12.1	20.5	28.3	39.1	3.5	99	19.5	20.1	...
132	10 20 37.76	+53 25 01.9	0.60	54.1	11.6	13.7	15.5	35.7	2.7	70	19.5	21.3	2
133	10 14 40.38	+53 28 51.8	1.00	110.0	25.3	15.4	41.0	18.1	3.0	122	21.8	22.7	1
134	10 10 52.57	+53 26 25.3	0.80	60.4	8.7	6.7	21.3	9.9	2.2	38	22.0	22.1	2
135	10 23 17.15	+53 27 01.4	0.30	22.6	4.7	9.2	-1.1	6.8	2.0	20	18.3	19.6	...
136	10 11 18.32	+53 25 51.9	1.10	104.1	9.8	4.8	4.3	0.7	2.4	55	20.5	22.9	1
137	10 16 21.24	+53 26 04.4	1.10	137.3	20.2	13.8	31.6	18.8	3.2	88	22.8	23.0	1
138	10 14 38.68	+53 25 18.0	0.30	32.0	24.4	18.2	37.5	32.8	2.9	119	19.8	19.4	...
139	10 24 28.88	+53 26 03.2	0.40	39.7	15.1	23.5	5.3	14.1	2.9	55	19.5	20.3	...
140	10 12 18.60	+53 23 23.3	0.60	45.0	15.0	14.7	9.9	16.6	2.2	25	20.8	21.3	...
141	10 20 00.98	+53 24 33.5	1.10	107.9	14.6	10.9	19.2	3.3	2.5	101	22.3	23.0	2
142	10 18 08.93	+53 22 24.1	0.50	66.6	24.0	19.8	35.9	34.2	3.9	78	19.5	20.8	3
143	10 01 41.82	+53 21 50.7	0.90	81.4	22.2	22.2	20.5	20.5	2.5	76	22.5	22.5	1
144	10 24 39.32	+53 23 18.5	1.00	101.8	30.3	23.4	22.1	12.8	2.7	65	22.5	22.7	2
145	10 08 46.06	+53 21 42.4	0.30	40.8	16.5	25.2	13.0	8.8	3.7	85	18.8	19.4	...
146	10 14 05.73	+53 21 42.2	0.70	90.8	24.8	23.9	52.1	62.3	3.8	194	20.5	21.8	3
147	10 13 32.73	+53 21 49.9	0.30	35.1	4.2	4.2	5.8	5.8	3.2	106	19.5	19.4	...
148	10 05 27.85	+53 20 48.8	1.10	99.4	4.8	9.4	-14.6	-7.3	2.3	23	23.3	23.0	1
149	10 25 14.86	+53 20 42.0	0.20	23.5	2.5	-0.7	-0.1	3.1	3.0	74	17.0	17.9	...
150	10 19 23.50	+53 19 18.3	0.40	32.4	5.5	8.5	8.1	19.1	2.3	30	19.0	20.2	...
151	10 16 22.32	+53 19 35.8	0.60	78.5	21.6	29.7	36.5	64.7	3.8	157	20.5	21.3	2
152	10 20 55.58	+53 19 23.2	0.20	18.9	3.5	8.4	0.9	5.7	2.4	44	18.8	18.4	...
153	10 16 41.90	+53 18 12.8	0.30	35.8	13.2	13.2	29.8	29.8	3.2	139	19.5	19.5	...
154	10 00 23.77	+53 19 57.9	1.00	101.3	16.4	7.8	18.5	9.4	2.7	85	21.5	22.7	2
155	10 25 35.84	+53 17 43.7	1.10	93.6	3.8	-0.3	-9.6	-9.5	2.2	16	22.8	23.0	1
156	10 09 25.71	+53 13 50.6	0.20	19.1	-2.3	-2.3	-13.4	-13.4	2.4	59	18.3	18.2	...
157	10 07 15.55	+53 16 48.3	0.30	61.9	15.8	15.3	27.3	36.1	5.6	177	18.5	19.3	3
158	10 00 11.86	+53 17 23.2	0.20	74.2	13.0	22.3	18.9	42.1	9.3	297	16.5	18.1	3
159	10 22 12.68	+53 16 33.3	1.10	114.1	8.5	14.2	-3.7	-1.3	2.7	88	23.3	23.0	1
160	10 01 55.15	+53 16 03.0	0.70	60.3	2.6	1.3	3.5	4.0	2.5	64	18.5	21.7	1

TABLE 2—Continued

ID	R.A. (J2000) Dec.		z_{est}	Λ_{CL}	$N_{A,0.25}$	$N_{e,0.25}$	$N_{A,0.5}$	$N_{e,0.5}$	σ	Rad (")	m_3	m_{eff}	QA
161	10 04 25.16	+53 16 20.5	1.10	87.8	5.0	1.7	11.0	3.1	2.0	13	20.3	23.0	1
162	10 22 55.39	+53 15 43.1	0.20	20.0	5.5	4.7	-1.1	1.6	2.5	51	18.8	18.2	...
163	10 23 39.91	+53 15 31.5	0.90	68.1	19.8	13.0	33.3	11.6	2.1	16	21.0	22.5	1
164	10 01 29.98	+53 14 34.0	0.60	44.8	13.0	17.7	10.9	16.6	2.2	37	20.8	21.3	...
165	10 05 51.25	+53 15 07.4	0.40	53.8	16.1	20.5	48.3	45.1	3.9	192	19.5	20.1	2
166	10 26 49.86	+53 13 45.0	0.50	61.7	17.1	17.8	36.4	46.2	3.6	75	20.5	20.8	3
167	10 18 16.85	+53 14 12.6	0.20	28.8	7.7	7.7	20.6	20.6	3.6	187	18.3	18.2	...
168	10 10 46.46	+53 13 18.1	0.60	55.6	17.6	20.7	18.5	24.6	2.7	37	20.5	21.3	3
169	10 20 04.18	+53 13 58.6	0.70	93.8	22.5	9.4	46.2	31.3	3.9	125	20.8	21.7	3
170	10 17 36.16	+53 11 08.0	0.30	48.7	10.5	11.3	18.0	26.1	4.4	146	18.8	19.4	...
171	10 15 23.80	+53 12 18.9	0.20	67.7	12.3	13.4	24.3	24.5	8.5	344	16.8	17.8	3
172	10 01 53.51	+53 10 29.9	0.30	32.5	4.2	4.2	-6.2	-6.2	2.9	53	19.5	19.4	...
173	10 22 06.89	+53 09 43.5	1.10	129.1	21.1	8.9	7.3	4.6	3.0	72	22.5	22.9	1
174	10 13 39.39	+53 11 23.3	0.50	62.1	16.7	16.8	47.8	40.2	3.7	140	20.0	20.8	3
175	10 20 42.06	+53 11 00.8	0.80	106.3	26.6	19.0	69.5	53.5	3.8	171	21.0	22.1	1
176	10 15 31.64	+53 08 32.5	0.50	53.9	15.1	8.1	20.4	-2.6	3.2	90	19.8	20.5	1
177	10 14 12.57	+53 10 00.7	0.70	86.6	37.2	27.6	45.9	28.5	3.6	170	21.3	21.8	3
178	10 17 07.23	+53 09 23.9	0.70	74.0	19.5	20.4	28.2	25.8	3.1	123	20.8	21.7	2
179	10 08 13.81	+53 09 00.5	0.80	59.9	20.5	16.8	39.9	34.3	2.1	15	21.3	22.1	2
180	10 17 55.03	+53 06 51.2	0.80	97.1	26.1	11.2	43.5	12.1	3.5	158	20.5	22.0	1
181	10 04 21.61	+53 07 39.9	1.10	96.5	7.8	4.1	16.3	-4.3	2.2	25	20.5	23.0	1
182	10 05 58.06	+53 06 06.6	0.30	46.7	12.5	18.2	24.0	27.8	4.2	226	18.8	19.4	...
183	10 26 44.43	+53 06 50.2	0.20	47.4	4.5	-0.6	8.9	-0.5	5.9	160	17.0	17.8	...
184	10 07 15.72	+53 07 00.4	0.70	64.6	19.8	6.1	8.1	-17.8	2.7	45	20.5	21.6	2
185	10 25 41.20	+53 07 40.7	1.00	100.5	23.2	13.4	21.2	11.8	2.7	54	21.8	22.7	1
186	10 06 55.26	+53 04 58.2	1.10	91.4	4.5	4.5	-1.3	-1.3	2.1	13	23.0	23.0	1
187	10 22 57.00	+53 05 10.7	0.70	61.3	21.2	14.0	32.9	18.8	2.5	31	21.3	21.7	2
188	10 24 16.00	+53 03 57.8	0.30	51.9	17.5	21.2	45.0	60.8	4.7	127	18.8	19.5	3
189	10 03 59.80	+53 04 13.6	0.40	69.2	26.5	38.5	35.1	48.1	5.0	230	19.0	20.2	2
190	10 21 43.33	+53 02 05.8	0.70	64.9	11.7	11.7	26.8	16.3	2.7	57	21.0	21.8	3
191	10 25 29.61	+53 01 06.3	1.10	115.4	14.4	8.4	5.4	2.1	2.7	142	22.0	23.0	3
192	10 07 33.70	+53 01 08.5	0.40	42.0	13.1	14.5	13.3	4.1	3.0	63	19.5	20.2	...
193	10 17 09.04	+53 00 12.8	0.30	37.9	14.7	11.3	9.7	8.1	3.4	92	19.0	19.3	...
194	10 11 48.68	+53 00 40.5	0.30	25.0	7.2	5.3	26.8	20.1	2.3	32	19.5	19.4	...
195	10 11 18.56	+52 59 15.2	0.60	73.4	31.6	26.7	40.5	20.6	3.6	89	20.5	21.3	3
196	10 00 23.12	+53 00 40.0	0.40	48.7	14.5	18.5	14.1	42.1	3.5	91	19.0	20.2	...
197	10 11 01.97	+53 00 55.3	0.40	32.7	6.1	3.4	4.3	4.5	2.4	46	19.5	20.1	...
198	10 06 26.07	+52 57 34.6	0.40	37.5	2.1	6.4	-2.7	1.5	2.7	36	19.5	20.0	...
199	10 04 56.81	+52 56 53.4	0.80	75.9	20.6	10.6	29.5	24.6	2.7	80	21.0	22.1	1
200	10 01 02.92	+52 57 57.6	0.30	29.1	12.5	8.2	0.0	-3.2	2.6	72	18.8	19.5	...
201	10 16 02.13	+52 54 58.9	0.30	47.2	6.5	12.3	13.0	2.1	4.3	128	17.8	19.2	...
202	10 12 07.53	+52 54 46.1	0.50	37.4	7.7	4.8	5.8	22.1	2.2	17	20.0	20.8	...
203	10 22 09.42	+52 55 28.1	0.60	43.0	11.0	11.7	9.9	31.6	2.1	12	20.8	21.3	...
204	10 19 31.23	+52 54 51.3	0.20	17.5	6.5	6.4	5.9	9.7	2.2	42	18.8	18.5	...
205	10 07 38.86	+52 53 41.3	0.40	33.5	9.6	1.4	18.3	10.5	2.4	59	18.8	20.1	...
206	10 24 26.62	+52 52 56.5	0.90	88.2	22.2	14.8	33.8	32.5	2.7	90	20.8	22.5	2
207	10 04 11.02	+52 52 35.3	0.40	55.4	15.1	19.5	24.3	40.1	4.0	203	19.5	20.2	2
208	10 19 13.10	+52 52 23.2	0.40	36.7	16.5	16.5	42.1	42.1	2.6	57	20.3	20.3	...
209	10 05 54.12	+52 52 08.0	1.10	116.7	12.0	6.8	24.0	7.8	2.7	59	21.0	23.0	1
210	10 10 53.14	+52 52 14.6	0.70	52.1	14.6	4.9	24.2	2.0	2.2	14	20.8	21.7	1
211	10 26 35.03	+52 51 27.3	0.20	17.8	2.4	0.3	1.5	4.1	2.2	26	17.8	18.1	...
212	10 25 45.91	+52 50 05.7	0.50	116.4	33.1	23.1	49.4	34.4	6.8	117	19.8	20.5	3
213	10 00 46.48	+52 45 32.6	0.30	35.4	7.5	4.3	36.0	32.1	3.2	95	18.8	19.3	...
214	10 01 48.89	+52 46 07.9	1.10	94.2	18.8	11.3	0.6	-7.4	2.2	18	21.8	23.0	1
215	10 05 26.84	+52 43 48.5	0.30	38.1	6.7	3.3	11.9	13.1	3.5	133	18.3	19.2	...
216	10 20 57.53	+52 46 00.6	0.20	26.5	10.4	10.4	4.7	4.7	3.3	156	18.5	18.4	...
217	10 13 14.06	+52 43 59.0	0.30	31.6	3.3	3.3	1.1	1.1	2.9	109	19.3	19.2	...
218	10 06 27.56	+52 45 04.0	0.50	45.7	10.1	10.8	3.4	19.1	2.7	50	19.8	20.7	...
219	10 01 55.75	+52 40 17.6	0.70	62.1	12.8	4.6	27.1	7.2	2.6	87	20.5	21.7	2
220	10 01 07.68	+52 41 52.4	0.80	76.4	6.5	0.3	32.9	10.0	2.7	80	21.3	22.0	2
221	10 02 43.82	+52 42 46.9	0.40	40.1	13.5	13.5	12.1	12.1	2.9	86	20.3	20.3	...
222	10 22 31.58	+52 42 02.5	0.20	21.6	1.4	1.3	-3.3	-4.9	2.7	40	17.3	18.0	...
223	10 17 45.32	+52 41 14.5	0.40	44.8	12.3	21.5	14.1	29.1	3.2	118	18.5	20.2	...
224	10 10 48.77	+52 42 14.2	0.40	38.9	1.5	-4.6	14.1	3.5	2.8	81	19.0	20.0	...
225	10 05 45.42	+52 40 15.0	0.80	73.1	17.2	13.7	35.0	29.2	2.6	74	21.8	22.2	2
226	10 17 09.60	+52 41 40.6	0.30	33.7	21.4	21.2	32.5	36.8	3.0	134	19.8	19.4	...
227	10 10 03.97	+52 38 40.0	0.20	22.1	6.4	6.4	-4.3	-4.3	2.8	68	18.5	18.5	...
228	10 24 42.24	+52 41 13.8	1.10	108.5	15.5	9.1	9.2	2.3	2.5	42	22.8	23.0	1
229	10 12 31.22	+52 41 08.5	0.40	39.7	26.5	26.5	16.1	16.1	2.9	80	20.3	20.3	...
230	10 23 17.36	+52 40 22.5	0.60	54.6	20.6	19.7	21.5	15.6	2.7	36	20.5	21.3	3
231	10 15 55.35	+52 39 41.7	0.60	51.3	15.0	7.7	-3.0	-14.4	2.5	24	20.8	21.2	2
232	10 21 29.55	+52 39 18.7	0.50	55.8	23.7	34.8	41.9	47.2	3.3	119	20.3	20.8	2
233	10 19 42.88	+52 40 37.3	1.10	96.8	13.2	7.9	8.0	4.6	2.3	46	22.8	22.9	1
234	10 23 51.19	+52 39 28.4	1.20	138.8	11.4	11.4	4.2	4.2	3.0	88	23.3	23.1	1
235	10 02 47.91	+52 37 10.6	0.70	59.3	22.5	8.5	9.2	-28.2	2.5	36	20.8	21.6	1
236	10 06 32.95	+52 40 50.9	0.30	48.9	9.7	4.7	18.9	14.7	4.4	145	18.3	19.1	...
237	10 01 58.84	+52 36 40.4	0.60	43.7	13.9	18.7	-13.4	11.6	2.1	26	21.5	21.3	...
238	10 20 48.71	+52 39 36.6	0.40	44.2	9.5	11.5	17.1	19.1	3.2	122	19.0	20.1	...
239	10 03 39.62	+52 40 25.9	0.30	37.4	2.5	-1.3	2.0	-1.3	3.4	103	18.8	19.1	...
240	10 10 31.71	+52 35 10.3	0.90	71.8	13.8	7.8	12.9	7.2	2.2	17	22.3	22.5	3

TABLE 2—Continued

ID	R.A. (J2000) Dec.		z_{est}	Λ_{CL}	$N_{A,0.25}$	$N_{e,0.25}$	$N_{A,0.5}$	$N_{e,0.5}$	σ	Rad ($''$)	m_3	m_{eff}	QA
241	10 19 20.32	+52 35 50.9	0.30	47.1	12.7	13.2	37.7	40.8	4.3	226	19.0	19.4	...
242	10 07 21.76	+52 30 48.9	0.20	32.1	4.3	0.6	0.1	-2.4	4.0	184	18.0	18.2	...
243	10 15 11.84	+52 34 12.2	1.10	86.7	17.0	6.7	5.8	-1.0	2.0	11	21.5	23.0	1
244	10 08 52.65	+52 35 47.5	0.40	34.2	-0.5	-0.5	36.1	36.1	2.5	56	20.3	20.3	...
245	10 11 59.52	+52 32 54.5	0.60	52.3	14.7	15.7	31.7	28.6	2.6	51	21.0	21.3	2
246	10 15 42.32	+52 32 45.8	0.50	42.4	14.7	14.8	21.8	14.1	2.5	43	20.0	20.8	...
247	10 17 01.58	+52 33 12.2	0.50	68.0	19.7	15.8	40.8	23.1	4.0	117	20.0	20.7	3
248	10 02 56.87	+52 31 25.6	0.40	38.5	15.1	18.4	7.3	-2.5	2.8	73	19.5	20.1	...
249	10 09 18.47	+52 32 04.5	1.10	130.0	2.7	1.9	6.9	2.6	3.0	156	20.0	23.0	1
250	10 04 09.59	+52 30 20.8	0.20	30.3	9.4	8.6	-0.5	-1.4	3.8	173	17.8	18.4	...
251	10 12 00.59	+52 29 41.9	0.90	73.5	15.2	6.7	18.8	-4.4	2.3	35	20.8	22.4	2
252	10 16 00.79	+52 29 59.0	1.10	130.8	20.9	16.5	28.9	17.8	3.0	121	21.8	23.0	1
253	10 06 14.12	+52 32 21.6	0.70	71.4	21.7	6.9	30.8	10.6	3.0	82	21.0	21.7	1
254	10 13 21.70	+52 28 15.5	0.30	26.8	4.4	5.3	-1.5	0.1	2.4	44	19.8	19.3	...
255	10 18 24.25	+52 29 27.5	0.30	44.1	23.5	23.2	25.0	24.8	4.0	157	18.8	19.4	...
256	10 10 03.44	+52 26 44.6	0.40	43.2	12.0	16.5	24.1	39.1	3.1	70	19.3	20.3	...
257	10 04 34.76	+52 27 13.4	1.10	101.9	3.3	3.3	13.1	13.1	2.4	44	23.0	23.0	2
258	10 20 40.95	+52 27 51.9	0.30	50.8	14.7	25.3	24.9	40.1	4.6	189	18.3	19.3	2
259	10 03 43.62	+52 28 43.3	0.80	73.3	17.2	15.7	-0.9	0.4	2.6	77	21.8	22.1	3
260	10 16 22.51	+52 26 24.4	0.60	49.3	5.6	11.7	18.5	19.6	2.4	42	20.5	21.2	...
261	10 09 43.65	+52 26 28.9	0.80	104.3	23.5	12.0	69.9	33.3	3.7	168	21.3	22.0	1
262	10 03 51.02	+52 24 35.5	0.60	48.5	14.0	9.7	24.0	24.6	2.4	52	20.8	21.3	...
263	10 00 48.44	+52 23 53.8	0.40	57.3	15.1	20.5	37.3	57.1	4.1	282	19.5	20.2	2
264	10 06 19.19	+52 26 39.0	1.10	140.1	19.0	9.7	36.8	17.0	3.3	184	21.5	22.9	1
265	10 21 32.27	+52 25 03.0	1.00	79.5	4.5	4.6	1.1	2.6	2.1	16	20.0	22.7	2
266	10 00 24.57	+52 25 17.2	0.80	90.9	14.6	10.9	24.2	21.7	3.2	161	20.0	22.1	2
267	10 23 34.97	+52 23 34.3	0.50	63.8	10.1	16.1	23.5	17.4	3.8	116	18.8	20.5	1
268	10 17 52.98	+52 23 03.7	0.50	72.0	16.0	18.8	41.9	43.2	4.2	143	19.5	20.6	3
269	10 09 03.56	+52 23 40.4	0.50	83.5	25.7	18.8	69.8	66.2	4.9	129	20.0	20.8	3
270	10 07 20.21	+52 22 24.0	0.30	33.6	8.8	8.2	11.3	7.8	3.0	78	18.5	19.4	...
271	10 23 58.40	+52 27 24.5	0.20	39.7	16.4	18.6	16.7	18.6	5.0	300	17.3	18.3	...
272	10 22 25.24	+52 25 05.6	0.20	35.6	3.4	5.7	14.5	12.6	4.5	204	17.8	18.2	...
273	10 06 00.09	+52 20 52.0	0.80	97.3	23.7	17.3	56.7	39.4	3.5	124	21.5	22.1	1
274	10 23 03.42	+52 21 25.9	1.10	92.7	14.6	9.2	10.1	-0.1	2.2	19	21.8	23.0	1
275	10 22 07.90	+52 21 32.2	0.60	52.4	19.7	19.7	17.6	17.6	2.6	72	21.3	21.3	1
276	10 16 22.66	+52 19 42.6	0.30	32.4	11.5	12.2	4.0	9.8	2.9	41	18.8	19.4	...
277	10 24 21.16	+52 19 41.0	0.50	45.0	10.7	7.8	25.8	43.2	2.6	89	20.0	20.9	...
278	10 13 31.77	+52 18 58.4	0.70	52.8	16.7	5.0	19.8	-17.8	2.2	20	21.0	21.7	2
279	10 12 30.14	+52 15 51.6	0.20	43.8	1.5	5.4	3.9	5.5	5.5	281	17.0	17.8	...
280	10 15 08.17	+52 18 57.5	0.80	66.8	19.7	13.3	17.7	11.4	2.4	70	21.5	22.1	3
281	10 16 01.51	+52 18 40.0	0.60	73.1	23.7	18.7	35.7	22.6	3.6	87	20.3	21.2	3
282	10 21 52.93	+52 17 35.5	0.50	41.6	3.7	8.8	12.8	28.1	2.5	127	20.0	20.7	...
283	10 00 57.81	+52 14 47.6	0.40	47.1	10.1	14.4	13.3	29.5	3.4	124	19.5	20.1	...
284	10 19 54.83	+52 15 25.9	0.60	85.6	26.6	30.7	34.5	59.7	4.2	107	20.5	21.2	3
285	10 25 48.46	+52 17 56.5	0.20	27.8	-0.3	-0.3	-5.4	-5.4	3.5	136	18.3	18.2	...
286	10 23 47.58	+52 17 32.4	1.10	112.6	9.7	3.0	15.9	1.0	2.6	85	20.0	23.0	1
287	10 24 06.15	+52 14 43.1	0.80	100.7	19.3	15.7	29.9	26.0	3.6	115	21.8	22.1	3
288	10 05 41.11	+52 18 07.1	0.20	37.2	7.4	7.7	3.5	-2.4	4.7	151	17.8	18.2	...
289	10 21 23.99	+52 13 12.6	0.40	44.9	7.6	2.4	9.3	24.5	3.2	157	18.8	20.0	...
290	10 22 20.51	+52 14 41.7	0.80	72.5	20.1	12.0	32.5	7.9	2.6	81	20.5	22.1	2
291	10 06 28.67	+52 11 21.1	0.70	52.9	2.0	0.3	7.2	1.2	2.2	37	21.5	21.7	1
292	10 13 58.27	+52 12 59.3	0.30	35.3	8.7	7.3	18.7	17.1	3.2	94	19.0	19.4	...
293	10 23 42.19	+52 09 46.0	1.10	109.8	12.0	9.1	-0.2	3.5	2.6	81	22.8	22.9	3
294	10 03 14.26	+52 10 39.1	0.30	45.5	8.3	6.7	15.1	14.7	4.1	186	18.0	19.1	...
295	10 20 18.03	+52 11 05.8	0.30	33.8	4.5	1.3	2.0	4.1	3.0	98	18.8	19.2	...
296	10 11 53.53	+52 09 38.5	0.40	43.1	17.1	20.5	33.3	44.1	3.1	117	19.5	20.3	...
297	10 18 53.24	+52 12 09.2	0.40	48.7	8.5	3.4	6.1	20.5	3.5	120	19.0	20.1	...
298	10 02 15.92	+52 10 54.2	0.20	33.0	13.4	17.6	23.5	27.6	4.1	278	17.8	18.3	...
299	10 13 54.32	+52 08 49.8	1.10	97.3	16.4	16.4	10.7	10.7	2.3	47	23.0	23.0	1
300	10 19 38.96	+52 07 35.2	0.20	27.0	-0.6	0.3	-0.3	-5.9	3.4	146	17.3	18.0	...
301	10 15 27.60	+52 06 07.2	0.70	87.0	23.2	10.1	51.9	25.6	3.6	124	21.3	21.7	3
302	10 22 27.79	+52 08 16.3	0.90	79.1	-0.1	2.9	-1.6	2.8	2.4	52	19.0	22.4	1
303	10 20 43.45	+52 07 42.2	0.70	50.3	2.5	2.1	1.1	7.8	2.1	18	18.8	21.8	1
304	10 11 24.65	+52 05 32.6	0.80	82.3	26.5	18.8	31.9	8.1	2.9	95	21.3	22.1	1
305	10 18 07.01	+52 05 05.8	1.10	122.3	4.1	1.1	13.3	-0.9	2.9	157	19.8	22.9	1
306	10 00 53.84	+52 03 55.1	0.30	27.7	1.5	4.2	14.0	2.8	2.5	45	18.8	19.4	...
307	10 08 45.27	+52 04 12.8	0.60	50.2	7.6	15.7	16.5	29.6	2.5	42	20.5	21.3	1
308	10 01 04.95	+52 02 53.0	0.40	39.2	12.5	4.5	28.1	19.1	2.8	68	19.8	20.3	...
309	10 23 00.04	+52 01 00.8	0.20	79.5	12.3	13.3	27.3	38.1	10.0	516	16.8	18.0	3
310	10 25 37.51	+52 02 52.5	0.30	51.6	10.7	16.3	19.9	17.1	4.7	131	18.3	19.2	2
311	10 07 09.36	+52 01 50.8	0.60	59.6	22.6	16.7	13.5	19.6	2.9	38	20.5	21.3	3
312	10 04 25.98	+52 02 40.8	1.00	115.4	19.1	8.2	38.9	11.8	3.1	150	21.8	22.7	1
313	10 04 50.39	+52 02 24.0	0.70	87.1	27.7	19.3	58.8	35.3	3.6	143	21.0	21.7	3
314	10 02 17.58	+51 59 51.6	0.20	40.9	8.5	15.3	7.9	17.1	5.1	299	17.0	18.0	...
315	10 18 45.99	+52 01 02.7	1.10	99.2	15.9	6.7	26.8	-5.1	2.3	33	21.5	22.9	1
316	10 10 08.70	+51 57 59.4	0.30	47.7	16.7	23.2	38.7	51.8	4.3	193	19.0	19.5	...
317	10 04 23.63	+51 58 09.8	0.20	31.0	8.4	7.4	6.5	8.7	3.9	162	17.8	18.5	...
318	10 17 16.93	+51 57 26.0	1.00	104.0	20.4	13.9	23.5	5.4	2.8	102	21.5	22.7	1
319	10 12 13.61	+51 58 12.6	0.30	35.2	2.7	2.7	10.7	10.7	3.2	116	19.0	19.1	...
320	10 04 03.83	+51 56 19.7	0.90	90.4	24.6	18.6	26.9	20.2	2.8	109	22.3	22.5	1

TABLE 2—Continued

ID	R.A. (J2000) Dec.		z_{est}	Λ_{CL}	$N_{A,0.25}$	$N_{e,0.25}$	$N_{A,0.5}$	$N_{e,0.5}$	σ	Rad (")	m_3	m_{eff}	QA
321	10 18 15.08	+51 54 56.7	0.90	119.9	15.2	15.1	24.6	22.5	3.7	157	20.0	22.4	1
322	10 08 19.92	+51 55 46.5	0.70	50.3	7.1	3.3	-22.8	-23.8	2.1	10	21.5	21.7	3
323	10 14 08.01	+51 55 39.9	1.20	116.7	9.7	6.4	11.1	3.5	2.5	41	21.8	23.1	1
324	10 17 35.83	+51 53 45.1	0.50	63.2	21.7	23.8	37.9	45.2	3.7	209	20.3	20.8	1
325	10 26 43.57	+51 54 25.2	0.20	69.6	20.1	16.3	21.3	15.1	8.7	335	17.5	18.0	3
326	10 04 56.68	+51 53 12.8	0.80	105.4	21.3	11.7	53.5	40.5	3.8	148	21.8	22.1	3
327	10 11 43.82	+51 52 51.6	0.80	59.0	16.7	12.3	4.7	-0.6	2.1	11	21.5	22.1	1
328	10 19 38.17	+51 52 50.0	0.60	53.7	18.0	24.7	27.0	47.7	2.6	39	20.8	21.4	2
329	10 09 03.44	+51 51 22.9	0.40	36.4	4.1	11.5	17.3	28.1	2.6	85	19.5	20.2	...
330	10 17 10.47	+51 50 46.0	1.10	99.2	11.3	5.3	15.9	3.3	2.3	36	22.3	23.0	1
331	10 15 47.48	+51 50 47.2	1.10	103.0	8.5	4.4	-2.6	-8.3	2.4	22	22.8	22.9	1
332	10 14 42.43	+51 53 00.5	0.30	39.9	10.5	12.2	6.0	15.8	3.6	188	18.8	19.4	...
333	10 11 45.79	+51 48 08.7	0.20	41.2	7.3	2.7	19.1	10.6	5.2	261	18.0	18.2	...
334	10 09 46.10	+51 47 02.1	0.70	68.8	13.1	11.3	27.2	25.2	2.8	137	21.5	21.7	1
335	10 13 59.39	+51 47 33.4	0.40	56.7	9.1	17.5	47.3	62.1	4.1	235	19.5	20.2	1
336	10 01 13.46	+51 47 03.2	1.10	93.1	10.4	10.4	16.7	16.7	2.2	39	23.0	23.0	1
337	10 05 56.10	+51 46 47.3	0.70	50.1	7.7	4.1	22.8	7.8	2.1	14	21.0	21.7	1
338	10 16 14.93	+51 47 52.5	0.30	73.1	18.5	15.3	34.0	32.1	6.6	265	18.8	19.3	2
339	10 02 34.47	+51 47 32.5	1.10	127.3	20.0	13.5	34.9	21.9	3.0	122	22.5	23.0	1
340	10 16 00.32	+51 43 50.5	0.60	63.1	12.7	11.7	26.0	8.7	3.1	163	19.3	21.1	3
341	10 15 37.39	+51 47 01.7	0.70	62.2	18.2	12.0	21.9	-3.7	2.6	105	21.3	21.7	1
342	10 03 16.21	+51 45 22.1	0.70	78.3	18.7	21.2	54.8	50.5	3.2	148	21.0	21.8	1
343	10 19 50.03	+51 43 31.8	0.30	35.0	11.7	8.2	25.7	21.8	3.2	59	19.0	19.5	...
344	10 19 11.69	+51 41 22.9	1.00	97.0	4.8	6.0	13.0	9.7	2.6	94	20.3	22.7	1
345	10 12 03.64	+51 41 44.4	1.00	87.0	7.8	7.8	7.3	7.3	2.3	40	22.8	22.7	1
346	10 10 34.84	+51 41 36.3	0.40	41.4	13.5	8.5	30.1	31.1	3.0	105	19.8	20.2	...
347	10 03 18.75	+51 39 41.9	0.80	97.2	26.5	10.1	85.9	47.0	3.5	189	21.3	22.1	1
348	10 17 55.73	+51 38 40.9	0.40	35.8	16.4	21.5	17.5	22.1	2.6	51	20.0	20.2	...
349	10 09 48.48	+51 38 51.1	0.30	36.4	9.8	8.3	14.3	11.1	3.3	89	18.5	19.3	...
350	10 07 24.14	+51 37 45.8	0.40	58.7	16.5	16.4	25.1	21.5	4.2	143	19.8	20.1	1
351	10 05 04.03	+51 39 09.6	0.40	37.4	5.1	9.4	15.3	20.5	2.7	82	19.5	20.1	...
352	10 02 10.05	+51 36 26.4	0.80	73.1	28.6	22.4	35.9	27.7	2.6	60	22.0	22.2	1
353	10 04 49.88	+51 36 45.7	0.30	35.8	7.5	4.3	13.0	11.1	3.2	81	18.8	19.3	...
354	10 24 33.65	+51 36 25.5	0.20	56.9	3.4	2.3	28.5	21.1	7.1	412	17.8	18.0	2
355	10 26 23.61	+51 37 36.1	0.20	29.1	1.4	-5.6	6.7	1.5	3.7	200	17.3	17.8	...
356	10 25 47.48	+51 36 24.4	0.80	84.4	26.2	20.8	21.6	8.3	3.0	65	20.8	22.1	2
357	10 14 00.56	+51 36 25.0	0.20	34.9	5.3	5.3	9.1	9.1	4.4	186	18.0	18.0	...
358	10 06 22.32	+51 35 59.2	0.40	47.5	15.0	17.4	17.1	31.5	3.4	105	19.3	20.1	...
359	10 11 29.47	+51 34 54.4	0.50	40.0	12.1	8.8	1.4	0.2	2.3	23	19.8	20.7	...
360	10 03 17.59	+51 37 16.4	0.20	28.9	2.7	2.7	11.6	11.6	3.6	209	18.3	18.3	...
361	10 15 38.29	+51 34 03.8	0.50	50.8	20.7	19.8	39.9	33.2	3.0	90	20.3	20.9	1
362	10 18 44.16	+51 33 20.5	0.30	27.5	7.0	6.2	18.1	21.8	2.5	35	20.3	19.4	...
363	10 13 23.18	+51 33 44.2	0.70	54.7	14.8	6.4	19.1	-7.7	2.3	37	20.5	21.7	1
364	10 20 52.29	+51 35 20.7	0.40	48.6	11.4	11.5	54.5	56.1	3.5	133	20.0	20.3	...
365	10 14 56.61	+51 31 47.9	0.30	49.1	12.8	23.3	16.3	19.1	4.4	117	18.5	19.3	...
366	10 22 49.38	+51 32 32.2	1.10	104.9	15.4	10.1	8.4	1.1	2.5	53	22.5	23.0	1
367	10 19 06.23	+51 32 13.1	0.60	56.7	17.7	13.7	6.7	1.6	2.8	60	21.0	21.2	3
368	10 16 34.05	+51 31 40.4	0.30	29.4	5.3	2.2	17.1	10.8	2.7	57	19.3	19.4	...
369	10 00 36.02	+51 32 38.0	0.20	41.8	13.1	10.3	21.3	20.1	5.2	245	17.5	18.0	...
370	10 21 41.99	+51 33 23.5	0.30	42.8	6.8	9.3	12.3	23.1	3.9	128	18.5	19.3	...
371	10 24 03.78	+51 30 08.0	1.10	111.0	9.7	4.6	23.9	1.5	2.6	89	20.0	23.0	1
372	10 05 23.00	+51 30 43.3	0.50	44.7	24.1	19.8	10.4	3.2	2.6	37	20.5	20.8	...
373	10 09 21.66	+51 28 53.1	0.30	35.6	12.3	9.2	4.1	2.8	3.2	70	19.3	19.4	...
374	10 12 18.74	+51 31 43.6	0.30	31.5	4.0	1.2	11.1	13.8	2.8	99	20.3	19.4	...
375	10 00 51.09	+51 26 18.1	0.50	56.6	13.1	12.8	27.4	25.1	3.3	101	19.8	20.7	2
376	10 20 52.25	+51 26 16.2	0.60	51.5	17.6	4.7	21.5	-9.4	2.5	72	20.5	21.2	1
377	10 23 34.37	+51 27 15.6	0.60	96.6	36.6	34.7	74.5	61.7	4.7	216	20.5	21.2	3
378	10 25 19.45	+51 27 40.6	0.40	58.1	8.5	6.4	20.1	12.5	4.2	126	19.8	20.0	2
379	10 06 11.47	+51 27 01.8	0.30	37.0	2.7	4.3	8.7	11.1	3.3	111	19.0	19.3	...
380	10 03 04.23	+51 27 19.7	0.70	72.7	13.5	6.1	24.8	-9.8	3.0	226	20.3	21.7	1
381	10 12 13.57	+51 26 42.2	0.50	39.5	11.1	-4.2	21.4	10.1	2.3	48	19.8	20.7	...
382	10 09 49.90	+51 25 46.6	0.80	63.5	10.0	8.6	-10.1	-8.9	2.3	22	21.8	22.0	2
383	10 20 09.03	+51 27 45.7	0.20	37.7	18.5	12.6	35.9	22.6	4.7	263	18.8	18.1	...
384	10 23 58.88	+51 22 10.5	0.40	80.6	15.5	13.4	29.1	43.5	5.8	192	19.0	20.0	3
385	10 03 03.38	+51 22 34.9	0.30	73.4	18.5	14.3	44.0	43.1	6.7	314	18.8	19.3	2
386	10 22 42.12	+51 23 02.1	0.60	68.5	22.0	21.7	41.0	34.7	3.4	161	20.8	21.3	3
387	10 24 14.20	+51 21 13.0	0.80	89.6	12.3	6.3	13.0	2.4	3.2	175	19.5	22.0	1
388	10 11 37.17	+51 20 22.5	0.50	44.9	16.7	12.8	29.9	22.1	2.6	81	20.3	20.9	...
389	10 25 53.66	+51 19 45.1	0.40	41.1	9.5	7.5	19.1	15.1	3.0	81	19.8	20.1	...
390	10 22 20.27	+51 18 13.1	0.30	43.7	11.5	11.3	32.0	33.1	4.0	221	18.8	19.4	...
391	10 25 02.64	+51 19 10.9	0.90	88.8	20.2	13.6	42.8	12.8	2.7	100	20.8	22.4	2
392	10 17 56.89	+51 18 11.8	0.60	43.9	8.6	1.7	7.5	-4.3	2.2	23	20.5	21.2	...
393	10 07 12.15	+51 18 38.6	0.50	51.3	10.1	2.8	25.4	-2.8	3.0	137	19.8	20.6	2
394	10 17 07.11	+51 16 20.4	0.70	72.3	16.8	11.6	22.1	2.8	3.0	44	20.5	21.7	2
395	10 05 55.06	+51 13 52.4	0.60	52.0	9.0	4.7	10.9	-0.3	2.5	101	20.8	21.1	2
396	10 09 05.07	+51 14 56.8	0.60	46.7	7.0	3.7	9.9	11.6	2.3	25	20.8	21.2	...
397	10 21 06.09	+51 14 44.2	0.40	55.5	13.1	15.5	30.3	28.1	4.0	152	19.5	20.2	1
398	10 07 02.65	+51 15 44.6	0.20	32.3	19.8	13.6	31.3	35.6	4.1	225	19.8	18.3	...
399	10 12 10.54	+51 13 53.5	0.90	88.7	19.2	10.1	45.8	7.7	2.7	121	20.8	22.4	2
400	10 01 28.93	+51 13 39.9	0.60	55.9	12.6	6.7	12.5	4.7	2.7	53	20.5	21.2	2

TABLE 2—*Continued*

ID	R.A. (J2000) Dec.		z_{est}	Λ_{CL}	$N_{A,0.25}$	$N_{e,0.25}$	$N_{A,0.5}$	$N_{e,0.5}$	σ	Rad ($''$)	m_3	m_{eff}	QA
401	10 11 30.72	+51 11 49.8	0.50	61.0	11.7	16.8	36.9	44.2	3.6	158	20.3	20.9	2
402	10 03 03.79	+51 10 57.5	0.20	27.1	8.5	6.4	42.9	30.7	3.4	234	18.8	18.5	...
403	10 21 57.83	+51 10 36.0	0.60	76.3	21.7	25.7	49.7	37.7	3.7	179	20.3	21.3	2
404	10 23 51.36	+51 11 34.4	0.40	42.8	10.5	11.5	39.1	63.1	3.1	151	19.8	20.3	...
405	10 22 50.58	+51 09 12.7	1.00	88.2	14.7	7.3	7.4	-8.2	2.4	40	22.0	22.7	2
406	10 12 21.43	+51 09 35.5	0.40	68.3	17.0	14.4	29.1	29.5	4.9	158	19.3	20.1	1
407	10 11 17.09	+51 06 38.4	0.30	44.6	3.5	5.3	12.0	20.1	4.0	176	17.8	19.2	...
408	10 08 08.90	+51 06 17.6	0.50	40.2	15.7	12.8	19.8	-3.8	2.4	38	20.0	20.8	...
409	10 21 00.41	+51 07 50.3	1.00	155.3	12.8	8.0	53.0	5.7	4.1	223	20.3	22.7	3
410	10 14 51.16	+51 05 37.1	0.40	30.3	6.5	16.4	1.1	15.5	2.2	17	19.0	20.1	...
411	10 19 18.50	+51 05 46.2	0.80	63.1	14.4	13.5	3.0	1.6	2.2	28	22.8	22.1	3
412	10 16 56.65	+51 04 59.1	0.80	70.3	30.5	13.9	24.9	-4.5	2.5	29	21.3	22.1	3
413	10 17 40.71	+51 04 24.0	0.30	68.4	29.8	34.2	36.3	55.8	6.2	142	18.5	19.4	3
414	10 25 39.03	+51 05 51.6	0.20	95.4	13.0	17.4	30.9	28.5	12.0	490	16.5	17.8	3
415	10 21 12.14	+51 04 33.8	0.30	61.9	20.5	27.2	43.0	72.8	5.6	290	18.8	19.5	1
416	10 22 43.26	+51 03 17.6	0.40	102.4	26.5	31.4	36.1	24.5	7.4	247	19.0	20.0	3
417	10 13 53.88	+50 59 32.9	0.30	43.2	9.8	14.3	23.3	28.1	3.9	92	18.5	19.3	...
418	10 12 25.66	+51 00 19.5	0.60	48.1	12.7	-0.3	23.6	-1.4	2.4	46	20.3	21.1	...
419	10 24 33.32	+51 00 41.5	0.40	42.7	9.1	5.4	9.3	-0.5	3.1	151	19.5	20.1	...
420	10 01 18.44	+51 01 33.0	0.20	33.0	4.4	3.3	-3.5	-10.9	4.1	231	17.8	18.0	...
421	10 22 54.02	+50 55 39.8	0.50	54.3	13.1	20.8	22.4	42.2	3.2	123	19.8	20.8	2
422	10 17 26.64	+50 53 40.3	0.20	20.1	0.4	-1.4	-5.5	-14.4	2.5	46	17.8	18.2	...
423	10 05 26.60	+50 58 44.5	0.20	62.6	14.5	18.6	21.9	23.6	7.8	414	17.0	18.1	3
424	10 03 33.21	+50 55 20.9	0.50	37.7	6.8	6.8	14.1	14.1	2.2	46	20.8	20.8	...
425	10 11 07.81	+50 54 29.7	0.40	32.3	10.1	13.5	4.3	12.1	2.3	26	19.5	20.2	...
426	10 06 33.73	+50 55 22.1	0.30	68.0	16.5	17.7	20.0	26.7	6.2	185	17.8	19.1	3
427	10 22 00.67	+50 53 06.1	0.60	58.8	27.6	19.7	32.5	11.6	2.9	54	20.5	21.2	2
428	10 17 43.52	+50 52 29.0	0.70	59.3	2.5	4.0	-1.9	2.4	2.5	34	18.8	21.8	1
429	10 22 47.81	+50 50 53.2	0.90	90.5	14.6	4.4	33.1	15.5	2.8	91	22.0	22.4	1
430	10 12 13.45	+50 55 05.8	0.20	44.0	9.4	11.6	15.5	18.6	5.5	322	17.8	18.1	...
431	10 19 40.62	+50 49 39.3	0.80	67.3	13.1	8.6	-0.9	-8.9	2.4	69	21.8	22.0	1
432	10 24 38.07	+50 49 42.5	0.90	70.2	10.4	5.5	16.1	11.3	2.2	17	22.0	22.4	1
433	10 08 07.87	+50 48 02.1	0.30	60.3	13.7	7.7	24.9	10.7	5.5	188	18.3	19.0	1
434	10 23 52.32	+50 49 31.8	0.50	50.2	17.1	6.8	35.4	30.1	3.0	64	19.8	20.7	1
435	10 12 06.90	+50 45 52.1	0.30	34.5	9.7	16.3	6.9	18.1	3.1	122	18.3	19.3	...
436	10 23 08.77	+50 46 36.0	0.20	48.8	10.4	12.3	19.7	25.1	6.1	290	17.3	18.1	...
437	10 01 00.13	+50 48 43.8	0.20	62.5	11.5	10.3	18.9	25.1	7.8	399	17.0	18.0	3
438	10 25 29.88	+50 47 44.5	0.40	47.2	9.6	4.4	12.3	24.5	3.4	153	18.8	19.9	...
439	10 24 42.24	+50 45 51.7	0.30	58.4	10.7	21.3	20.9	30.1	5.3	231	18.3	19.2	3
440	10 19 46.74	+50 47 40.9	0.40	60.0	11.5	11.4	12.1	27.5	4.3	143	19.0	20.0	1
441	10 21 25.04	+50 45 01.7	0.40	52.4	17.5	16.4	30.1	25.5	3.8	117	19.0	20.0	3
442	10 10 03.31	+50 43 44.7	0.40	31.5	12.4	14.5	8.5	25.1	2.3	26	20.8	20.2	...
443	10 20 01.51	+50 43 01.4	0.20	42.8	7.1	5.3	9.3	18.1	5.4	130	17.5	18.0	...
444	10 22 41.59	+50 40 56.3	0.70	69.3	18.2	14.9	51.9	33.4	2.9	82	21.3	21.7	1

Note. — CL309 = Abell 985, $N_A = 61$, $z = 0.1347$ (redshift from NED)
 CL414 = Abell 1004, $N_A = 76$, $z = 0.1414$ (redshift from NED)
 CL423 = Abell 915, $N_A = 54$, $z = 0.1484$ (redshift from NED)

TABLE 3
CLUSTER SAMPLE SIZE VS. MINIMUM SELECTION CRITERIA

Min. σ	Min. Λ_{CL}	Min. Effective Radius (arcsec)	Number of Clusters	No. with $z_{est} \geq 0.7$	No. with $z_{est} \geq 1.0$
2.0	10	5	444	154	63
2.5	10	5	341	91	33
3.0	10	5	217	38	10
3.5	10	5	146	16	2
4.0	10	5	95	2	1
2.0	10	5	444	154	63
2.0	20	5	440	154	63
2.0	40	5	338	154	63
2.0	60	5	189	134	63
2.0	80	5	106	92	61
2.0	10	5	444	154	63
2.0	10	10	441	151	60
2.0	10	25	402	122	48
2.0	10	50	329	89	32
2.0	10	75	267	70	24
3.0	60	60	93	38	10

TABLE 4
GALAXY REDSHIFTS

ID	R.A. (J2000) Dec.		I mag	z	z Error (km/s)	Comments
CL005						
1	10 10 45.21	+54 34 45.2	19.73	Low S/N
2	10 10 51.25	+54 35 09.6	20.23	0.3987	153	
3*	10 10 50.83	+54 34 24.8	19.03	0.3629	138	
4	10 10 46.94	+54 33 12.9	19.78	Low S/N
5*	10 11 01.52	+54 35 19.0	20.45	0.3654	174	
6	10 10 57.68	+54 34 05.7	18.34	0.2543	140	Emission
7*	10 11 01.00	+54 33 33.5	19.10	0.3650	120	
8	10 11 01.32	+54 33 03.2	17.69	0.5941	146	
9	10 10 55.27	+54 31 36.8	20.78	Low S/N
10	10 11 00.85	+54 32 09.8	19.51	Low S/N
11	10 11 07.15	+54 32 29.2	19.01	Low S/N
12	10 11 12.04	+54 32 48.5	18.16	0.0470	140	Emission
CL009						
1	10 20 27.89	+54 30 27.7	19.80	Low S/N
2	10 20 22.00	+54 31 05.8	18.06	0.2998	81	
3	10 20 18.31	+54 31 09.9	19.78	Modest S/N, weak features
4	10 20 16.20	+54 30 56.0	19.76	Low S/N
5	10 20 16.20	+54 30 56.0	19.76	0.1441	...	
6	10 20 11.28	+54 30 55.3	20.16	Low S/N
7*	10 20 13.75	+54 29 34.0	18.82	0.5507	73	
8	10 20 09.17	+54 30 21.0	19.08	0.7679	221	
9	10 20 08.28	+54 29 20.5	19.06	0.3376	83	
10*	10 20 08.83	+54 28 24.2	19.47	0.5591	134	
11*	10 20 11.08	+54 27 02.7	18.54	0.5532	82	
12	10 20 01.22	+54 28 44.0	19.73	Low S/N
13	10 19 57.74	+54 28 30.1	20.33	Low S/N
CL011						
1	10 22 15.47	+54 31 14.6	18.69	0.4313	140	Emission
2	10 22 18.06	+54 31 46.6	20.50	0.4307	85	Low S/N
3	10 22 23.85	+54 29 55.5	20.22	0.4720	87	
4	10 22 26.00	+54 30 37.4	19.61	0.7694	104	Low S/N
5*	10 22 27.87	+54 29 54.9	18.52	0.3032	68	
6*	10 22 31.23	+54 30 21.8	18.56	0.3028	140	Emission
7*	10 22 32.93	+54 30 18.4	19.83	0.3019	108	
8	10 22 37.25	+54 29 51.3	20.68	Low S/N
CL026						
1*	10 07 08.44	+54 18 29.6	17.73	0.5814	96	
2	10 07 04.47	+54 18 44.5	19.65	0.4095	67	Low S/N
3	10 07 00.39	+54 19 00.7	18.31	0.1302	140	Emission
4	10 07 01.51	+54 17 15.5	20.29	Low S/N
5*	10 06 55.43	+54 18 27.3	19.08	0.5775	97	
6	10 06 51.42	+54 18 38.8	20.09	Low S/N
7	10 06 47.46	+54 17 54.1	20.22	Low S/N
8	10 06 43.77	+54 18 19.1	20.13	Low S/N
9	10 06 43.32	+54 17 40.9	20.23	Low S/N
CL052						
1	10 18 42.78	+53 58 46.3	19.63	Low S/N
2	10 18 36.43	+53 59 46.2	19.44	0.6360	120	
3*	10 18 34.06	+54 00 18.7	19.50	0.5434	114	Low S/N
4*	10 18 43.76	+54 00 21.2	20.05	0.5445	123	
5*	10 18 44.64	+54 00 44.8	19.71	0.5449	93	
6	10 18 43.01	+54 01 20.0	20.02	Low S/N
7*	10 18 46.02	+54 01 23.0	18.88	0.5423	105	
8	10 18 36.01	+54 02 40.8	18.60	0.5163	162	
9*	10 18 48.90	+54 01 48.7	18.81	0.5471	168	
10	10 18 44.77	+54 03 25.6	20.54	Low S/N
CL062						
1	10 20 52.27	+53 55 48.5	18.77	0.3730	83	
2*	10 20 49.19	+53 55 45.9	20.39	0.4683	210	Low S/N
3	10 20 44.38	+53 55 20.0	19.66	Modest S/N, weak features
4	10 20 46.44	+53 56 08.7	19.60	Modest S/N, weak features
5	10 20 45.96	+53 56 39.4	20.20	Low S/N
6	10 20 40.09	+53 56 32.8	20.34	Low S/N
7*	10 20 40.80	+53 57 12.7	18.73	0.4546	113	
8	10 20 39.17	+53 57 33.4	19.46	Modest S/N, weak features
9	10 20 37.79	+53 58 07.6	20.09	Low S/N
10	10 20 34.69	+53 58 11.0	19.64	0.5690	114	Low S/N
11	10 20 32.29	+53 58 15.3	19.50	0.4882	127	Modest S/N
CL063						
1*	10 12 25.48	+53 52 08.8	18.34	0.3271	96	
2	10 12 20.11	+53 54 24.1	17.54	0.3749	66	
3	10 12 37.45	+53 51 26.2	20.68	Low S/N
4*	10 12 35.67	+53 52 42.8	19.12	0.3360	171	

TABLE 4—Continued

ID	R.A. (J2000) Dec.		I mag	z	z Error (km/s)	Comments
5*	10 12 36.13	+53 53 04.7	17.43	0.3297	78	
6	10 12 39.61	+53 53 10.0	18.25	0.1792	140	Emission
7*	10 12 38.11	+53 54 03.0	19.61	0.3275	93	
8	10 12 40.60	+53 55 02.1	18.98	0.3917	96	
9*	10 12 43.24	+53 54 55.0	18.46	0.3272	93	
10	10 12 46.65	+53 54 37.4	18.76	0.3907	162	
11*	10 12 49.25	+53 54 35.6	18.37	0.3278	189	
CL065						
1	10 19 01.40	+53 52 19.5	17.83	0.3287	129	
2	10 19 02.18	+53 50 54.4	19.63	Low S/N
3*	10 19 06.04	+53 49 07.3	20.11	0.4975	153	
4	10 19 12.04	+53 50 41.6	20.22	0.4585	141	
5	10 19 13.93	+53 50 33.9	19.03	0.4557	93	
6*	10 19 16.55	+53 51 16.9	19.29	0.5016	96	
7	10 19 19.19	+53 51 17.6	19.67	Low S/N
8	10 19 21.90	+53 52 25.0	20.01	0.5409	132	
9*	10 19 23.19	+53 49 27.2	19.16	0.4996	129	
10*	10 19 26.01	+53 49 28.8	19.25	0.5006	129	
11*	10 19 29.38	+53 50 06.0	19.88	0.5017	135	
CL084						
1	10 04 53.84	+53 45 21.0	20.67	Low S/N
2	10 04 56.56	+53 45 29.4	19.00	Low S/N
3	10 04 56.49	+53 43 40.5	19.16	0.3426	140	Emission
4	10 05 01.70	+53 46 15.1	18.74	0.4217	97	
5*	10 05 03.63	+53 45 54.6	19.08	0.4497	114	
6	10 05 03.85	+53 44 46.4	20.52	Low S/N
7*	10 05 07.72	+53 45 42.4	19.14	0.4465	150	
8*	10 05 10.40	+53 46 01.4	18.25	0.4463	78	
9*	10 05 13.81	+53 46 00.2	19.19	0.4462	114	
10	10 05 16.82	+53 45 41.9	19.91	Low S/N
CL112						
1	10 11 13.20	+53 32 24.6	19.36	Low S/N
2	10 11 04.86	+53 33 15.9	19.43	0.4883	93	
3*	10 11 15.11	+53 33 19.3	19.30	0.3894	135	
4	10 11 21.56	+53 33 21.0	18.58	0.5987	111	
5*	10 11 12.19	+53 34 30.6	17.81	0.3894	51	
6*	10 11 19.32	+53 34 30.3	17.55	0.3896	48	
7*	10 11 15.67	+53 35 01.3	18.61	0.3996	132	
8*	10 11 22.13	+53 35 09.2	19.48	0.3875	87	
CL115						
1	10 00 58.06	+53 30 52.0	19.02	Low S/N
2	10 00 42.04	+53 32 15.3	19.75	0.5639	120	Marginal S/N
3	10 00 50.60	+53 31 59.7	18.91	Low S/N
4	10 00 53.17	+53 32 05.6	19.30	Low S/N
5	10 00 50.30	+53 32 52.4	19.46	0.4202	96	Marginal S/N
6	10 00 57.44	+53 32 55.5	16.88	0.1458	60	
7	10 01 00.91	+53 33 18.1	18.00	S/N ok, weak features
8	10 01 00.91	+53 33 18.1	18.00	0.0389	140	Emission
9	10 01 01.62	+53 33 33.3	17.99	0.4198	51	
10	10 00 57.55	+53 34 25.7	19.70	Low S/N
11	10 01 03.80	+53 34 19.0	19.01	0.2246	126	
12	10 00 53.26	+53 35 30.4	20.54	0.3342	140	Emission
13	10 00 55.90	+53 35 37.3	20.04	Low S/N
CL157						
1	10 07 14.77	+53 18 32.7	19.95	Low S/N
2*	10 07 10.41	+53 17 37.6	19.35	0.2431	162	
3*	10 07 11.62	+53 17 01.2	18.47	0.2417	145	
4	10 07 28.60	+53 17 38.8	19.99	Low S/N
5*	10 07 16.05	+53 16 44.0	16.74	0.2433	102	
6*	10 07 14.87	+53 16 23.9	18.08	0.2432	93	
7	10 07 15.93	+53 16 01.4	19.84	Low S/N
8	10 07 23.35	+53 15 41.3	19.73	Low S/N
CL188						
1	10 24 15.05	+53 05 27.7	19.39	Low S/N
2	10 24 14.20	+53 05 11.1	18.76	0.1640	140	Emission
3	10 24 08.07	+53 04 55.1	20.26	Low S/N
4*	10 24 09.30	+53 04 25.0	17.90	0.3674	75	
5*	10 24 13.62	+53 04 02.0	18.55	0.3657	45	
6*	10 24 19.16	+53 03 34.7	17.55	0.3687	75	
7*	10 24 04.12	+53 03 18.2	18.81	0.3696	160	
8*	10 24 13.49	+53 02 56.5	18.61	0.3694	72	
9*	10 24 10.61	+53 02 34.1	18.19	0.3715	84	
CL189						

TABLE 4—*Continued*

ID	R.A. (J2000) Dec.		I mag	z	z Error (km/s)	Comments
1	10 04 06.37	+53 03 01.0	21.00	Low S/N
2*	10 04 04.84	+53 03 23.7	20.37	0.3779	131	Low S/N
3	10 04 06.02	+53 03 59.1	19.01	0.0461	140	Emission
4	10 03 56.67	+53 02 42.7	20.42	0.5872	113	
5	10 04 01.08	+53 03 53.4	19.08	0.6878	99	
6*	10 03 58.34	+53 04 22.9	19.20	0.3898	90	
7*	10 03 58.52	+53 04 57.2	18.02	0.3894	36	
8	10 03 54.93	+53 04 43.6	20.24	0.6886	124	
9	10 03 59.02	+53 05 52.2	20.40	Low S/N
CL207						
1	10 04 17.76	+52 54 14.5	19.97	Low S/N
2	10 04 15.77	+52 53 59.2	18.99	Low S/N
3*	10 04 11.61	+52 53 55.3	20.19	0.4452	115	Low S/N
4*	10 04 09.31	+52 53 17.5	18.11	0.4449	127	
5	10 04 10.87	+52 52 34.8	19.15	0.4680	149	
6	10 04 12.58	+52 52 03.3	18.50	0.3187	125	
7*	10 04 05.46	+52 52 04.0	18.75	0.4453	90	
8	10 04 04.04	+52 51 35.0	18.71	0.4261	107	
9	10 04 05.01	+52 51 09.1	19.34	0.2985	140	Emission
CL212						
1	10 25 49.52	+52 48 33.2	20.14	Low S/N
2*	10 25 49.37	+52 49 02.2	17.92	0.5323	74	
3*	10 25 46.69	+52 49 16.3	19.48	0.5284	108	
4*	10 25 45.94	+52 49 30.6	19.25	0.5220	124	
5	10 25 42.89	+52 49 34.3	19.68	Low S/N
6	10 25 42.89	+52 49 34.3	19.68	Low S/N
7*	10 25 46.33	+52 50 25.2	19.91	0.5340	103	
8*	10 25 44.61	+52 50 40.6	19.82	0.5277	95	
9	10 25 46.73	+52 51 16.2	20.17	Low S/N
10*	10 25 37.84	+52 50 49.1	20.09	0.5325	104	
11	10 25 35.49	+52 50 52.4	20.20	Low S/N
CL258						
1	10 20 44.79	+52 26 27.2	18.33	0.2471	141	
2	10 20 48.10	+52 27 01.6	19.66	weak features
3*	10 20 32.88	+52 27 49.4	18.82	0.4009	87	
4*	10 20 41.53	+52 27 52.0	18.26	0.3992	78	
5	10 20 45.46	+52 27 58.8	20.28	0.5162	150	Marginal S/N
6*	10 20 42.26	+52 28 39.9	19.18	0.3959	120	
7	10 20 46.79	+52 28 50.3	17.37	0.1486	75	
8	10 20 39.99	+52 29 21.1	19.40	Low S/N
9	10 20 43.31	+52 29 29.3	18.69	weak features
CL263						
1	10 00 47.41	+52 22 02.7	20.36	Low S/N
2	10 00 44.16	+52 22 24.8	20.76	0.5085	140	Emission
3	10 00 52.20	+52 22 26.2	18.88	0.2370	140	Emission
4	10 00 45.00	+52 23 01.7	20.05	Low S/N
5	10 00 54.90	+52 23 00.1	20.10	Low S/N
6	10 00 48.59	+52 23 38.8	19.48	0.4297	126	
7*	10 00 45.06	+52 24 00.9	19.09	0.5468	84	
8*	10 00 45.47	+52 24 25.7	19.69	0.5468	99	
9	10 00 43.13	+52 25 18.1	19.43	Good S/N, weak features
10	10 00 50.54	+52 25 22.5	20.49	0.4018	165	
CL268						
1*	10 18 05.85	+52 22 07.0	17.85	0.4637	94	
2	10 17 59.78	+52 24 09.3	20.20	Low S/N
3	10 17 56.56	+52 22 34.9	19.24	0.4167	181	
4*	10 17 53.22	+52 23 03.0	17.92	0.4631	70	
5	10 17 51.93	+52 22 05.0	19.19	0.4186	80	
6	10 17 48.85	+52 23 39.0	19.70	Low S/N
7	10 17 48.03	+52 22 31.8	19.60	Low S/N
8	10 17 42.26	+52 23 11.1	20.51	Low S/N
9	10 17 41.05	+52 22 26.7	19.64	Low S/N
CL310						
1	10 25 46.07	+52 01 40.8	17.62	0.1718	140	Emission
2	10 25 40.59	+52 01 01.8	20.70	Low S/N
3	10 25 45.53	+52 03 24.3	18.36	0.4220	60	
4	10 25 37.08	+52 02 09.1	18.58	0.2513	140	Emission
5	10 25 37.54	+52 02 44.7	18.51	0.4373	79	
6	10 25 34.86	+52 02 41.3	17.75	0.2516	140	Emission
7	10 25 39.92	+52 04 18.2	19.51	Low S/N
8*	10 25 36.97	+52 04 12.1	20.07	0.5084	159	
9	10 25 29.22	+52 03 26.5	20.58	Low S/N
10*	10 25 32.00	+52 04 35.2	19.52	0.4873	101	Low S/N
11*	10 25 25.74	+52 04 10.0	18.71	0.5059	88	

TABLE 4—*Continued*

ID	R.A. (J2000) Dec.		I mag	z	z Error (km/s)	Comments
CL335						
1*	10 14 08.80	+51 48 45.3	19.06	0.6128	140	Emission
2	10 14 10.65	+51 47 47.5	20.43	Low S/N
3	10 14 10.14	+51 47 27.2	19.18	Good S/N, weak features
4	10 14 03.65	+51 47 45.1	19.71	0.4871	140	Emission
5	10 14 03.05	+51 47 21.7	20.30	0.6575	137	Low S/N
6*	10 13 57.20	+51 47 54.9	20.64	0.6109	122	Low S/N
7	10 13 57.78	+51 47 27.6	19.30	0.6666	119	
8	10 13 55.74	+51 47 09.5	19.66	0.3875	81	
9	10 14 00.93	+51 45 53.9	19.93	Modest S/N, weak features
10	10 13 51.18	+51 46 42.0	20.72	Low S/N
11*	10 13 52.43	+51 45 48.8	19.28	0.6095	131	
12	10 13 49.90	+51 45 49.6	20.92	Low S/N
CL338						
1	10 16 08.96	+51 46 34.0	20.56	Low S/N
2*	10 16 11.00	+51 47 10.9	16.41	0.2577	54	
3	10 16 11.85	+51 47 34.5	20.36	Low S/N
4*	10 16 15.36	+51 47 43.1	18.98	0.2593	87	
5*	10 16 14.77	+51 48 03.1	19.01	0.2590	72	
6*	10 16 17.02	+51 48 13.3	17.93	0.2416	120	
7	10 16 16.87	+51 48 33.1	19.53	Low S/N
8	10 16 22.31	+51 48 46.6	19.24	Low S/N
9	10 16 26.33	+51 49 06.0	19.79	Low S/N
10	10 16 13.20	+51 49 55.7	19.26	Low S/N
CL350						
1	10 07 20.81	+51 39 46.7	19.60	0.5833	163	
2	10 07 18.67	+51 38 45.9	19.71	0.4248	88	
3*	10 07 20.60	+51 37 57.7	19.96	0.4024	127	
4*	10 07 24.20	+51 37 45.6	18.75	0.3898	64	
5	10 07 22.06	+51 36 46.0	18.94	0.6229	89	
6	10 07 23.63	+51 36 40.7	20.05	Low S/N
7	10 07 28.98	+51 36 54.6	20.29	Low S/N
8*	10 07 29.70	+51 36 29.8	18.80	0.3854	226	
CL378						
1	10 25 10.78	+51 26 37.3	19.46	weak features
2	10 25 16.65	+51 27 04.3	18.37	Good S/N, weak features
3*	10 25 17.67	+51 27 40.4	18.96	0.5169	93	
4*	10 25 19.92	+51 27 23.5	18.88	0.5157	81	
5*	10 25 21.57	+51 27 30.5	20.01	0.5165	96	
6*	10 25 29.47	+51 26 48.4	19.69	0.5095	126	
7	10 25 31.53	+51 27 32.5	19.83	Low S/N
8	10 25 33.49	+51 27 35.7	18.95	0.4660	129	
CL384						
1*	10 24 09.65	+51 22 42.0	19.35	0.5071	126	Low S/N
2*	10 24 09.32	+51 22 18.5	19.66	0.4944	119	Low S/N
3*	10 24 00.94	+51 23 15.0	18.96	0.4837	143	
4	10 24 07.61	+51 20 57.3	20.34	0.3355	171	Low S/N
5*	10 23 58.49	+51 22 20.6	19.67	0.5139	123	
6	10 23 58.49	+51 22 20.6	19.67	Low S/N
7*	10 23 56.64	+51 21 57.5	19.58	0.5116	96	
8	10 23 53.76	+51 22 08.5	19.53	Low S/N
9	10 23 56.31	+51 21 11.9	19.34	0.4161	126	
10	10 23 57.03	+51 20 35.3	19.48	0.3779	94	
CL385						
1	10 02 52.86	+51 20 16.1	19.85	Low S/N
2	10 03 00.02	+51 21 14.4	19.78	Low S/N
3	10 03 02.15	+51 21 37.5	19.17	0.4308	140	
4*	10 03 01.07	+51 22 12.9	18.59	0.2534	140	Emission
5*	10 03 04.57	+51 22 16.1	19.13	0.2518	51	
6	10 03 05.37	+51 22 41.0	18.27	0.1402	140	Emission
7	10 03 06.89	+51 23 04.6	19.81	Low S/N
8	10 03 01.81	+51 23 46.5	19.27	Low S/N
9	10 03 11.44	+51 23 48.4	18.67	0.2170	140	Emission
CL397						
1	10 21 20.73	+51 14 26.3	18.64	Low S/N
2	10 21 18.45	+51 13 57.7	19.83	Low S/N
3	10 21 16.99	+51 14 55.5	19.50	Low S/N
4	10 21 13.92	+51 15 58.9	19.02	Low S/N
5*	10 21 07.26	+51 13 55.8	19.34	0.4831	140	Emission
6*	10 21 05.89	+51 14 36.8	19.58	0.4960	88	
7*	10 21 04.09	+51 15 00.1	19.72	0.4980	89	
8*	10 21 00.99	+51 14 51.8	19.12	0.4883	161	
9	10 20 57.41	+51 14 14.9	20.42	Low S/N

TABLE 4—*Continued*

ID	R.A. (J2000) Dec.		I mag	z	z Error (km/s)	Comments
10	10 20 54.97	+51 14 21.4	19.06	0.4706	82	Low S/N
11	10 20 52.45	+51 14 15.0	20.27	Low S/N
CL406						
1*	10 12 32.77	+51 08 13.2	18.76	0.3206	140	Emission
2	10 12 32.84	+51 10 13.3	19.87	Low S/N
3*	10 12 21.30	+51 08 56.6	18.64	0.3153	138	
4	10 12 21.57	+51 09 20.5	19.18	0.3635	117	
5	10 12 19.55	+51 09 40.8	20.26	Low S/N
6	10 12 20.79	+51 10 22.1	19.93	Low S/N
7	10 12 14.51	+51 10 21.9	19.95	Low S/N
8*	10 12 16.60	+51 11 02.0	18.75	0.3382	84	
9	10 12 12.10	+51 10 51.1	20.08	Low S/N
10	10 12 09.21	+51 11 03.7	20.07	Low S/N
CL413						
1	10 17 28.80	+51 04 11.5	20.08	Low S/N
2	10 17 35.10	+51 04 02.3	19.83	Low S/N
3*	10 17 41.53	+51 02 57.1	19.06	0.3669	132	
4*	10 17 40.30	+51 03 50.9	18.79	0.3699	140	Emission
5*	10 17 40.26	+51 04 25.5	18.61	0.3681	75	
6*	10 17 43.83	+51 03 58.8	19.17	0.3704	81	
7*	10 17 41.56	+51 05 26.9	19.48	0.3650	141	
8	10 17 47.05	+51 04 48.1	19.39	0.5186	143	
9	10 17 49.50	+51 04 50.0	19.43	weak features
CL415						
1	10 21 21.63	+51 02 45.3	19.78	0.4088	121	Low S/N
2	10 21 15.71	+51 02 36.4	21.02	0.3226	99	Low S/N
3	10 21 18.88	+51 03 30.2	18.78	0.1658	84	
4	10 21 19.48	+51 04 03.6	18.72	0.4369	45	
5*	10 21 12.13	+51 03 56.6	20.20	0.3535	125	
6*	10 21 14.02	+51 04 34.5	18.85	0.3644	140	Emission
7	10 21 05.96	+51 03 58.1	18.75	0.3894	41	
8	10 21 09.36	+51 04 51.8	18.66	0.3867	135	
9*	10 21 05.40	+51 04 43.5	19.08	0.3654	89	
10*	10 21 11.82	+51 06 00.5	18.43	0.3516	50	
11*	10 21 09.19	+51 06 08.0	19.62	0.3528	115	
CL416						
1*	10 22 30.49	+51 04 30.8	20.61	0.4798	132	
2	10 22 37.67	+51 04 56.6	19.76	Low S/N
3*	10 22 39.63	+51 03 35.7	19.86	0.4791	84	
4	10 22 41.61	+51 03 33.6	19.68	Low S/N
5*	10 22 43.39	+51 03 13.3	18.83	0.4834	174	
6*	10 22 45.02	+51 03 08.7	18.62	0.4713	69	
7*	10 22 49.14	+51 02 17.7	19.37	0.4839	81	
8*	10 22 53.81	+51 03 49.1	19.53	0.4857	108	
CL426						
1	10 06 17.17	+50 55 07.1	19.93	0.1480	140	Emission
2*	10 06 22.06	+50 54 56.7	18.64	0.2232	70	
3	10 06 25.61	+50 54 49.3	18.83	0.3833	100	
4	10 06 27.87	+50 55 09.3	18.11	0.3821	70	
5*	10 06 32.31	+50 54 29.1	18.56	0.2247	96	
6*	10 06 32.99	+50 54 49.9	16.66	0.2273	69	
7	10 06 32.05	+50 55 55.1	18.86	0.3788	140	Emission
8*	10 06 35.71	+50 55 24.6	19.24	0.2254	132	
9*	10 06 38.66	+50 55 08.7	18.16	0.2263	117	
10	10 06 34.86	+50 56 48.7	18.93	Low S/N
CL433						
1	10 08 00.85	+50 47 15.7	18.74	Low S/N
2*	10 08 06.15	+50 47 46.9	18.15	0.2255	81	
3*	10 08 07.85	+50 47 50.3	18.41	0.2265	87	
4*	10 08 06.65	+50 48 44.8	18.28	0.2295	140	Emission
5*	10 08 13.61	+50 47 55.5	17.85	0.2279	72	
6	10 08 16.22	+50 47 51.6	19.59	Low S/N
7*	10 08 16.71	+50 48 32.5	19.06	0.2273	96	
8*	10 08 15.08	+50 49 30.1	18.92	0.2274	140	Emission
CL439						
1*	10 24 38.09	+50 47 45.2	18.73	0.3551	117	
2*	10 24 38.23	+50 47 04.3	19.20	0.3567	90	
3*	10 24 47.43	+50 46 33.7	19.19	0.3539	120	
4	10 24 29.95	+50 45 47.3	16.37	0.1366	57	
5*	10 24 41.98	+50 45 44.4	17.58	0.3548	78	
6*	10 24 44.29	+50 45 30.5	20.16	0.3542	230	
7*	10 24 41.36	+50 45 08.0	18.64	0.3584	63	

TABLE 4—*Continued*

ID	R.A. (J2000) Dec.		I mag	z	z Error (km/s)	Comments
CL440						
1	10 19 42.71	+50 49 30.3	19.45	0.3499	120	
2	10 19 57.39	+50 48 19.1	19.72	Low S/N
3	10 19 57.83	+50 47 53.4	19.91	Low S/N
4*	10 19 47.57	+50 48 00.9	19.00	0.4830	110	
5*	10 19 42.27	+50 47 56.3	19.55	0.4851	167	
6*	10 19 46.59	+50 47 30.0	18.65	0.4839	66	
7	10 19 48.33	+50 46 58.9	19.22	Low S/N
8	10 19 49.08	+50 46 41.8	19.81	Low S/N
9	10 19 47.37	+50 45 58.9	19.99	Low S/N
10*	10 19 43.13	+50 45 52.5	19.82	0.4796	134	
CL441						
1	10 21 36.72	+50 44 03.0	19.62	0.3529	140	Emission
2*	10 21 33.49	+50 44 33.2	19.58	0.4869	142	
3*	10 21 31.84	+50 45 25.5	19.10	0.4816	140	Emission
4	10 21 27.41	+50 44 54.4	20.67	Low S/N
5	10 21 25.66	+50 45 02.2	18.58	0.0788	140	Emission
6*	10 21 23.46	+50 45 17.9	20.63	0.4767	156	Low S/N
7*	10 21 20.92	+50 45 16.2	20.12	0.4831	114	
8	10 21 18.30	+50 45 28.3	19.60	Modest S/N, weak features
9	10 21 16.50	+50 45 27.1	19.84	Low S/N

Note. — Galaxies with an asterisk after their ID number are used in the computation of the mean cluster redshift. See Table 5 for results.

TABLE 5
CLUSTER REDSHIFTS

Cluster	\bar{z}	N_z	N_{spec}	N_{aper}	Cluster	\bar{z}	N_z	N_{spec}	N_{aper}
CL005	0.3644	3	6	11	CL310	0.5005 †	3	8	10
CL009	0.5543	3	7	13	CL335	0.6111	3	7	12
CL011	0.3026	3	7	8	CL338	0.2544	4	4	10
CL026	0.5795 ?	2	4	9	CL350	0.3925 †	3	6	8
CL052	0.5444	5	7	10	CL378	0.5147	4	5	8
CL062	0.4615 ?	2	5	11	CL384	0.5021	5	8	9
CL063	0.3292	6	10	11	CL385	0.2526 ?	2	5	9
CL065	0.5002	5	9	11	CL397	0.4914	4	5	12
CL084	0.4472	4	6	10	CL406	0.3247 †	3	4	9
CL112	0.3911	5	7	8	CL413	0.3681	5	6	9
CL115	7	12	CL415A	0.3575	5	10	10
CL157	0.2428	4	4	8	CL415B	0.3949	3	10	10
CL188	0.3687	6	7	9	CL416	0.4805	6	6	8
CL189	0.3857	3	7	9	CL426A	0.2254	5	9	10
CL207	0.4451	3	7	9	CL426B	0.3814	3	9	10
CL212	0.5295	6	6	10	CL433	0.2274	6	6	8
CL258	0.3987	3	6	9	CL439	0.3555	6	7	7
CL263	0.5468 ?	2	6	10	CL440	0.4829	4	5	10
CL268	0.4634 ?	2	4	8	CL441	0.4821	4	6	9

Note. — N_z is the number of galaxies used to compute the cluster redshift, N_{spec} is the number of galaxy redshifts measured, N_{aper} is the number of spectra extracted. See Table 4 for the specific galaxies used in the \bar{z} computation. Cluster redshifts marked with the † symbol have a maximum spread in the individual galaxy redshifts that exceeds the nominal 3000 km s^{-1} limit. Redshifts with question marks are based on fewer than 3 galaxies and may not be very reliable.

TABLE 6
 $\Lambda_{CL} \geq 40$ CLUSTER SURFACE DENSITY, CORRECTED FOR SELECTION FUNCTION

z_{est}	Clusters deg^{-2} with $z \leq z_{est}$	Effective Area of Survey (deg^2)
0.20	1.19 ± 0.28	14.762
0.30	3.02 ± 0.46	14.762
0.40	5.18 ± 0.64	14.762
0.50	7.52 ± 0.85	14.762
0.60	10.69 ± 1.12	14.586
0.70	14.70 ± 1.47	14.586
0.80	19.31 ± 1.88	14.528
0.90	24.46 ± 2.37	14.528
1.00	31.02 ± 2.97	14.293
1.10	39.81 ± 3.74	13.005
1.20	47.97 ± 4.50	11.071

TABLE 7
CUMULATIVE CLUSTER SPACE DENSITIES

Λ_{CL}	$N(\geq \Lambda_{CL})$ $h_{75}^3 \text{ Mpc}^{-3}$	Corresponding Abell Cluster Density
30	$(4.85 \pm 1.25) \times 10^{-5}$	1.17×10^{-5} , RC ≥ 0
40	$(1.83 \pm 0.50) \times 10^{-5}$	
50	$(8.54 \pm 2.58) \times 10^{-6}$	3.80×10^{-6} , RC ≥ 1
60	$(4.59 \pm 1.54) \times 10^{-6}$	
70	$(2.72 \pm 1.00) \times 10^{-6}$	
80	$(1.73 \pm 0.69) \times 10^{-6}$	
90	$(1.16 \pm 0.49) \times 10^{-6}$	9.16×10^{-7} , RC ≥ 2
100	$(8.09 \pm 3.67) \times 10^{-7}$	

Note. — Abell RC $\geq 0, 1$ densities from De Propris et al. (2002); RC ≥ 2 density from a compilation of Abell redshifts by Postman.